An agile and stable optical system for high-fidelity coherent control of a single $^{88}Sr^{+}$ ion

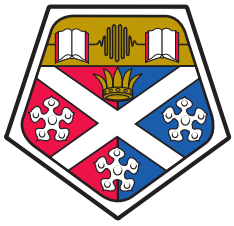

Joseph Andrew Thom

Department of Physics and SUPA

University of Strathclyde

Experimental work conducted at the
National Physical Laboratory

A thesis presented in the fulfilment of the requirements for the degree of

Doctor of Engineering

September 2015

'This thesis is the result of the author's original research. It has been composed by the author and has not been previously submitted for examination which has led to the award of a degree.'

Signed: Date:

Abstract

This thesis describes experiments involving the coherent manipulation of a single $^{88}Sr^{+}$ ion that is confined in a microfabricated trap. A stable and agile laser is constructed and used to perform rotations on an optical qubit that is encoded in the $D_{1/2}(m_j = -1/2)$ - $D_{5/2}(m_j = -5/2)$ transition at 674 nm.

After the excess micromotion is fully compensated in the microtrap, frequency-resolved optical pumping to the $S_{1/2}(m_j = 1/2)$ qubit level is demonstrated with 99.8 % efficiency and resolved sideband cooling is used to reduce the mean vibrational number of the axial mode to $\bar{n}_z \sim 1$. Deterministic ion transport between segments of the microtrap is also performed at frequencies up to 1 kHz.

The agile laser permits fast, accurate and precise modulation of the optical phase, amplitude and frequency on a sub-microsecond timescale. Amplitude-shaped pulses are produced in near-perfect agreement with the desired functional form for durations ranging over 10^6, which allows the frequency spectrum to be tailored in order to reduce off-resonant excitation. The agile system is stabilised in frequency by injection locking to an ultra-stable laser to yield a linewidth of < 10 Hz. Also, interrogation pulses are stabilised over a range of 10^5 in optical power using a cascaded series of avalanche photodiodes, and the beam position at the ion is stabilised to < 0.4 % of the beam diameter. The complete system is capable of performing single qubit gate operations with an infidelity below a fault-tolerant limit.

The agile laser is used to demonstrate that using Blackman rather than square shaped interrogation pulses offers an 11 dB reduction in off-resonant excitation. Also the phase agility of the system is verified using Rabi and Ramsey spectroscopy. Finally, a spin-echo sequence is used to enhance the storage time of the optical qubit, and high resolution scans over the quadrupole transition are performed to measure a system coherence time of 1 ms.

Acknowledgements

Firstly I must sincerely thank Alastair Sinclair for his insight, guidance and encouragement over the course of this project. His approach to experimental physics is to be aspired to, and I am fortunate to have conducted my postgraduate studies under his supervision. Equally I thank Guido Wilpers for his expertise on a huge variety of topics, and for always finding the time to share it with me. Much of my knowledge on running an ion-trap laboratory is down to him. Also to Erling Riis at Strathclyde, who has been of great help to me throughout this thesis on a variety of academic and non-academic issues.

I have benefited greatly during my time at NPL from working alongside a number talented and dedicated scientists. For the last year and a half it has been a pleasure to share the lab with Ben Yuen, from whom I have a learned a great deal, especially with regard to some aspects of the theory. Also to David Szwer for his invaluable advice on numerous occasions, especially during the writing of this thesis. The group has been greatly enhanced since the arrival of Kaushal Choonee, whom I also thank for his advice and encouragement. Lastly I thank Mariam Akhtar for her interest and enthusiasm over the last year or so, it has genuinely been a pleasure to give her an introduction to the experiment.

In the wider NPL community, I have enjoyed countless scientific discussions with many individuals who have consistently been willing to give up their valuable time for the benefit of their fellow researchers. To each of them I offer my utmost thanks and admiration; its people like you who make working at NPL such a pleasurable experience. Also to the NPL running club for the sessions in Bushy park; its surprising how intervals around the pond can help focus the mind. On a personal note, I'd also like to say that my time at NPL has been vastly improved by the presence and friendship of Stephen Kyriacou.

Outside of NPL, there are many people I must offer my thanks, without whom I might not have made it this far. Firstly to my house mates, Joe, Dorothy and Sam. Long days are the lab are much more pleasurable when there is something

to look forward to at home; you all helped more than you know. Somehow I have been ridiculously fortunate in my friends over the last few years. To the ones that really made a difference, they know who they are, all I can say is thank you very much. You guys made my decade.

Finally the biggest thanks of all goes to my family. To my sisters, Jennifer and Lucy, for making me the person I am today in so many ways. And to my parents, for teaching me all of the most important things in life. Their unwavering support has been the foundation of this thesis.

Contents

List of Figures

Chapter 1

Introduction

The ion trap is an ideal system for experimental quantum physics. An individual ion can be tightly confined, yet be virtually free from external perturbations that would otherwise disturb the delicate quantum state of the particle. Two internal energy levels of an ion can be used to store quantum information, and transitions between levels are implemented with externally applied radiation. When several ions are trapped in a linear string, a tunable coupling exists between each entity due to the Coulomb repulsion, which allows quantum information to be distributed between ions. Such a system is an ideal platform for experimental *quantum information processing* (QIP), as first suggested by Cirac and Zoller in 1995 [1]. Since then the research field of trapped ion QIP has grown enormously from initial proof-of-concept demonstrations to a worldwide coordinated effort, involving many research groups and significant amounts of investment, all with the common goal of realising a functioning quantum computer with trapped ions. The main purpose of this thesis is to develop techniques that maximise the fidelity of single qubit quantum gates, a basic yet crucial component of QIP. However the methods presented are also of benefit to the field of *quantum metrology*, which seeks to provide ever more precise measurements of physical quantities due to the exploitation of quantum effects such as coherence, superposition and entanglement. This chapter serves to review the status of the ion trap research community with respect to both of these topics. An outline of the structure of this thesis is also presented, along with an account of the specific contributions made by the author.

1.1 Quantum information processing

Richard Feynman was the first to propose in 1982 that two of the greatest advances in science and technology of the 20th century, the discovery of quantum mechanics and the digital revolution based on classical computation, could be combined to realise a quantum computer [2]. Here the physical laws that govern classical computing are replaced with those given by quantum mechanics, where concepts such as superposition and entanglement allow for a degree of parallelism and hence computational speed up. This remained a theoretical curiosity until the discovery by Peter Shor in 1994 [3] of a quantum algorithm that offered an exponential speed up of the factorisation of large numbers over its classical counterpart. This galvanized a large amount of experimental work aimed at demonstrating quantum gates and algorithms as the basis of a future quantum computer. This motivation was bolstered by further discoveries of quantum algorithms, such as Grover's search algorithm for searching unsorted databases [4] and the Deutsch-Joza algorithm [5]. The discovery of other computational problems that could benefit from quantum computation remains a major research effort in its own right, and it is still unclear as to what extent a practical quantum computer could in theory outperform a classical one. However, an area in which the techniques developed for QIP are already having an impact is the related field of quantum simulation [6], which is already being used to investigate quantum systems that would be impractical to model on a classical computer.

In particular, there has been tremendous progress towards QIP with linear Paul traps since the original proposal of Cirac and Zoller [1]. Here the authors suggested that qubits could be encoded in the internal state of trapped ions and manipulated with laser beams to form single qubit gates. Furthermore, multi-qubit gates are realised through the collective quantised motion of the ions in a linear ion string. The stringent requirements of a practically viable quantum computer were summarised by DiVincenzo in 2000 [7]. Further insight into the state of experimental progress of QIP with trapped ions is gained by describing the state of the art with respect to each of these requirements:

1) *A scalable system with well characterised qubits*

For ion trap QIP, the issue of scalability relates to finding a trap architecture that can handle the many qubits that would be required to implement useful computations. Whilst many important proof-of-principle experiments have been demonstrated with custom-machined ion traps that can only trap $\sim$ 10 ions, current efforts are focused on microfabrication to realise an architecture where scaling to many qubits is more feasible. Two approaches are being pursued in this regard. Firstly, 2-dimensional geometries where the electrodes of an ideal linear Paul trap are reduced to one plane have been demonstrated by many groups. This is motivated by a proposal for trapped ion QIP [8] where separate ion traps are designated with individual purposes, such as memory and readout etc. and are interconnected by shuttling junctions. The planar geometry allows for relative ease of fabrication, enabling complex functionalities such as transport through Y [9] and X shaped [10, 11] junctions to be realised. However the planar geometry reduces the harmonicity of the trapping potential significantly compared to the ideal case, yielding low trapping [12] efficiencies. A closer approximation to the ideal linear Paul trap can be achieved with a 3-dimensional microfabricated structure. A 3-D monolithic multi-segmented ion trap is used in the work of this thesis, and is described in detail in chapter 3. Comprehensive reviews of microfabricated ion trapping have been given elsewhere [13, 14].

Trapped ion qubits are commonly realised in three distinct ways. Firstly a qubit can be encoded in two hyperfine energy levels of the ground state in ions with odd nuclear spin, and are typically manipulated with microwave or Raman fields. For example pioneering work conducted at the NIST ion storage group was implemented with $^{9}Be^{+}$ [15, 16], similarly the Oxford group uses $^{43}Ca^{+}$ [17] and the Maryland group uses $^{171}Yb^{+}$ [18]. A second approach is to encode the qubit in two Zeeman sub-levels of the electronic ground state, as used by the Weizmann Institute in $^{88}Sr^{+}$ [19] and the Oxford group with $^{40}Ca^{+}$ [20, 21]. The third option is to encode quantum information in the ground and metastable excited states to realise an *optical qubit* that is manipulated with a narrow linewidth laser. Examples include the $^{40}Ca^{+}$ isotope as used in the Innsbruck experiment [22], and the $^{88}Sr^{+}$ ion as used in the MIT group [23] and in the experiment described in this thesis [24].

2) *The ability to initialise the register to a simple fiducial state*

The initialisation of the quantum register typically consists of optical pumping to a desired electronic level and sideband cooling to the motional ground state. The first of these can be implemented by selectively driving transitions with a laser beam of well-defined polarisation, however the efficiency of this process is very sensitive to polarisation impurities. A more robust method is frequency-resolved optical pumping, which has been achieved with an efficiency of 99.9 % [25]. Sideband cooling to the motional ground state [26, 27] has also been achieved with efficiencies of 99.9 % [22]. Progress towards similar efficiencies with both sideband cooling and frequency-resolved optical pumping are described in chapter 4 of this thesis.

3) *Long relevant decoherence times, much longer than the gate operation time*

Qubits based on hyperfine or Zeeman sub-levels can have long lifetimes, as they exist only in the electronic ground state and are therefore not subject to spontaneous decay. For example a quantum memory realised with a $^{9}Be^{+}$ qubit had a coherence time of over 10 seconds [28]. Coherence times greater than 1 second have also been achieved with $^{43}Ca^{+}$ [17] and $^{171}Yb^{+}$ [18]. In contrast, the metastable excited state of an optical qubit has a natural lifetime on the order of 1 s (390 ms for $^{88}Sr^{+}$ [29]). This places a fundamental constraint on the attainable coherence times in an experiment. In $^{40}Ca^{+}$, a single qubit coherence time of 95 ms was measured [30], in contrast to the 1.2 s natural lifetime of the metastable state. Therefore it is clear that technical decoherence such as laser and magnetic field noise limits the coherence times for optical qubits. These sources of noise can partially be cancelled through the use of spin-echo techniques, as described and implemented experimentally in chapter 7. Decoherence-free subspaces [31] have also been employed to engineer entangled states that are insensitive to some sources of technical noise for both hyperfine [32] and optical [25] qubits.

4) *A universal set of quantum gates*

For trapped ion QIP, it is sufficient to realise only single and two-qubit gates with high-fidelity to form a universal set. Single qubit gates are realised with

pulsed laser, microwave or radio frequency fields that are tuned to the qubit resonance frequency. For a single-ion quantum register, fidelities in excess of 99.99 % have been observed for hyperfine qubits [17, 33]. For optical qubits, fidelities are currently limited to 99.5 % [34], mainly due to the particularly harsh constraints on the stability of the laser used to manipulate the qubit. Implementing high fidelity gates on a single ion in a multi-qubit register is more challenging, and requires either tight-focussing of the addressing laser to a few microns [35] or inducing a position dependent qubit transition frequency via a controlled magnetic field gradient [36], which has recently been implemented with a nearest ion cross-talk of 10^{-5} [37].

The Cirac-Zoller two-qubit gate was the first to be suggested [1] and has been demonstrated with a fidelity of 92.6 % using the $^{40}Ca^{+}$ optical qubit [38]. This gate is however is technically demanding as it requires both individual ion addressing and perfect ground state cooling. The Mølmer-Sørensen entangling gate [39, 40] has no such stringent requirements, and has already been demonstrated with a fidelity of 99.3 % for two ions using $^{40}Ca^{+}$ [41] in Innsbruck. The same group used the gate to entangle up to 14 qubits in a single register, although this was at a significantly reduced fidelity of $\sim$ 50 % [30]. The Mølmer-Sørensen gate has also been used to entangle $^{43}Ca^{+}$ hyperfine qubits with a fidelity of 96.7 % [42]. Finally a geometric phase gate has been used to entangle $^{9}Be^{+}$ hyperfine qubits with a fidelity of 97 % [16]; ground state cooling and single-ion addressing was not required in this case also.

5) *A qubit specific measurement capability*

State measurement is carried out by imaging ion fluorescence for all of optical, hyperfine and Zeeman qubits according to Dehmelt's electron shelving method [43]. Here fluorescence is only produced during resonant excitation when the ion is in one of the two qubit levels. The method is particularly convenient for optical qubits as the metastable state is dark to the exciting field, and scalable single-shot readout fidelities of 99.99 % have been achieved [44]. The same method of direct state-selective florescence detection may also be used for hyperfine qubits, however the process fidelity is limited to $\sim$ 99.5 % due to off-resonant scattering of the state detection laser on one of the qubit levels [18, 45]. State-selective

optical pumping to a metastable level can be used to eliminate this problem, yielding a detection fidelity for hyperfine qubits of 99.8 % [46]. A similar method has been used to map a Zeeman qubit to an optical transition in order to achieve a detection fidelity of 99.9 % [19].

Other notable milestones in the trapped ion QIP field have been the demonstration of teleportation of quantum information between ions [47, 48] in the same quantum register, and similarly the heralded teleportation of ion qubits in remote ion traps [49]. Basic error correcting codes, as required by any practical implementation of QIP, have also been demonstrated [50], as well as basic demonstrations of quantum algorithms such as the Grover search algorithm [51] and the Deutsch-Joza algorithm [52]. Also, significant progress has been made with regard to the deterministic transport of ions between segments of a microtrap array, as motivated by the original proposal for trapped ion QIP [8]. Notably, non-adiabatic transport protocols has been shown where single ions were transported between separate zones of a microtrap array with negligible heating of the motional mode [53, 54].

Other physical systems are also being researched as potential platforms for scalable QIP. Prominent among these are nuclear spins [55, 56], single photons [57], quantum dots [58, 59] and superconducting Josephson junctions [60]. The subtleties of the advantages and disadvantages of each platform are too numerous to be discussed here, however a detailed review of each has been given previously [61]. However is worth noting the recent demonstration a two qubit-entangling gate with 99.4 % [62] fidelity with superconducting Josephson junctions, which is comparable with the analogous value of 99.3 % for trapped ions [41]. Solid-state systems indeed seem favourable for their potential in scalability, yet suffer from relatively short coherence times on the order of microseconds. It remains to be seen which physical platform will ultimately be used for a practical quantum computer, if not a hybrid of different systems, however trapped ions are undoubtedly a leading candidate due to the significant experimental progress that has been outlined in this section.

1.2 Quantum metrology

Due to the highly reproducible nature of transition frequencies in trapped ions and atoms, they are ideal reference standards for atomic clocks. Indeed the S.I. definition of the second itself is based on the interrogation of hyperfine transitions in Caesium with microwave radiation. However in the near future the second may be redefined in terms of an optical frequency that is referenced to a single trapped ion or neutral atoms in an optical lattice [63]. This is because optical transitions have a $\sim 10^5$ higher quality factor Q compared to transitions in the microwave domain, and therefore offer an inherently lower instability, and relative uncertainties at the 10^{-18} level seem feasible in the near future. Other applications of such precise timekeeping range from tests of fundamental theories, such as searching for variations in the fine structure constant [64, 65], to practical applications such as improved GPS navigation and geodesy [66].

Specifically, alkali-like ions such as $^{88}Sr^+$, $^{40}Ca^+$ etc. have narrow quadrupole transitions that have natural linewidths in the range of a few hertz, and are currently being assessed as potential candidates. Of particular relevance to the work presented in this thesis is the $^{88}Sr^+$ single-ion standard, which currently has an estimated systematic fractional uncertainty contribution of 2×10^{-17} [67, 68], which is the ultimate limit to the long term performance of the standard. Similar systematic uncertainty contributions have been estimated in the quadrupole transition standards of $^{199}Hg^+$ [69], $^{171}Yb^+$ [70] and $^{40}Ca^+$ [71]. An extremely narrow octupole transition in $^{171}Yb^+$ (1 nHz linewidth [72]) also shows promise as a standard, particularly since the invention of an interrogation scheme that largely cancels the light shift due to the intense fields needed to probe the very weak transition [73, 74]. A thorough assessment of the strengths and limitations of the various optical clock candidates has been given elsewhere [63].

Absolute frequency measurements are currently limited by the primary standards that are used to realise the second [75, 76]. Recently, measurements of two independent octupole $^{171}Yb^+$ standards agreed to within a part in 10^{15}, representing the best international agreement between standards to date. However to fully assess the stability of an optical standard, direct comparisons must be made by referencing one system to another. Of particular interest is a comparison of

two frequency standards based on $^{27}Al^+$ that were found to have a fractional frequency difference of 1.8×10^{-17}, where one of the standards had particularly low systematic uncertainty contribution of 8.6×10^{-18} [77]. However $^{27}Al^+$ poses extra experimental challenges as it possesses no convenient cooling or detection transitions. Therefore a technique known as quantum logic spectroscopy [78] is used to map the quantum state of $^{27}Al^+$ ion to a sympathetic coolant ion such as $^{9}Be^+$ or $^{25}Mg^+$.

Quantum logic spectroscopy is an example of a technique that is inspired by established methods in the field of trapped-ion QIP being used to enhance the precision and accuracy of optical atomic clocks. Another such example is the proposal that entangled states of trapped ions may increase the precision of spectral phase estimation in Ramsey spectroscopy [79, 80], as demonstrated experimentally with $^{9}Be^+$ hyperfine qubits [81, 82]. Whilst improved phase estimation with up to 14 optical qubits has been realised [30], no benefit from the use of entangled states in an operational frequency standard has been shown to date. However, the demonstration of decoherence-free subspaces [25] has shown how entanglement can be employed to create states that are insensitive to magnetic field noise; a promising route to reducing the systematic uncertainty of an optical atomic clock.

1.3 Thesis structure and author contribution

This thesis is organised as follows. Chapter 2 provides explanations of the theoretical concepts that are relevant to the experimental work in this thesis. Chapter 3 describes the setup of the experiment, with emphasis on the apparatus that was altered or installed during the course of this thesis. Namely this was the construction and installation of a low drift reference cavity for a 1033 nm quench/clearout laser. Significant contributions were also made to the experimental control system so that the agile pulse sequences described later in this thesis could be integrated with the wider experiment. Chapter 4 describes various experimental techniques that must be successfully implemented for quantum gate operations to be possible. All of the data described in this chapter was recorded and analysed independently by the author, however the ion transport experiments were only

possible due to the installation of a multichannel arbitrary waveform generator by Tanveer Baig. An agile laser system that is designed for accurate and precise modulation of the temporal shape, phase and frequency of interrogating laser pulses is described in chapter 5. Here the author was entirely responsible for the construction of the system and collected and analysed all of the data. Chapter 6 proceeds to describe how the agile system is stabilised in terms of power, beam pointing and frequency in order to realise a qubit manipulation system that is capable of implementing single qubit gates at the fault-tolerant threshold of quantum computation. The extra experimental hardware used in this chapter, which was added to the system described in chapter 5, was constructed in equal collaboration between the author and Ben Yuen. Both researchers also contributed equally to the recording and analysis of the results. However the headline result of this chapter, which is the demonstration a long-term stability sufficient for fault-tolerant operation, was only possible after the author independently diagnosed and eliminated sources of excess drift in the system. Finally, chapter 7 describes the application of the agile laser system to the coherent manipulation of a single trapped ion. This includes a demonstration of using amplitude-shaped pulses to minimise the probability of off-resonant excitation in a single qubit rotation and an assessment of the limits of coherence in the system. In this chapter, the author collected and analysed all of the results independently. Furthermore, all of the numerical simulations in the chapter were carried out by the author. These were done using a Matlab package that was significantly updated from a previous version (written by Valliappan Letchumanan) to account for the effects of amplitude shaping and phase agility in Rabi and Ramsey spectroscopy.

Chapter 2

Theory

2.1 Introduction

This chapter introduces theoretical concepts that are relevant to the experimental work conducted in this thesis. As the long-term goal of this experiment is to realise high-fidelity quantum gate operations, the discussion naturally begins with a description of the qubit, which is the basic unit of information in a quantum processor. A geometrical representation of an arbitrary single qubit state is described by means of a Bloch vector that points to the surface of a Bloch sphere. Arbitrary rotations on the Bloch sphere are described as unitary operators acting on the qubit state, and a method of characterising the qubit by a series of projective measurements is discussed.

The equations of motion for a qubit that is manipulated with a monochromatic laser are presented in the form of the optical Bloch equations. These describe the dynamics of the Bloch vector in terms of a Rabi frequency and a detuning from resonance for a qubit that is subject to decoherence. Also presented (without derivation) is a solution to the optical Bloch equations that describes the excitation probability of the qubit as a function of detuning for the case of excitation with pulses of a fixed Rabi frequency. This serves as a foundation for further discussion of the effects of pulse shape on spectral lineshape, as presented in chapter 7. Furthermore, a description of Ramsey and spin-echo spectroscopy is given in terms of a sequence of rotations around the Bloch sphere. An application

of the latter technique to increasing the lifetime of a qubit subject to technical noise is also described.

As the discussion so far has focused on a general qubit, the final section of this chapter proceeds to describe how a qubit is physically realised in this experiment as a trapped ion with internal and external states that are manipulated with a laser. The physics of linear Paul traps is briefly discussed, and the equations that characterise the motion of a single confined ion are presented. Also, the quantisation of a trapped ion's motional degrees of freedom is described, along with a discussion of how this modifies the properties of an ideal qubit. The internal structure of a single $^{88}Sr^{+}$ ion is described with reference to its suitability as a qubit candidate, and the transitions used to realise practical quantum information processing are described. Among ten Zeeman components of a narrow quadrupole transition, one is chosen to encode the qubit. Also given is a description of the selection rules of the dipole transitions in strontium, as these are key to understanding several of the experimental techniques demonstrated in chapter 4. Finally, the chapter concludes with a description of the Mølmer-Sørensen entangling gate.

2.2 The qubit and the Bloch sphere

A 'qubit' is a quantum system that has two distinct states that can be used to store and represent one unit of binary information. In this respect a qubit is analogous to the bit that is familiar from classical information processing. However qubits differ in that they may exist in linear superpositions of the two orthogonal states. In this chapter, the qubit states are labelled $|S\rangle$ and $|D\rangle$ to reflect the specific implementation in this experiment as described in this chapter. However the qubit is a concept that has a generality above any specific experimental implementation, and is treated as such in the following description of its properties.

A general qubit state is written

$$|\Psi\rangle = a_S |S\rangle + a_D |D\rangle , \tag{2.1}$$

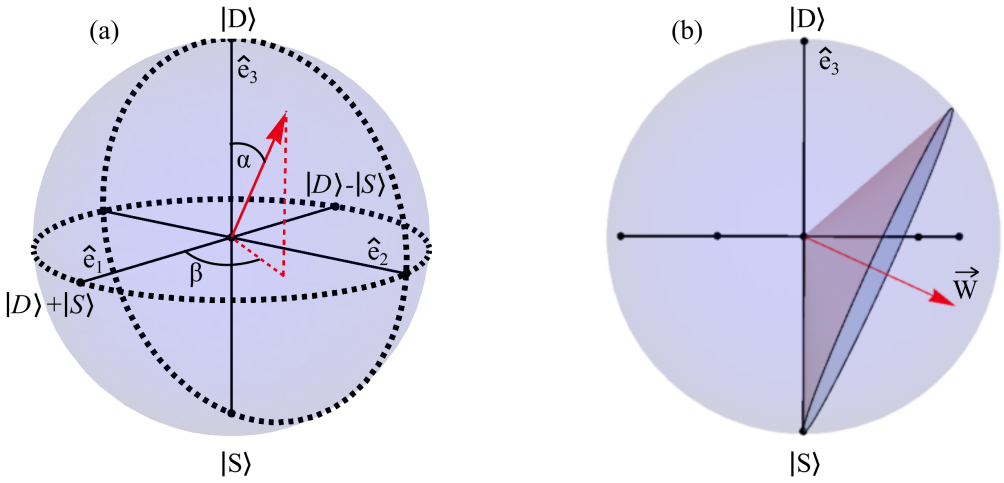

Figure 2.1: (a) Bloch sphere representation of the qubit, with the states $|S\rangle$ and $|D\rangle$ shown at the poles. General superposition states are described by the polar coordinates α and β as expressed in equation 2.2. (b) Side on view of the Bloch sphere, showing the vector $\vec{W}$, which is the axis of rotation for non-zero detuning.

where a_S and a_D are complex numbers that represent the probability amplitudes associated with each state. As these coefficients satisfy the condition $a_S^2 + a_D^2 = 1$, it is convenient to rewrite equation 2.1 as

$$|\Psi\rangle = \cos\left(\frac{\alpha}{2}\right)|D\rangle + e^{-i\beta}\sin\left(\frac{\alpha}{2}\right)|S\rangle\,. \tag{2.2}$$

This representation allows the complex qubit state to be visualised as a *Bloch vector* with polar coordinates α and β. The permitted values of the Bloch vector lie on the surface of a sphere, which is referred to as the *Bloch sphere*.

With reference to the Bloch sphere shown in figure 2.1, the south and north poles represent the states $|S\rangle$ and $|D\rangle$ respectively (all opposite points on the sphere are orthogonal). All other points represent superpositions of the two states, with points on the equator denoting equal superpositions. The angle α defines the latitude of the Bloch vector, and fully describes the population of each level. β defines the longitude of the Bloch vector and represents the relative phase of the coefficients a_S and a_D.

In a single qubit gate operation, the qubit is initialised into one of the qubit eigenstates i.e., $|S\rangle$. Subsequent rotations of the Bloch vector around the Bloch sphere are given by unitary operators acting on the state

$$|\Psi\rangle = \begin{pmatrix} a_S \\ a_D \end{pmatrix}. \tag{2.3}$$

For example arbitrary rotations of the Bloch vector by Θ around an axis defined by a unit vector $\vec{n}$ are described by

$$R_{\hat{n}}(\Theta) = e^{-i\Theta\vec{n}.\vec{\sigma}/2} = \cos\left(\frac{\Theta}{2}\right)I - i\sin\left(\frac{\Theta}{2}\right)\left(n_x\sigma_x + n_y\sigma_y + n_z\sigma_z\right). \tag{2.4}$$

where I is the identity operator and σ_x, σ_y and σ_z are the Pauli spin matrices [83]. A succession of such rotations may be used to realise a mathematical description of any single qubit gate. This formalism is limited in that it does not account for the physical mechanisms that cause the Bloch vector to rotate. In section 2.3, the temporal dynamics of the Bloch vector due to excitation with an external field are described fully.

A single measurement does not yield the full information on the qubit state $|\Psi\rangle$, rather a projective measurement yields either the state $|S\rangle$ or $|D\rangle$ with probability a_S^2 and a_D^2 respectively. In the case of trapped ions, the application of laser light to a transition that is auxiliary to the qubit projects the system into one of two energy levels, as described in chapter 4. This corresponds to a collapse of the qubit wavefucntion $|\Psi\rangle$ into one of eigenstates of a measurement operator $\hat{M}$ with eigenvalues m. With the associated projection operators $\hat{P}_m$ this is written

$$\hat{M} = \sum_m m\hat{P}_m. \tag{2.5}$$

The probability of the outcome m occurring when measuring the state $|\Psi\rangle$ is

$$p(m) = \langle\Psi|\,\hat{P}_m\,|\Psi\rangle\,. \tag{2.6}$$

Following the measurement, the qubit is projected into one of the eigenstates and is in the state

$$|\Psi'\rangle = \frac{\hat{P}_m |\Psi\rangle}{\sqrt{p(m)}}. \tag{2.7}$$

As only a binary piece of information is obtained from each measurement, it is clear that many measurements of identically prepared qubits are necessary to fully characterise the state of the qubit. With a single trapped ion, this is achieved by performing many cycles of qubit preparation, rotation and measurement as described in the introduction to chapter 3.

2.3 Qubit manipulations with a monochromatic laser

In this section, the quantum dynamics of an ideal two-level atom with ground state $|S\rangle$ and excited state $|D\rangle$ are considered for the case of excitation with a monochromatic laser of frequency ω_L and phase ϕ, which couples to the ion with a characteristic coupling strength Ω_R. The density matrix for the system is:

$$\hat{\rho} = \begin{pmatrix} \rho_{SS} & \rho_{SD} \\ \rho_{DS} & \rho_{DD} \end{pmatrix}, \tag{2.8}$$

where ρ_{SS} and ρ_{DD} are the populations of each level and ρ_{SD} and ρ_{DS} represent the coherence between the levels. The time evolution of the density operator is given by:

$$\frac{d}{dt}\hat{\rho} = -\frac{i}{\hbar}[\hat{H}, \hat{\rho}], \tag{2.9}$$

where $\hat{H}$ is the Hamiltonian operator

$$\hat{H} = \begin{pmatrix} E_S & 0 \\ 0 & E_D \end{pmatrix} + \begin{pmatrix} 0 & \frac{1}{2}\Omega_R e^{-i(\omega_L t+\phi)} \\ \frac{1}{2}\Omega_R e^{i(\omega_L t+\phi)} & 0 \end{pmatrix}. \tag{2.10}$$

Here the first term represents the internal energy of the atom E_D-$E_S = \hbar\omega_{atom}$ and the second term represents the energy of the atom-laser interaction in the

rotating-wave approximation. The effective decoherence rate due to the finite laser bandwidth Γ_L and the spontaneous decay rate of the atom Γ_{DS} are accounted for in a fashion similar to Boyd [84] and Letchumanan [85] to yield the coupled differential equations

$$\dot{\tilde{\rho}}_{DS} = [i\delta - (\Gamma_L + \frac{1}{2}\Gamma_{DS})]\tilde{\rho}_{DS} - i\frac{\Omega_R}{2}e^{-i\phi}(\rho_{DD} - \rho_{SS}), \tag{2.11a}$$

$$(\dot{\rho}_{DD} - \dot{\rho}_{SS}) = -\Gamma_{DS}[1 + (\rho_{DD} - \rho_{SS})] + i\Omega_R(e^{-i\phi}\tilde{\rho}^*_{DS} - e^{i\phi}\tilde{\rho}_{SD}), \tag{2.11b}$$

where $\delta = (\omega_L - \omega_{atom})$, the substitutions

$$\tilde{\rho}_{SD} = e^{(-i\omega_L t)}\rho_{SD}, \tag{2.12a}$$

$$\tilde{\rho}_{DS} = e^{(i\omega_L t)}\rho_{DS}, \tag{2.12b}$$

have been made and $\tilde{\rho}^*_{DS} = \tilde{\rho}_{SD}$. Insight into the dynamics of the equations are found by setting $\phi = 0$ and separating $\tilde{\rho}_{SD}$ into its real and imaginary parts according to

$$\tilde{\rho}_{SD} = \frac{1}{2}(u - iv). \tag{2.13}$$

Equations 2.11 can subsequently be rewritten as

$$\dot{u} = \delta v - (\Gamma_L + \frac{1}{2}\Gamma_{DS})u, \tag{2.14a}$$

$$\dot{v} = -\delta u + \Omega_R w - (\Gamma_L + \frac{1}{2}\Gamma_{DS})v, \tag{2.14b}$$

$$\dot{w} = -\Omega_R v - \Gamma_{DS}(w - 1), \tag{2.14c}$$

where $\dot{w} = (\dot{\rho}_{DD} - \dot{\rho}_{SS})$. These are collectively known as the optical Bloch equations, and describe the motion of the Bloch vector $\vec{R}$ around the Bloch sphere due to excitation by a near-resonant laser field. With reference to figure 2.2(a),

this generalised vector is described by

$$\vec{R} = u\hat{e}_1 + v\hat{e}_2 + w\hat{e}_3. \tag{2.15}$$

For a qubit initialised in either $|S\rangle$ or $|D\rangle$ and at zero detuning (δ=0), the Bloch vector rotates around the $\hat{e}_1$ axis from pole-to-pole at the Rabi frequency Ω_R (see figure 2.1(a)). For $\delta \neq 0$, the Bloch vector moves around the axis $\vec{W} = \Omega_R\hat{e}_1 + \delta\hat{e}_3$ at an effective Rabi frequency $\Omega'_R = \sqrt{\Omega_R^2 + \delta^2}$ (see figure 2.2(b)). In the case where $\Omega_R = 0$, only rotations around the $\hat{e}_3$ axis occur at a frequency δ and there is no change in the population of the qubit levels.

In the absence of decoherence ($\Gamma_{DS} = \Gamma_L = 0$), the Bloch vector remains of unit length ($u^2 + v^2 + w^2 = 1$) and points to a position on the surface of the sphere, corresponding to a pure quantum mechanical state. However, with a finite decoherence rate the Bloch vector shrinks in magnitude with increasing time and points inside the Bloch sphere. In this case $u^2 + v^2 + w^2 < 1$, corresponding to a mixed state. Even with an infinite laser coherence length ($\Gamma_L = 0$), this irreversible decay of a pure state into a mixed state is unavoidable where one qubit level is encoded in a metastable state, as in the case with an optical qubit. However, high-fidelity qubit rotations can still be realised if they are implemented on a timescale that is short compared to $1/\Gamma_{DS}$.

Analytical solutions can be found [86] for equations 2.14 that yield

$$\rho_{DD} = \frac{1}{2}(1 - w) = a_D^2 = \frac{\Omega_R^2}{\Omega_R^2 + \delta^2} \sin^2\left(\sqrt{\Omega_R^2 + \delta^2}T\right). \tag{2.16}$$

This dictates the spectral lineshape for pulses of fixed Rabi frequency (i.e. square pulses) and duration $2T$. In chapter 7, a generalisation of the optical Bloch equations is made that allows for a temporally varying Rabi frequency. In this case the equations are solved numerically to find the full dynamics of the Bloch vector for excitation pulses of arbitrary shape.

2.4 Ramsey and spin-echo spectroscopy of a qubit

In Ramsey's spectroscopic technique of separated oscillatory fields [79], two Ramsey excitation pulses are separated by a free precession period, during which there is zero coupling between the qubit and the laser ($\Omega_R = 0$). A schematic of a Ramsey sequence for is shown in figure 2.2(a), where the Bloch vector highlighted in blue represents the state of the qubit *after* the corresponding rotation pulse or free precession period, and the axis of rotation at each stage is highlighted in green. In the case of zero detuning, the first Ramsey pulse performs a $\pi/2$ rotation around the $\hat{e}_1$ axis to create the superposition state $(|S\rangle + i\,|D\rangle)/\sqrt{2}$. Provided that there is no accumulated phase shift between the atomic and laser phase during the Ramsey free precession time τ_R, the Bloch vector does not rotate around the $\hat{e}_3$ axis during τ_R and the Bloch vector is stationary. Subsequently the second Ramsey pulse effects a further $\pi/2$ rotation to completely transfer the population to the $|D\rangle$ state.

For non-zero detuning, the first Ramsey pulse rotates the Bloch vector around $\vec{W}$ to a position near the equator (see figure 2.2(b)). Subsequently a rotation around the $\hat{e}_3$ axis occurs during τ_R at a frequency δ. Finally the second Ramsey pulse performs a further rotation about the $\vec{W}$ axis, with a direction that depends on the phase Φ that accumulates during τ_R. When Φ is an even multiple of π, the rotation continues in the same direction as in the first pulse to the top of the cone defined by the $\vec{W}$ axis. However when Φ is an odd multiple of π the rotation direction is reversed and the second Ramsey pulse returns the Bloch vector to its original position. Therefore Ramsey fringes are observed when the excitation probability is measured as function the detuning of the $\pi/2$ pulses [24, 79]. This is as a consequence of interference between the probability amplitudes associated with each Ramsey pulse.

For a qubit subject to random detuning errors over the many experiments required to characterise a qubit, the Bloch vector undergoes a dephasing during τ_R. In figure 2.2(a), this is represented by a fanning out of the red vectors. Due to this effect, the population is only partially transferred to $|D\rangle$ by the second $\pi/2$ pulse. As the amount of dephasing increases with τ_R, measuring the population

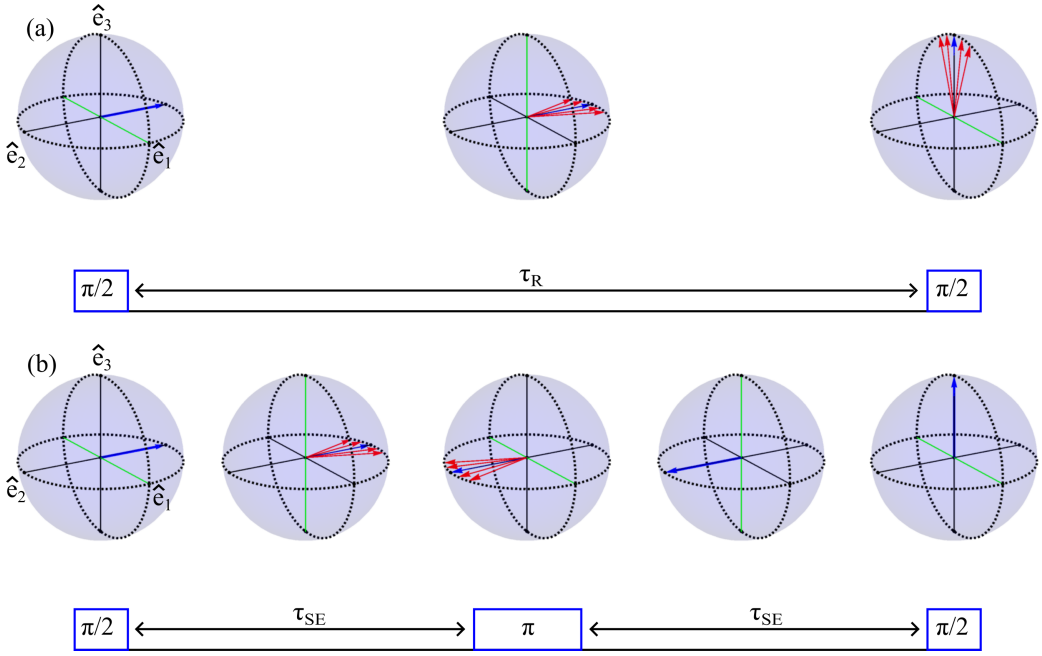

Figure 2.2: Bloch vector (blue) evolution for Ramsey (a) and spin-echo (b) sequences for an qubit initialised in the $|S\rangle$ state. The effects of random detuning errors are represented by the fanned out red vectors. The green line denotes the axis of rotation during each stage of the sequence. In the spin-echo sequence, the phase of the second $\pi/2$ pulse is switched by π in order to produce complete population transfer to the $|D\rangle$ state.

of $|D\rangle$ as a function of τ at $\delta = 0$ offers a convenient method of measuring the decoherence rate of the system.

The spin-echo technique [87] offers a method of protecting the qubit from noise in the environment, which can be manifest for example as random detuning errors as described above. The spin-echo sequence is similar to a Ramsey experiment (see figure 2.2(b)), except two free precession periods τ_{SE} are separated by a resonant π excitation. This extra pulse serves to rotate the Bloch vector to the opposite side of the Bloch sphere. Therefore, if the detuning error is constant during each sequence, any dephasing that occurs in the first free precession period is reversed during the second. The second $\pi/2$ pulse then effectively transfers all of the population to the $|D\rangle$ state. When measuring the excitation probability as a function of the total free precession time, the spin-echo technique therefore

offers an increase in the coherence time of the system over that achievable with a Ramsey sequence.

In general, the spin-echo technique as outlined above is only effective at protecting the qubit from noise sources that have a characteristic period $1/f_{noise}$ that is long compared to the duration of the sequence. However when the free precession time τ_{SE} or τ_R is an even multiple of $1/f_{noise}$, the phase accumulation averages to zero and the coherence is restored to the same level as if the noise were not present. Therefore in a Ramsey or spin-echo experiment, oscillations in the coherence as a function of the total free precession time are observed at $\frac{1}{2}f_{noise}$ when this is the dominant source of decoherence. However the amplitude of this oscillation is greater in the case of a spin-echo experiment, as the extra π rotation induces extra dephasing in the case where τ_{SE} is an odd multiple of $1/f_{noise}$.

2.5 Physical realisation of a qubit

2.5.1 Linear Paul trap

In this work, a single ion is confined in a linear Paul trap to form the basis of a physical qubit. The physics of ion trapping has been documented extensively [12, 88, 89], therefore in this section only a brief outline of the trap operation is given, along with the equations that characterise the motion of the ion in the trap.

A consequence of Earnshaw's theorem is that it is impossible to create a trapping potential minimum using static d.c. field alone. However with a rapidly oscillating electric field it is possible to produce a time-averaged pseudopotential that is trapping in three dimensions. Specifically, a linear Paul trap features an oscillating quadrupole potential which is typically applied to diagonally opposite 'rod' electrodes, as shown in figure 2.3. The potential in the radial plane is

$$\Phi(x, y, t) = \frac{x^2 - y^2}{2r_0^2} V_0 \cos(\Omega_{RF} t), \tag{2.17}$$

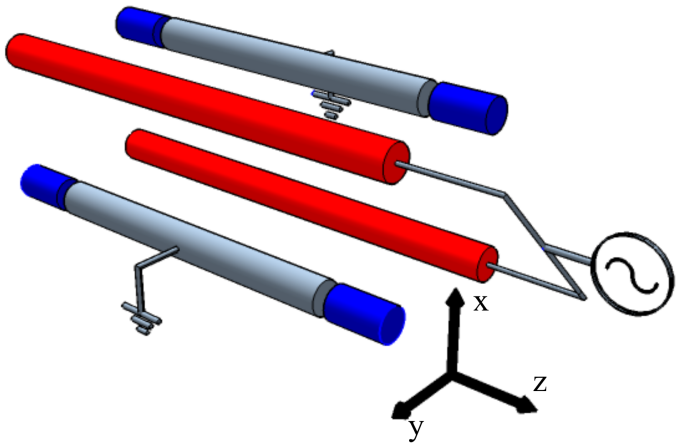

Figure 2.3: Schematic of a linear Paul trap, showing the RF (red), grounded (grey) and d.c. (blue) electrodes.

where Ω_{RF} is the applied frequency, V_0 is the signal amplitude, and r_0 is the shortest distance between the centre of the potential and the electrode. This radial field only provides trapping in two dimensions. To achieve 3-dimensional confinement, a d.c. voltage V_{ec} is applied to the endcaps. Including the axial potential, the equations of motion are

$$\frac{d^2x}{dt^2} + \frac{\Omega_{RF}^2}{4}(a - 2q\cos(\Omega_{RF}t)) = 0, \tag{2.18a}$$

$$\frac{d^2y}{dt^2} + \frac{\Omega_{RF}^2}{4}(a + 2q\cos(\Omega_{RF}t)) = 0, \tag{2.18b}$$

$$\frac{d^2z}{dt^2} + \frac{\Omega_{RF}^2 a}{2} = 0, \tag{2.18c}$$

where q is defined as

$$q = \frac{2eV_0}{Mr_0^2\Omega_{RF}^2}, \tag{2.19}$$

and a as

$$a = \frac{e\kappa V_{ec}}{ML^2\Omega_{RF}^2}, \tag{2.20}$$

where L is the distance between the endcap electrodes and κ is a constant that depends on the trap geometry. The dimensionless numbers a and q are known as the stability parameters, and stable trapping occurs for only certain combinations [12, 90].

Solutions to the equations of motion yield two distinct oscillations; a slow *secular* motion around the centre of the pseudopotential and a fast driven oscillation at Ω_{RF} known as the *micromotion*. The secular frequency along the trap axis is

$$\omega_z = \sqrt{\frac{a}{2}}\Omega_{RF}. \tag{2.21}$$

The secular frequency due to the radial potential alone is

$$\omega_{r0} = \frac{\Omega_{RF}q}{2\sqrt{2}}, \tag{2.22}$$

however the endcap voltage serves to modify the radial potential so that the secular frequencies in the radial direction are modified according to

$$\omega_r = \sqrt{\omega_{r0}^2 - \frac{1}{2}\omega_z^2}. \tag{2.23}$$

For an ideal linear Paul trap, there is zero electric field at the centre of the trap. However an oscillating ion necessarily departs from the trap centre due to its secular motion and therefore directly experiences the confining field. The detrimental effects of the resulting micromotion are discussed in detail in section 4.3 of this thesis, along with practical methods of reducing it.

2.5.2 Trapped-ion qubit

This section proceeds to describe how the absorption and emission properties of a single ion confined in a harmonic potential are modified compared to the general qubit that has been discussed so far. The total Hamiltonian of a single atom trapped in a one-dimensional harmonic potential is given by:

$$\hat{H}_0 = \hat{H}_{atom} + \hat{H}_{trap}, \tag{2.24}$$

$$\hat{H}_{trap} = \frac{\hat{p}^2}{2m} + \frac{1}{2}m\omega\hat{x}^2, \tag{2.25}$$

$$\hat{H}_{atom} = \frac{1}{2}\hbar\omega_{atom}\sigma_z, \tag{2.26}$$

where $\hat{H}_{atom}$ describes the internal energy of the atom and $\hat{H}_{trap}$ describes the motion in the harmonic potential at a secular frequency ω. As the potential is harmonic, the position and momentum operators $\hat{x}$ and $\hat{p}$ are expressed as in the quantum mechanical simple harmonic oscillator:

$$\hat{p} = i\sqrt{\frac{2M\omega}{\hbar}}(\hat{a}^\dagger - \hat{a}), \quad \hat{x} = \sqrt{\frac{\hbar}{2M\omega}}(\hat{a} + \hat{a}^\dagger). \tag{2.27}$$

This enables $\hat{H}_{trap}$ to be re-written in terms of the creation and annihilation operators as follows

$$\hat{H}_{trap} = \hbar\omega(\hat{a}^\dagger\hat{a} + \frac{1}{2}). \tag{2.28}$$

This describes a ladder of equally spaced motional states with energies that are quantised according to

$$E_{trap} = \big(n + \frac{1}{2}\big)\hbar\omega. \tag{2.29}$$

Transitions between motional states are accounted for by a Hamiltonian that describes the interaction between the harmonically-bound two-level atom and a

classical laser field:

$$\hat{H}_{laser} = \frac{1}{2}\Omega_R(|S\rangle\langle D| + |D\rangle\langle S|)\big(e^{i(k\hat{x}-\omega_L t+\phi)} + e^{-i(k\hat{x}-\omega_L t+\phi)}\big). \tag{2.30}$$

Using the spin -$\frac{1}{2}$ algebra

$$|D\rangle\langle S| = \sigma_+ = \frac{1}{2}(\sigma_x + i\sigma_y), \tag{2.31a}$$

$$|S\rangle\langle D| = \sigma_- = \frac{1}{2}(\sigma_x - i\sigma_y), \tag{2.31b}$$

and the expression for the position operator $\hat{x}$ as defined in equation 2.27, $\hat{H}_{laser}$ can be re-written as

$$\hat{H}_{laser} = \frac{1}{2}\Omega_R\Big(e^{-i\eta(\hat{a}+\hat{a}^\dagger)}\sigma_+ e^{-i\omega_L t} + e^{i\eta(\hat{a}+\hat{a}^\dagger)}\sigma_- e^{i\omega_L t}\Big). \tag{2.32}$$

Here the Lamb-Dicke parameter has been defined as

$$\eta = k\sqrt{\frac{\hbar}{2M\omega_i}}\cos\xi, \tag{2.33}$$

where ξ is the angle between the oscillation axis and the wave vector $k{=}|\hat{k}|$. Qualitatively this describes the extent of the ion's motional wavefunction compared to the wavelength of the interrogating laser $\lambda = \frac{2\pi}{k}$. A transformation into the interaction picture is done with the free Hamiltonian H_0 and the interaction Hamiltonian $V(t) = \hat{H}_{laser}$ via $\hat{H}_{int} = \hat{U}^\dagger V(t)\hat{U}$, where $\hat{U} = e^{i\hat{H}_0 t/\hbar}$ to give

$$\hat{H}_{int} = \frac{1}{2}\Omega_R\Big(\sigma_+ e^{i\eta(\hat{a}e^{-i\omega t}+\hat{a}^\dagger e^{i\omega t})}e^{(\phi-\delta t)} + H.c.\Big), \tag{2.34}$$

where δ is the detuning from resonance and $H.c.$ denotes the Hermitian conjugate. Here terms containing $(\omega_L + \omega_{atom})$ have been omitted, i.e. the rotating wave approximation has been made.

Depending on the detuning, this interaction Hamiltonian will couple certain electronic and motional states. An expansion of the exponent containing the creation and annihilation operators results in terms with a combination of $\sigma_\pm$,

with m $\hat{a}^\dagger$ operators and l $\hat{a}$ operators rotating at a frequency $(l-m)\omega = s\omega$. When the detuning $\delta \approx s\omega$, the laser is near-resonant with one of the transitions $|S\rangle|n\rangle - |D\rangle|n+s\rangle$, where $s > 0$ and $s < 0$ are known as blue and red sideband transitions respectively. The Rabi frequency of each transition is given by

$$\Omega_{n,n+s} = \Omega_0 |\langle n+s| e^{-i\eta(\hat{a}+\hat{a}^\dagger)} |n\rangle|, \tag{2.35}$$

where Ω_0 is the Rabi frequency in the motional ground state. In the case where the spatial extent of the ion's wavefunction is much smaller than $1/k$, the interaction Hamiltonian can be simplified. In this *Lamb-Dicke regime*, the equality $\eta^2(2n+1) \ll 1$ is valid and equation 2.34 can be expanded to lowest order in η to give

$$\hat{H}_{LD} = \frac{1}{2}\Omega_0\sigma_+(1 + i\eta(\hat{a}e^{-i\omega t} + \hat{a}^\dagger e^{i\omega t})e^{(\phi-\delta t)}) + H.c., \tag{2.36}$$

which allows three resonances only, which are on the carrier and first order red and blue sidebands. This is desirable regime for experiments, as the spectrum is greatly simplified compared to the general case described by $\hat{H}_{int}$. Specifically, the case $\delta = 0$ gives rise to carrier transitions with the Hamiltonian

$$\hat{H}_{car} = \frac{1}{2}\Omega_0(\sigma_+ e^{i\phi} + \sigma_- e^{-i\phi}). \tag{2.37}$$

These produce no change in the motional state of the ion. In the Lamb-Dicke regime, the dependency of the carrier transition Rabi frequency on the vibrational number n is given as [12, 85]

$$\Omega_R(n) = \Omega_0\Big[1 - \Big(n + \frac{1}{2}\eta^2\Big)\Big]. \tag{2.38}$$

The resonance for $\delta = -\omega$ is known as the first red sideband and is described by the Hamiltonian

$$\hat{H}_{rsb} = \frac{1}{2}\Omega_0\eta(\hat{a}\sigma_+ e^{i\phi} + \hat{a}^\dagger\sigma_- e^{-i\phi}). \tag{2.39}$$

This gives rise to transitions of the form $|S\rangle|n\rangle - |D\rangle|n-1\rangle$, where the Rabi

frequency on the red sideband is given by

$$\Omega_{n,n-1} = \eta\sqrt{n}\Omega_0. \tag{2.40}$$

Similarly the resonance for $\delta = +\omega$ is known as the first blue sideband and is described by the Hamiltonian

$$\hat{H}_{bsb} = \frac{1}{2}\Omega_0\eta(\hat{a}^\dagger\sigma_+ e^{i\phi} + \hat{a}\sigma_- e^{-i\phi}). \tag{2.41}$$

Transitions on the blue sideband are of the form $|S\rangle|n\rangle - |D\rangle|n+1\rangle$ with Rabi frequency

$$\Omega_{n,n+1} = \eta\sqrt{n+1}\Omega_0. \tag{2.42}$$

In summary, in the Lamb-Dicke regime, the absorption spectrum of trapped ion is modified to include a carrier transition and first order sidebands only at $\pm\,\omega$. Absorption on the red and blue detuned sidebands results in a change of the vibrational number n of -1 and $+1$ respectively [12]. This provides a convenient means of manipulating the motional state of the ion, as for example in the case of sub-Doppler cooling as described in chapter 4.

In the above, only an ion trapped in a one-dimensional potential was considered. If the potential is quadratic along each of the three Cartesian coordinate axes, the treatment is extended to three dimensions simply by replacing $k\hat{x}$ in equation 2.30 by the scalar product $\vec{k}\cdot\vec{r}$. The term $\exp(-i\eta(\hat{a}+\hat{a}^\dagger)$ is therefore replaced as $\exp(i\vec{k}\cdot\vec{r}) = \exp\big(i\sum_j \eta_j(\hat{a}_j + \hat{a}_j^\dagger)\big)$, where the index j is over the three normal modes of the harmonic oscillator. The interaction Hamiltonian in three-dimensions is therefore given as

$$\hat{H}_{int-3D} = \frac{1}{2}\Omega_0(\sigma_+ e^{i\sum_j \eta_j\left(\hat{a}_j e^{-i\omega_j t} + \hat{a}_j^\dagger e^{i\omega_j t}\right)} e^{(\phi-\delta t)}) + H.c., \tag{2.43}$$

which dictates that the Rabi frequency of transitions that change the motional number of a single vibrational mode is given by

$$\Omega_{n,n+s} = \Omega_0|\,\langle n+s|\,e^{\left(i\sum_j \eta_j(\hat{a}_j+\hat{a}_j^\dagger)\right)}\,|n\rangle\,|. \tag{2.44}$$

Similarly to the one-dimensional case, this interaction Hamiltonian can be expanded to lowest order in η to give the simplified Hamiltonian in the Lamb-Dicke regime

$$\hat{H}_{LD-3D} = \frac{1}{2}\Omega_0\sigma_+(1 + i\sum_j \eta_j\big(\hat{a}_j e^{-i\omega_j t} + \hat{a}_j^\dagger e^{i\omega_j t}\big)e^{(\phi-\delta t)}) + H.c.. \tag{2.45}$$

This describes a carrier with red and blue sideband transitions at $\pm\omega_j$ only. Again there is zero coupling between the laser and higher order sidebands of any mode. Furthermore, only processes that change the total motional number of the ion by one vibrational quanta are allowed. This includes transitions that lead to a superposition of excitations on two or three motional modes.

In general, the motional state of a trapped ion is not known exactly, but is described by a thermal distribution that depends on the mean vibrational number $\bar{n}$ of each motional mode. The probability of finding the ion in state n in a single measurement is given by [12]:

$$P_n(\bar{n}) = \frac{\bar{n}^n}{(1+\bar{n})^{1+n}}. \tag{2.46}$$

When characterising a qubit in a thermal ($n \neq 0$) state, the final excitation probability is given by the weighted average of rotations at Rabi frequencies $\Omega_R(n)$ according to the distribution of equation 2.46. This dephasing effect due to the thermal state of the ion serves to reduce the length of the Bloch vector in a similar fashion as due to decoherence. This can be avoided when the ion is initialised in the motional ground state with high fidelity.

2.5.3 Strontium

A single isotope of ionised strontium is trapped and manipulated in the experimental work presented in this thesis. The $^{88}Sr^+$ ion has alkali-like structure that is very similar to other species used to realise optical qubits, such as $^{40}Ca^+$. Figure 2.4 shows the relevant lowest lying energy levels, along with the laser wavelengths used for laser cooling, state manipulation and state measurement.

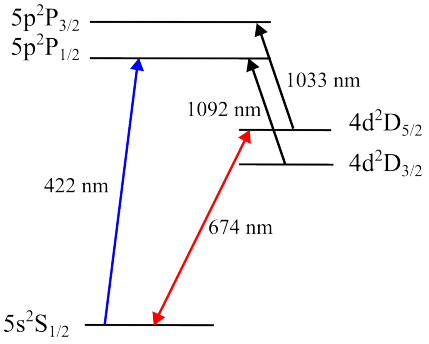

Figure 2.4: Relevant energy levels of the $^{88}Sr^{+}$ ion, with the laser wavelengths used for Doppler cooling, state readout, coherent manipulation and quenching and clearout of the metastable state.

The levels are labelled fully, however shorthand notations are used for energy levels in the remainder of this thesis, apart from those not shown explicitly in the figure. The wavelengths and transition linewidths are also displayed in table 2.1. Conveniently, all of the necessary wavelengths can be produced with solid-state semiconductor diode lasers.

Specifically, the $S_{1/2}$ - $P_{1/2}$ transition is used for Doppler cooling and for state detection via Dehmelt's electron shelving method [91]. As there is a 1/13 probability of the $P_{1/2}$ state decaying to the $D_{3/2}$ state, it is necessary to continuously excite the $D_{3/2}$ - $P_{1/2}$ transition in order to prevent optical pumping to this dark state and thus maintain Doppler cooling. Coherent manipulation is implemented on the narrow $S_{1/2}$ - $D_{5/2}$ quadrupole transition. The upper $D_{5/2}$ metastable level has a radiative lifetime of 0.39 s [29], which is sufficiently long to store information in a quantum processor, however it is often impractical to wait for this long for the ion to decay. Therefore excitation on the $D_{5/2}$ - $P_{3/2}$ transition can be used to return the ion to the ground state via spontaneous decay on the $S_{1/2}$ - $P_{3/2}$ transition on a timescale much shorter than the metastable state lifetime. This transition is referred to as the 'clear-out' when used to re-initialise the ion state after a spectroscopic investigation and as the 'quencher' in the context of frequency-resolved optical pumping and sideband cooling (see chapter 4).

Transition	Wavelength	$\Gamma/2\pi$	Lifetime $\tau = 1/\Gamma$
$S_{1/2}$ - $P_{1/2}$	421.6706 nm [92]	20.22 MHz	7.35 ns [93]
$S_{1/2}$ - $D_{5/2}$	674.02559 nm [94]	0.41 Hz	0.39 s [29]
$D_{3/2}$ - $P_{1/2}$	1091.7860 nm [92]	1.52 MHz	105 ns [93]
$D_{5/2}$ - $P_{3/2}$	1033.01 nm [92]	1.38 MHz	115 ns [93]

Table 2.1: Wavelengths and radiative lifetimes of selected transitions in $^{88}Sr^{+}$.

In a magnetic field, the quadrupole transition is split into 10 Zeeman components (see figure 2.5(a)). The $S_{1/2}$ and $D_{5/2}$ levels are split according to

$$\Delta E = g_j \mu_B B m_j, \tag{2.47}$$

where μ_B is the Bohr magneton, m_j is the relevant magnetic quantum number, B is the magnitude of the applied magnetic field and g_j is the Landé g-factor. For an atom with total angular momentum quantum number J, orbital angular momentum quantum number L and spin angular momentum quantum number S, this is defined as

$$g_j = \frac{3}{2} + \frac{S(S+1) - L(L+1)}{2J(J+1)}. \tag{2.48}$$

If the Landé g-factors for the $^2S_{1/2}$ and $^2D_{5/2}$ levels are $g_{1/2}$ and $g_{5/2}$ respectively, and similarly the magnetic quantum numbers in each level are denoted $m_{1/2}$ and $m_{5/2}$, then the energies of the Zeeman components of the qubit transition are given by:

$$E_{S-D} = \mu_B (m_{1/2} g_{1/2} - m_{5/2} g_{5/2}) B. \tag{2.49}$$

The relative coupling strength of each Zeeman component is a function of ζ, the angle of the $\hat{k}$-vector of the laser with respect the direction of the magnetic field and χ, the angle between the laser polarisation and the plane formed by the magnetic field and laser $\hat{k}$-vector. Figure 2.5(b) shows the quadrupole spectrum for a applied field of $B = 290$ μT with $\zeta = 78°$ and $\chi = 90°$, where the relative coupling strengths are calculated according to the method of James [95]. This

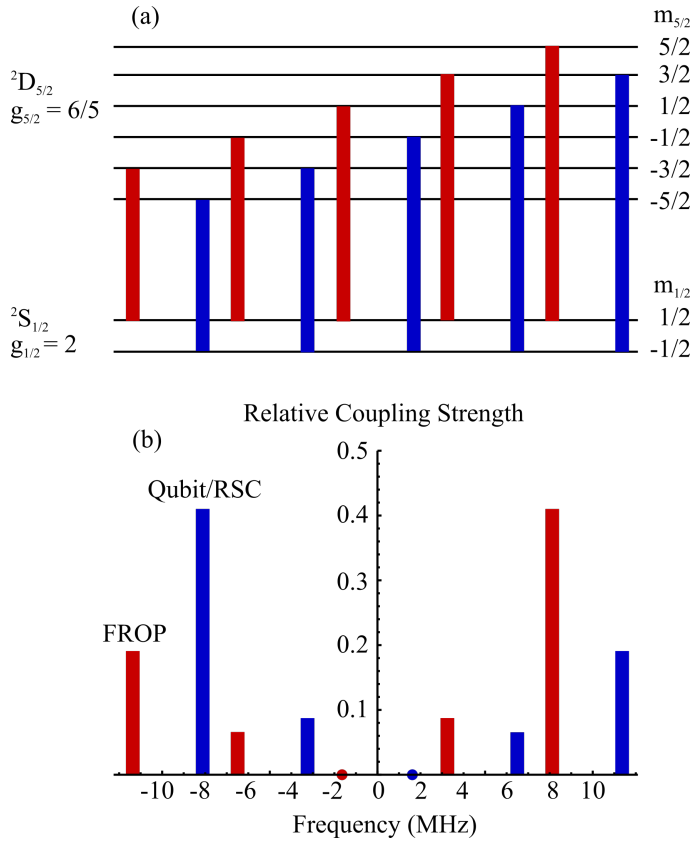

Figure 2.5: (a) Energy level representation of the 10 Zeeman components of the quadrupole transition. Transitions from the $m_{1/2} = -1/2$ Zeeman level are marked in blue, and similarly transitions from the $m_{1/2} = 1/2$ level are highlighted in red. (b) Quadrupole transition spectrum in an applied magnetic field of $B = 290$ μT with the laser polarisation and direction aligned to the magnetic field as described in the main text. The frequencies of the $\Delta m = 0$ transitions are labelled by the circles, although these have zero coupling in this configuration.

configuration is the experimental implementation used in this thesis, as described in detail in chapter 3. The $S_{1/2}(m_j = -1/2)$ - $D_{5/2}(m_j = -5/2)$ transition is used to realise a qubit in this experiment, and is also used for resolved sideband cooling (RSC). The main benefit of using this transition is its high relative coupling strength, however it is more sensitive to magnetic fields than the $\Delta m = 0$ and $\Delta m = 1$ transitions. This choice was largely dictated by geometrical constraints of the experiment, as described in chapter 3. The $S_{1/2}(m_j = 1/2)$ - $D_{5/2}(m_j = -3/2)$ transition is also used in this work for the purpose of frequency-resolved optical pumping (FROP), as described in chapter 4.

Aside from the quadrupole transition discussed above, several of the experimental techniques used in this thesis exploit selection rules of the dipole transitions of the $^{88}Sr^{+}$ ion. These dictate that only certain transitions are allowed depending on the polarisation and $\hat{k}$-vector of the light that is used to excite the ion with respect to the applied magnetic field. Specifically, polarisation resolved optical pumping is implemented on the $S_{1/2}$ - $P_{1/2}$ transition and a method used to zero the ambient magnetic field relies on selection rules on the $D_{3/2}$ - $P_{1/2}$ transition (see chapter 4).

A discussion of allowed transitions begins with Fermi's Golden Rule. This states that the transition rate between levels $|1\rangle$ and $|2\rangle$ due to irradiation by a resonant field with amplitude E_0 is proportional to the square of the matrix element of the perturbation [96]:

$$Rate \propto |eE_0|^2 \times |\langle 2|\, \vec{r} \cdot \hat{e}_{rad}\, |1\rangle|^2. \tag{2.50}$$

Here $e\vec{r}$ is the dipole operator and the polarization vector of the incident field is given as

$$\hat{e}_{rad} = A_\pi \hat{e}_z + A_{\sigma^-} \frac{\hat{e}_x - i\hat{e}_y}{\sqrt{2}} + A_{\sigma^+} \Big(- \frac{\hat{e}_x + i\hat{e}_y}{\sqrt{2}} \Big), \tag{2.51}$$

where the first term corresponds to a linear polarisation along the z axis, and the second and third terms correspond to opposite senses of circular polarisation. In zero magnetic field, the quantisation axis of the atom aligns with the incident polarisation. For example if the polarisation is such that only the first term of equation 2.51 is non-zero, then the atom becomes quantised along the z

axis. Transition rates are calculated by considering only the angular parts of the wavefunction that describes each state as $|1\rangle \rightarrow Y_{l,m}$ and $|2\rangle \rightarrow Y_{l',m'}$, where l and m are the orbital and magnetic quantum numbers respectively. The transition rate is only non-zero under certain conditions for a given polarisation, giving rise to *selection rules*. For linear polarisation ($A_\pi \neq 0, A_{\sigma^-} = A_{\sigma^+} = 0$), the transition rate is zero unless $m = m'$. Therefore the selection rule for these 'π' transitions is $\Delta m = 0$. In this case the total angular momentum of the atom does not change, which is a consequence of linearly polarised light not carrying spin angular momentum. For circularly-polarisation radiation with amplitude A_{σ^+} ($A_\pi = A_{\sigma^-} = 0, A_{\sigma^+} \neq 0$), the transition rate is only non-zero for $m - m' + 1 = 0$, thus enforcing the selection rule $\Delta m = +1$. Similarly the selection rule for light of the opposite circular polarisation is $\Delta m = -1$. Collectively transitions driven with circular polarised light are known as 'σ' transitions.

Application of a small magnetic field results in the quantisation axis of the ion no longer being aligned with the incident polarisation. In this case there is a precession of the magnetic dipole moment of the atom around the applied field at the Larmor frequency. This allows the $\Delta m = \pm 1$ transitions to have a non-zero transition rate even when the driving field is linearly polarised.

2.6 Mølmer-Sørensen gate operation

The Mølmer-Sørensen entangling gate operation [39, 40, 41] generates maximally entangled states of two or more ions by simultaneously addressing the red and blue sideband of a shared motional mode, such as the centre-of-mass (COM) mode. Unlike the Cirac-Zoller gate, the gate does not require both ions to be cooled to the motional ground state, does not require single-ion addressing and is insensitive to heating of the ions during the gate itself. For optical qubits with an energy splitting of ω_{atom}, a bichromatic laser field with frequencies $\omega_\pm = \omega_{atom} \pm \delta$ induces the collective spin flips that drive the gate, with the condition $2\omega_{atom} = \omega_+ + \omega_-$ being satisfied and δ close to the frequency of the centre of mass mode ω_{COM}.

Figure 2.6 shows the principle of the gate operation. Application of the bichromatic field couples the states $|SS\rangle$ and $|DD\rangle$ via four interfering pathways. Neither of the frequency components of the bichromatic field can be absorbed by a

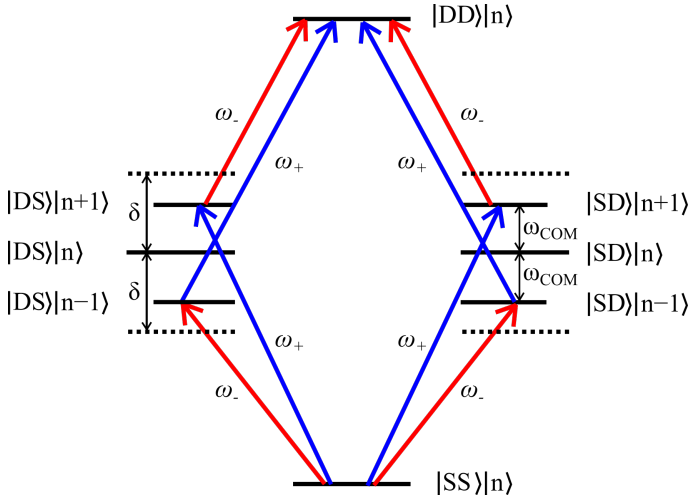

Figure 2.6: The Mølmer-Sørensen gate operation is driven by a bichromatic field with components ω_+ and ω_- that are near-resonant with the blue and red sidebands of the centre-of-mass mode respectively.

single ion, but requires two ions to undergo the $|S\rangle - |D\rangle$ transition simultaneously. Although they act as intermediate states in the process, the $|n+1\rangle$ and $|n-1\rangle$ states are only virtually occupied. The coupling strengths on the $\Omega_{n,n-1}$ and $\Omega_{n,n+1}$ transitions depend on the motional number n as described in equations 2.40 and 2.42 respectively. However the remarkable feature of the Mølmer-Sørensen gate is that the coupling strength on the two-photon $|SS\rangle - |DD\rangle$ transition, calculated by a summation over the four interfering paths [40], is independent of n:

$$\Omega_{SS,DD} = 2\frac{\eta^2\Omega_0^2}{\delta}. \tag{2.52}$$

With the intensity of the bichromatic field set so that $\eta\Omega_0 \approx |\delta - \omega_{COM}|/4$, the initial state $|\Psi\rangle_{k=0} = |SS\rangle$ ideally evolves as follows after k consecutive pulses of

duration $\tau_{MS} = 2\pi/|\omega_{COM} - \delta|$:

$$\begin{aligned} |\Psi\rangle_{k=1} &= |SS\rangle + i\,|DD\rangle \\ |\Psi\rangle_{k=2} &= |DD\rangle \\ |\Psi\rangle_{k=3} &= |DD\rangle + i\,|SS\rangle \\ |\Psi\rangle_{k=4} &= |SS\rangle\,. \end{aligned} \tag{2.53}$$

Hence maximally entangled states are produced when the gate duration is an odd multiple of τ_{MS}.

Chapter 3

Experimental Setup

3.1 Introduction

In this experiment, coherent laser-ion interactions are realised with a single $^{88}Sr^{+}$ ion that is confined in the NPL microfabricated ion trap [97]. The experimental setup used to achieve this is described in this chapter.

An experiment is initialised by ionising atoms from a neutral Sr source through a doubly resonant process [98], starting with excitation by 461 nm light on the $5s^2\ {}^1S_0$ - $5s5p^1P_1$ transition, followed by excitation to the auto-ionising $(4d^2{+}5p^2)^1D_2$ state with 405 nm radiation. Given stable trapping parameters, the ion can then be confined in the linear Paul trap potential. The ion is Doppler cooled on the $S_{1/2}$ - $P_{1/2}$ transition at 422 nm (see figure 2.4, page 27). After reduction of the micromotion, confinement in the Lamb-Dicke limit is achieved.

A typical experimental sequence proceeds as follows (see figure 3.1). Starting from a Doppler cooled ion (1), the ion is optically pumped (2) to the $S_{1/2}(m_j = -1/2)$ state with σ^- polarised 422 nm radiation. A 'repumper' laser resonant with the $P_{1/2}$ - $D_{3/2}$ transition at 1092 nm is applied continuously to close the cooling cycle. After optical pumping with σ^- light, sideband cooling (3) is used to reduce the motional state of the ion below the Doppler cooling limit [22, 27]. This is optionally followed by frequency-resolved optical pumping (FROP) (4), which increases the pumping efficiency beyond what is possible with the σ^- 422 nm light only [25]. Steps (3) and (4) are implemented on the $S_{1/2}$ - $D_{5/2}$ transition

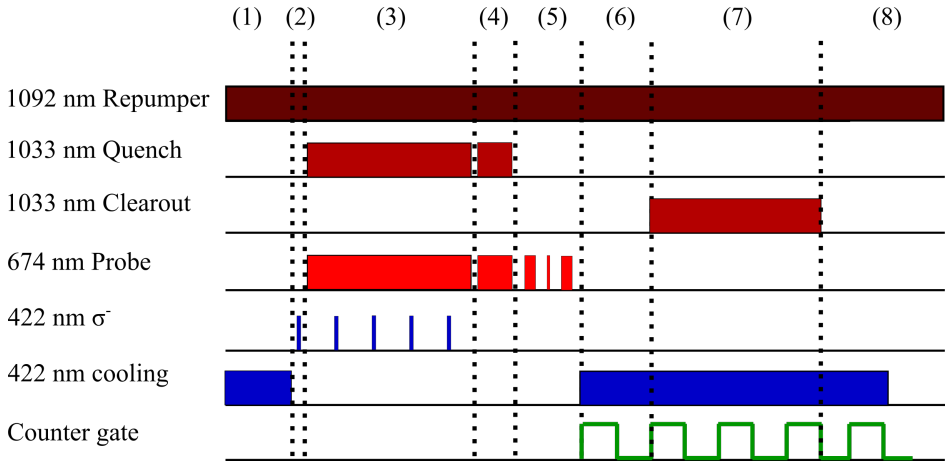

Figure 3.1: A typical experimental sequence. The entire sequence is executed in less than 10 ms.

manifold, and also require quench light resonant with the $D_{5/2}$ - $P_{3/2}$ transition at 1033 nm to maintain process efficiency (see chapter 4). Coherent manipulation (5) follows on the $S_{1/2}(m_j = -1/2)$ - $D_{5/2}(m_j = -5/2)$ component of the Zeeman manifold. State measurement (6) is then carried out with the Dehmelt electron shelving method [43] by imaging state-dependent fluorescence at 422 nm. If the ion is measured to be in the excited state, the 1033 nm clearout (7) is applied to return the ion to the ground state.

This chapter is organised as follows. Section 3.1 provides a basic outline of the experimental routine that dictates the required apparatus in the lab. Section 3.2 details the ion trap, the associated RF drive system, the electrical connectivity of the apparatus and the ultra-high vacuum (UHV) system. In section 3.3 the optical systems are presented and the arrangement of laser beams is described, as are the systems used to image the state-dependent fluorescence. Finally in section 3.4 the experimental control system is described.

3.2 Ion trap apparatus

3.2.1 Microfabricated ion trap

The trap used in this experiment is of a unique 3-dimensional design and is realised with a monolithic fabrication process [97, 99]. The trap electrodes are formed on both sides of an oxidised silicon substrate, see figure 3.2. The ion is trapped in the middle of a 340 μm aperture that is etched through the silica and silicon layers. Gold is patterned onto the silica to form low dissipation electrodes. The silicon is undercut by 235 μm under each aperture edge, which allows the RF electrodes to wrap around the underside of the silica layer. A 50 μm gap between the RF electrodes on the inner side and the silicon substrate minimises the chance of electrical breakdown. On the chip surface, the RF track electrodes are separated by 50 μm from the compensation electrodes (co1, co2, co3) of 340 μm axial length. All electrodes on the RF track side of the aperture are separated by regions of exposed silica. On the other side of the aperture, d.c. electrodes (dc1, dc2, dc3) are formed in alignment with the compensation electrodes, and are isolated from each other by regions where the silica has been etched away. Endcap electrodes (ec1, ec2) of 500 μm axial length are formed either side of the d.c. electrodes to complete the trap geometry. All other areas of the chip surface are metallised with gold and are grounded. The same electrode arrangement is repeated on the reverse side of the chip.

The trap efficiency ϵ is the ratio of the harmonic component of the trapping potential relative to that created by ideal hyperbolic electrodes with the same ion-electrode separation. The quadrupole part of the microtrap potential $\Phi_{MT}(x, y, t)$ differs from that of an ideal hyperbolic trap $\Phi(x, y, t)$ (equation 2.17, page 19) by only the this factor ϵ:

$$\Phi_{MT}(x, y, t) = \epsilon \frac{x^2 - y^2}{2r_0^2} V_0 \cos(\Omega_{RF} t). \tag{3.1}$$

A high trap efficiency is desirable as anharmonic terms cause the ion's motion to be non-linear, with oscillation frequencies depending on the oscillation amplitude. As the aperture width of the NPL trap is the same as the wafer thickness, the microtrap has a unit aspect ratio. This dictates a high trap efficiency of $\epsilon = 0.72$

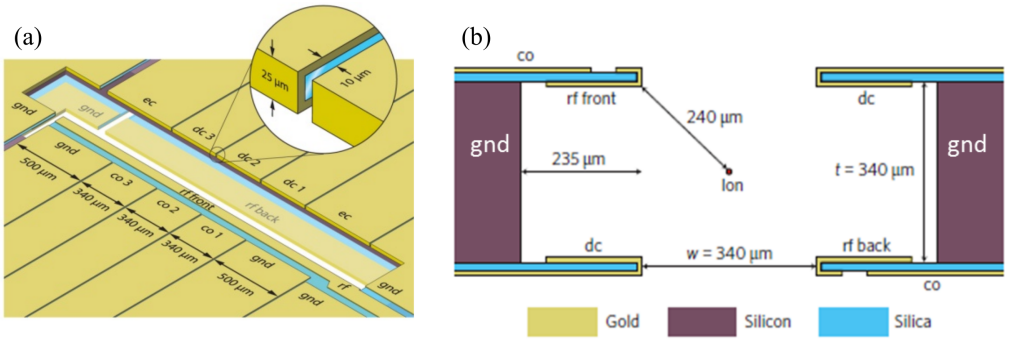

Figure 3.2: Schematics of NPL microfabricated ion trap. (a) The arrangement of dc, compensation (co), endcap (ec) and RF electrodes on one side of the chip. The same geometry is repeated on the reverse. (b) The same electrode geometry in cross-section.

[97, 100] (compared to $\epsilon = 1$ for an ideal hyperbolic trap). The silicon substrate is highly n-doped (resistivity $= 2.6 \times 10^{-3}$ Ω cm), which minimises the ion dieletric exposure, as well as reducing the heating effect due to capacitive coupling of the RF to the grounded substrate. Less than 1 mW is dissipated in the device under typical operating conditions.

3.2.2 Electronic addressing and vacuum system

The trap chip is mounted in a compact electronic package [101], consisting of a modified ceramic 84-pin leadless chip carrier (LCC), a double sided aluminium nitride substrate (AlN) and the microtrap chip itself. The AlN is sandwiched between the LCC and the microtrap chip in an epoxy bonded stack. This allows electrical connectivity between the single sided LCC and the reverse side of the microtrap chip by means of electrical vias in the AlN. The connections between layers of the stack are made by wire bonds. The pins on two opposite sides of the LCC are used for the d.c. connections (21 per side), and a third side is used for the RF connection. The RF signal is provided by an analogue synthesiser that is amplified by a helical resonator [102] to produce the voltage required for ion trapping. The resonator is operated at a resonant frequency of $\Omega_{RF} = 8.2$ MHz with a quality factor $Q = 180$.

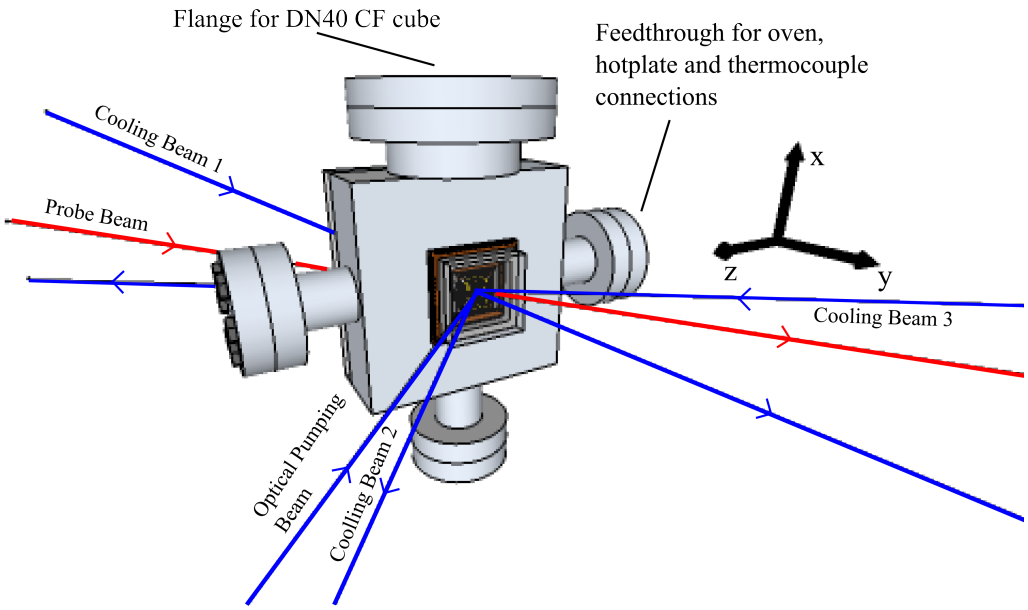

Figure 3.3: Schematic of the custom made UHV system with the LCC, spacer and small optical window. The RF and d.c. connectors are not shown.

The electronic package is indium sealed onto custom made UHV chamber (see figure 3.3). A second indium seal between a steel spacer and the LCC forms the boundary between vacuum and air, allowing electrical pathways of < 20 mm from the LCC air-side pins to the trap electrodes. The spacer increases the distance between the microtrap and a dielectric window (25.4 $\times$25.4 mm), itself attached to the spacer with a third indium seal. A larger (70 $\times$70 mm) window is attached to the rear side of the chamber with a final indium seal. The custom vacuum package shown connects to one port of a DN40 CF cube, to which a 20 l/s ion pump, non-evaporable getter and ion gauge are also attached. The chamber pressure is maintained at 1×10^{-11} mbar.

Sr vapour is produced in a two stage process similar to that used by DeVoe [98, 103]. An oven containing a SrO:Ta mixture is heated to ~ 800 °C to evaporate Sr onto a tantalum hotplate. This is in turn heated to ~ 200 °C to create high purity Sr vapour in the trapping region. Thermocouples allow the oven and hotplate temperatures to be monitored during loading.

3.3 Optical systems

3.3.1 422 nm Doppler cooling laser

422 nm light is used to Doppler cool the ion on the $S_{1/2}$ - $P_{1/2}$ transition and to optically pump the ion into the $S_{1/2}(m_j = -1/2)$ Zeeman sub-level. It is derived from a frequency-doubled extended-cavity diode laser (ECDL) at 843 nm in the Littrow configuration (see figure 3.4). The output from an anti-reflection coated laser diode is collimated and is incident on diffraction grating at the Littrow angle to form the external cavity. To reduce the drift of the fundamental laser, a side of fringe lock is used to stabilise the laser to a tunable etalon (finesse = 115). An intensity independent error signal is generated by dividing the cavity reflection (PD1) and monitor (PD2) photodiode signals. This provides feedback to laser diode current and the ECDL grating angle (PZT1).

To generate 422 nm light, 30 mW of 844 nm is incident on a doubling cavity containing a single potassium niobate ($KNb0_3$) crystal that is non-critically phase matched at T = -17 °C [104]. One of the cavity mirrors is mounted on a piezoelectric mount (PZT3), enabling fine tuning of the cavity length. This is maintained in resonance with the laser fundamental frequency by means of a Hänsch-Couillaud polarisation lock [105]. By monitoring PD3, PD4 and PD5, an error signal is used to generate feedback to PZT3. In lock, 3 mW of power at 422 nm is produced.

The frequency stability derived from the side-of-fringe lock is not sufficient to maintain Doppler cooling. Fortuitously, a suitable absolute reference is found in the $5s^2S_{1/2}$ - $6p^2P_{1/2}$ transition in ^{85}Rb [106]. This lies 440 MHz below the Doppler cooling transition in $^{88}Sr^+$, which is conveniently bridged by an acousto-optic modulator (AOM). A portion of doubling cavity output is appropriately frequency shifted by AOM1 and is then incident on a rubidium cell to form a saturated absorption lock. The resulting error signal is integrated and provides feedback to PZT4, which dictates the length of the reference cavity. When the frequency applied to AOM1 by a voltage controlled oscillator (VCO) is varied, the reference cavity length is shifted by virtue of the saturated absorption lock.

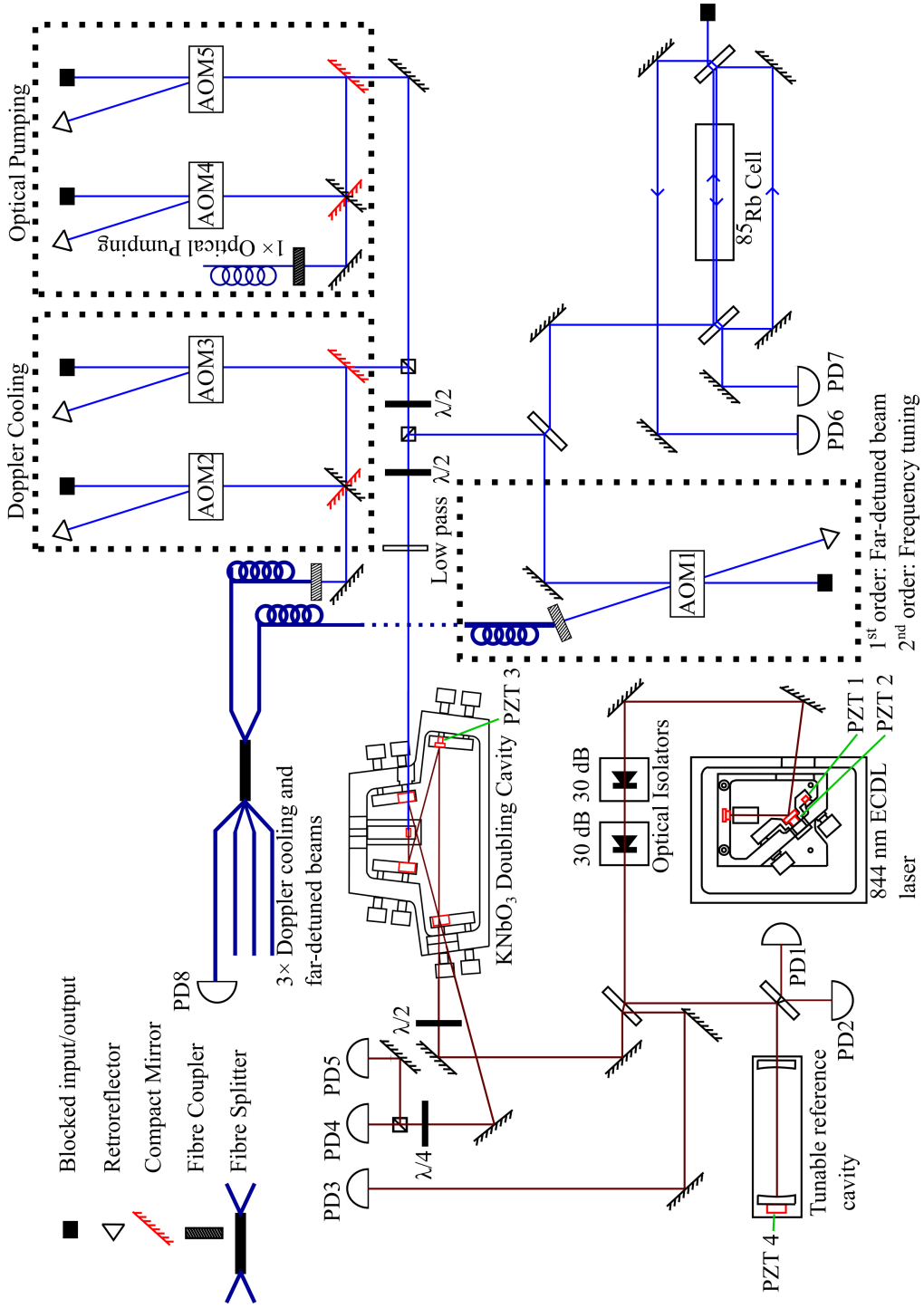

Figure 3.4: Schematic of the 422 nm laser. Pairs of double pass AOMs provide high extinction switching of the Doppler cooling and optical pumping beams. Light after a single pass of AOM1 forms the far-detuned beam. Similarly the double-passed beam provides a frequency tunable signal for the saturation absorption lock.

Hence the 422 nm laser frequency can be conveniently set by altering the voltage that is applied to the modulation input of the VCO.

The 422 nm output is split into several paths. The Doppler cooling signal goes via two double-pass AOMs (AOM2 and AOM3) and is coupled into one input of polarisation maintaining (PM) 2×4 fibre splitter. The other input is formed of light which is picked off after the first pass of AOM1. This forms a far-detuned Doppler cooling beam for use in trap loading only. An optical pumping beam takes a similar path via AOM4 and AOM5, and is injected into a separate PM fibre. The Doppler cooling and optical pumping beams are switched with high extinction at the ion due to the two AOM double passes and fibre coupling. PD8 is used to monitor the 422 nm output during experiments.

Therefore the three outputs are:

1) 3 Doppler cooling outputs, each with ~ 1.5 μW at the ion with a waist diameter of $2w_0 = 70$ μm. Only one beam is required for Doppler cooling, however three are needed for full micromotion compensation.

2) 3 far-detuned outputs each with ~ 20 μW to cool initially hot ions immediately after photoionisation.

3) An optical pumping beam output with 1.5 μW at the ion with a waist diameter of $2w_0 = 70\mu$m. The beam is passed through a Glan-Taylor polariser and Berek compensator to produce σ^- polarised light at the ion (the latter compensates for phase shifts induced by birefringence of the optical window, see section 4.6.1).

3.3.2 1092 nm 'repumper' laser

Light at 1092 nm is used to depopulate the $D_{3/2}$ dark state via excitation to the $P_{1/2}$ state. The light is generated from a neodymium-doped (Nd $^{3+}$) fibre laser with an 825 nm diode pump (see figure 3.5). A diffraction grating couples light back into the fibre to form the laser cavity.

The laser frequency is not actively stabilised and always has multi-modal operation; longitudinal modes are separated by 1 MHz under a 1.5 GHz wide envelope. The wavelength of the laser can be coarsely altered by changing the angle of the intra-cavity etalon, and fine tuning can be carried out by adjusting

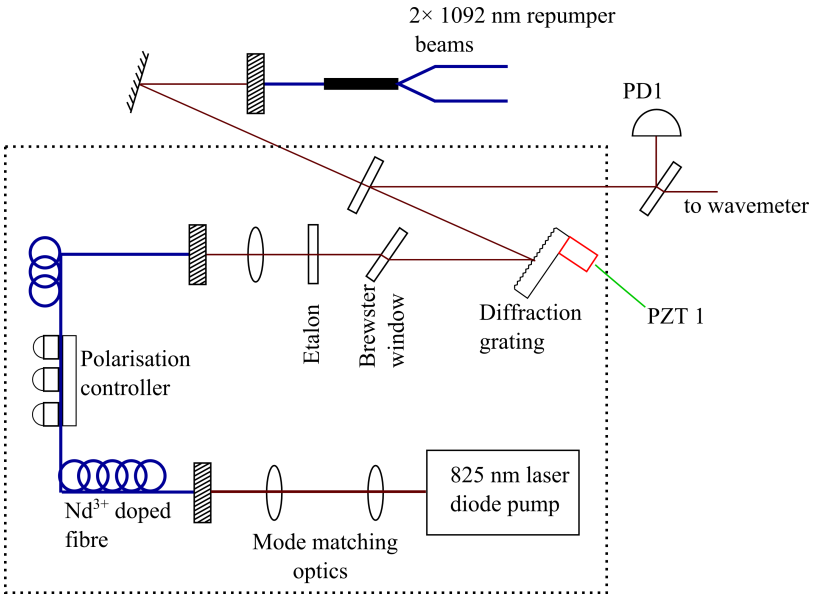

Figure 3.5: Schematic of the 1092 nm laser. Fine tuning of the centre wavelength of the multi-modal envelope is implemented by changing the voltage applied to PZT1. The beam is not shuttered.

the angle of the diffraction grating via its piezo mount (PZT1). A polarisation controller is used to match the output polarisation to the angle at which the grating is maximally reflective.

The laser output is coupled into a 1×2 fibre splitter to provide two outputs, each of which delivers ~ 1.8 mW of 1092 nm light to a spot size of $2w_0 = 580$ μm at the ion. One output goes through a Glan-Taylor polarisor and half-wave plate, producing a beam of rotatable polarisation which is used in a procedure to minimise the ambient magnetic field (see section 4.4). The second beam is additionally employed to maintain fluorescence when working in zero magnetic field. PD1 is used to monitor the laser output power.

3.3.3 461 nm photoionisation laser

Light at 461 nm is required for the first part of the photo-ionisation process; the $5s^2\ {}^1S_0$ - $5s5p^1P_1$ transition. An ECDL at 922 nm, similar in design to the 844 nm laser described in section 3.3.1, produces up to 35 mW of output power

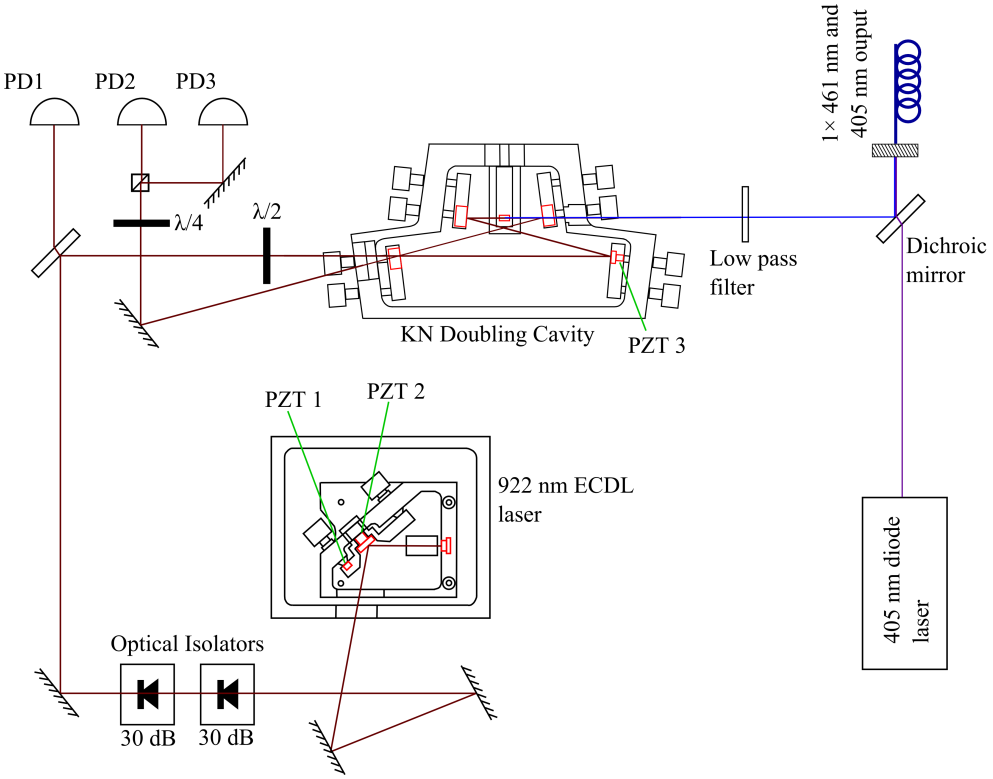

Figure 3.6: Schematic of the 461 nm and 405 nm photoionisation lasers. The two wavelengths are overlapped on a dichroic mirror and coupled into a single fibre coupler.

(see figure 3.6). A doubling cavity, again similar to the one described in section 3.3.1, is used to frequency double the 922 nm light. Critical phase matching is achieved using angle tuning of the crystal.

The cavity length is locked to the fundamental laser wavelength with the Hänsch-Couillaud lock [105] (using PD1, PD2, PD3) to provide feedback to PZT3, enabling 2 mW of 461 nm light to be produced. This is coupled into a single mode PM fibre, the output of which provides 600 μW of signal into a spot size of $2w_0 = 200$ μm. The laser frequency is not stabilised, but is set to the appropriate value by monitoring the wavemeter and manually adjusting the voltage applied to PZT1. The beam is switched with a mechanical shutter.

3.3.4 405 nm photoionisation laser

The 405 nm laser excites the $5s5p^1P_1$ - $(4d^2{+}5p^2)^1D_2$ transition, leaving the ion in the auto-ionising state, from where one valence electron is ejected into the continuum, and the other decays back to the ground state. The transition has a very broad linewidth of 0.9 nm, therefore laser stabilisation techniques are not required. The output of free-running laser diode at 405 nm is overlapped with the 461 nm beam on a dichroic beam splitter and is coupled into the same fibre (see figure 3.6). 5 mW of 405 nm light is focused to a spot size of $2w_0 = 180$ μm at the ion. The 405 nm beam is also switched with a mechanical shutter.

3.3.5 1033 nm quench/clearout laser

Light at 1033 nm is applied to return the ion to the ground state after making the transition to the metastable $D_{5/2}$ state. In sideband cooling, this 'quenches' the excited state to allow for an effective cooling rate. After the ion is measured to be in $D_{5/2}$ in a spectroscopy experiment, 1033 nm light is applied to 'clearout' the ion to the ground state so that the next experimental cycle can begin.

Up to 40 mW of 1033 nm light is produced from an ECDL, similar in design to the 844 nm laser (see figure 3.7). The beam is aligned into two separate fibre coupler inputs. One forms the input to a 2×2 fibre splitter; one output goes to the wavemeter, and the other to a side-of-fringe lock to a low drift cavity. Ultra-low expansion (ULE) glass is used for the cavity mirror substrate, backplate and spacer material, as shown in cross-section in figure 3.7. One of the mirrors is fixed to one end of the cavity spacer, and the other is attached to a backplate by an inner set of actuators (AS1). The backplate is in turn attached to the spacer material with a second set of actuators AS2. A tunable high voltage is applied to AS1, whilst AS2 is grounded. This yields a tunable cavity (finesse = 275) that is approximately insensitive to the thermal expansion of the actuators.

The cavity is mounted in a compact vacuum chamber that is evacuated to 10^{-6} mbar. The vacuum chamber is temperature stabilised to $\pm$ 1mK and is situated in a thermal enclosure that is itself stabilised to $\pm$ 5mK. A drift rate of 2 MHz/hr was measured when the laser is locked to the low drift cavity. PD1

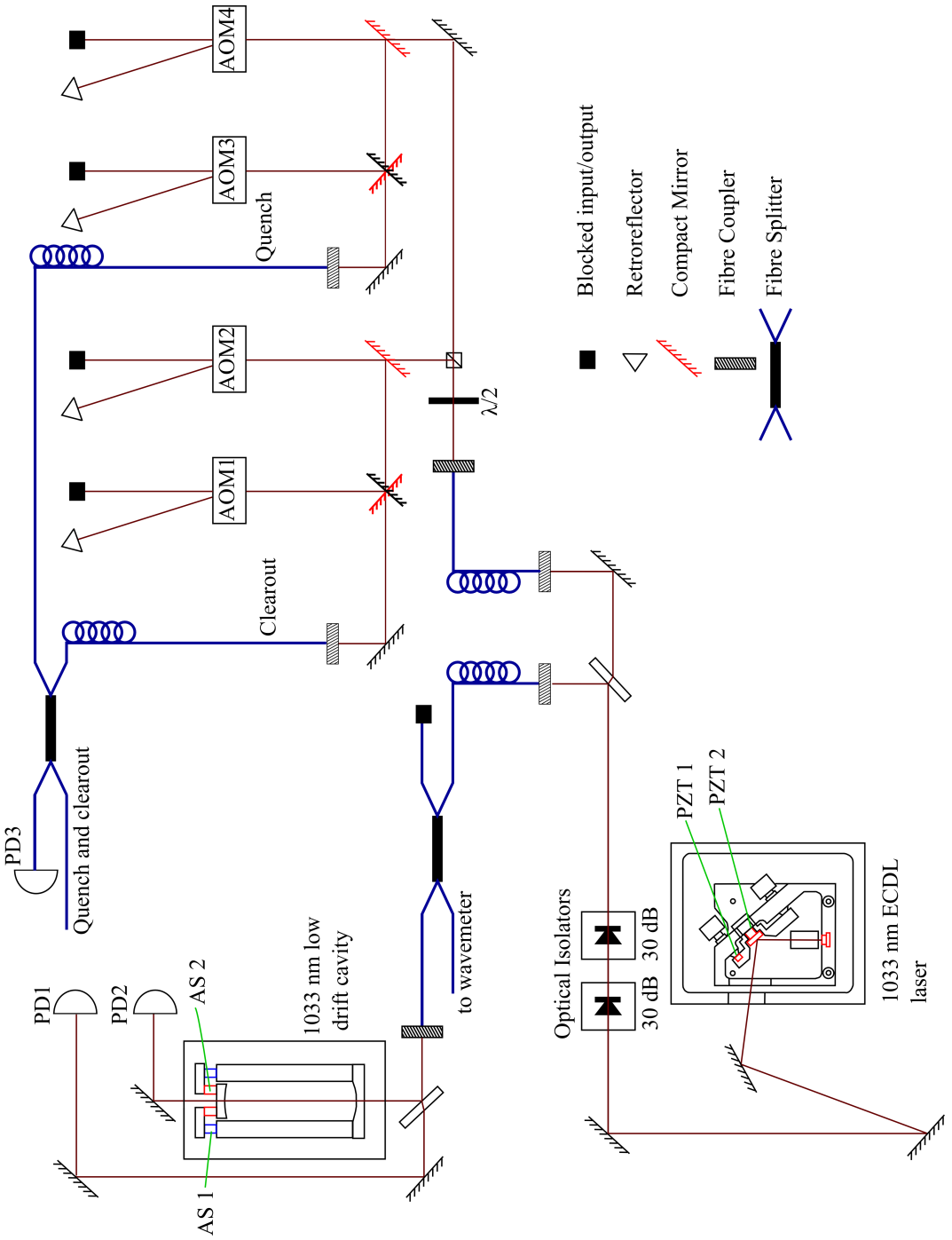

Figure 3.7: Schematic of the 1033 nm laser. Pairs of double pass AOMs provide high extinction switching of the quench and clearout beams. A side-of-fringe lock to a ULE cavity reduces the frequency drift of the laser.

and PD2 are used to generate an intensity-independent error signal, as described in section 3.3.1.

The other fibre coupler output takes light to an AOM setup. Here the beam is divided into two paths. Each path consists of two double-pass AOMs to form the quench (AOM3 and AOM4) and clearout (AOM1 and AOM2) beams, each of which can be switched independently and with high extinction. The AOMs are arranged so that the quench beam is 300 MHz detuned from the clearout, as required for sideband cooling (see 4.6.3). The two beams are inputs to a 2×2 fibre splitter, and one of the outputs delivers both frequencies to the trap. Up to 700 μW and 100 μW of clearout and quench light respectively is focused to a spot diameter of $2w_0 = 180$ μm. The other output is used for monitoring the 1033 nm pulses with PD3.

3.3.6 674 nm laser

Light at 674 nm is used for spectroscopy of the $S_{1/2}$ - $D_{5/2}$ transition, and for state preparation in sideband cooling and frequency-resolved optical pumping. The construction of an agile and stable laser at 674 nm forms a significant part of the work of this thesis, and is described in detail in chapters 5 and 6.

3.3.7 Arrangement of laser beams and magnetic field coils

All of the laser beams are delivered to the ion trap via fibre. This increases the beam alignment stability and beam quality at the ion compared to free space delivery. Table 3.1 shows a summary list of all the beams entering the trap with their vector direction and $2w_0$ spot size at the ion. Furthermore the 422 nm and 674 nm beam directions are displayed graphically in figure 3.3. The beams can enter the vacuum chamber at a wide range of angles due to the $\sim 0.7\pi$ sr of optical access on each side. Orthogonal pairs of magnetic field coils in $\hat{x}$, $\hat{y}$ and $\hat{z}$ cancel the ambient field. Also, an additional a pair of coils creates a magnetic field parallel to the optical pumping beam. This creates a bias field that lifts the degeneracy of the quadrupole transition.

Wavelength	Beam	$2w_0$ (μm)	Unit Vector
405 nm and 461 nm	Photoionisation	200	0.00 $\hat{x}$ - 0.79 $\hat{y}$ - 0.62 $\hat{z}$
422 nm	Cooling 1	70	-0.18 $\hat{x}$ + 0.84 $\hat{y}$ + 0.52 $\hat{z}$
422 nm	Cooling 2	70	0.00 $\hat{x}$ + 0.89 $\hat{y}$ - 0.45 $\hat{z}$
422 nm	Cooling 3	70	- 0.18 $\hat{x}$ - 0.84 $\hat{y}$ - 0.52 $\hat{z}$
422 nm	Opt. Pumping	70	0.00 $\hat{x}$ - 0.75 $\hat{y}$ + 0.67 $\hat{z}$
674 nm	Probe	45	0.00 $\hat{x}$ + 0.80 $\hat{y}$ + 0.60 $\hat{z}$
1033 nm	Quench and Clearout	180	- 0.34 $\hat{x}$ + 0.81 $\hat{y}$ - 0.45 $\hat{z}$
1092 nm	Repumper 1	580	0.00 $\hat{x}$ - 0.87 $\hat{y}$ + 0.48 $\hat{z}$
1092 nm	Repumper 2	580	0.00 $\hat{x}$ - 0.87 $\hat{y}$ - 0.48 $\hat{z}$

Table 3.1: Beam directions and $2w_0$ spot sizes of the 9 separate beams that are aligned to the ion. The 422 nm and 674 nm beam directions are displayed in figure 3.3.

3.3.8 Imaging systems

State detection requires fluorescence on the $S_{1/2}$ - $P_{1/2}$ transition to be collected and detected. High numerical aperture (NA = 0.43) lenses are positioned on each side of the trap to give a magnification of ~ 10 at the focal point. Each lens covers $\sim 0.25\pi$ sr of the $\sim 0.7\pi$ sr available due to the trap geometry. A photomultiplier tube (PMT) and a electron multiplying CCD camera measure fluorescence on the large and small window sides of the trap respectively. Both are fitted with optical filters that effectively block out 674 nm, 1033 nm and 1092 nm light. The 405 nm and 461 nm beams are detected by both instruments, however these are only used during trap loading and have no effect on state detection. In typical experiments, only cooling beam 2 is used, which has a background count rate due to electrode scatter of ~ 300 s^{-1}. The PMT dark count with all laser beams extinguished is ~ 10 s^{-1}.

3.4 Experimental control

All of the experimental sequences and data collection are handled by one National Instruments PXI machine, containing four individual cards (see figure 3.8). A high precision counter/timer card (NI PXI-6608) is used to measure the count rate from the photomultiplier tube (PMT) and generates a clock signal for a high speed digital I/O card (NI PXIe-6537). This provides 32 independent TTL signals that switch the AOMs and mechanical shutters to create the desired pulse sequences. An analogue output card (NI PXI-6733) is used to provide the d.c voltages for the endcap and compensation electrodes, and to provide the modulation input to the VCO to set the 422 nm laser frequency (see section 3.3.1). Finally an analogue input card (NI PXI-6254) is used to monitor all the photodiode signals in the lab. All of the cards are linked by high-precision trigger lines, enabling timing synchronisation between cards. All RF sources and the master oscillator in the PXI chassis are phase-locked to a stable 10 MHz reference signal, which is derived from a local hydrogen maser.

At the start of each experiment, the digital I/O card is loaded with a pattern that defines the logical state of all 32 lines at a specified number of time intervals. The card toggles between these states on each rising edge of the clock signal; a frequency of 100 kHz is used, so that the timing resolution of pulse lengths etc. is 10 μs. One TTL line is connected over the PXI Trigger to the counter/timer card, and is used to trigger the start of fluorescence counting so that it is simultaneous with the return of the 422 nm cooling light during state measurement.

The 674 nm laser pulse sequences are created by using two commercial (Toptica VFG150) direct digital synthesis (DDS) sources. DDS1 controls the RF modulation frequency of the sideband injection lock, and DDS2 provides the agile RF pulse sequences that drive the 674 nm laser double pass AOM (see chapter 5). Before each interrogation cycle, the internal buffer of each DDS is loaded with a set of commands (over USB 2.0) that defines the RF pulse sequence. The sequences are executed when the DDS sources receive a shared trigger pulse from the digital I/O card, which is defined in the pattern so the 674 nm pulses are synchronised with the rest of the experiment. An ORTEC amplifier/discriminator is used to convert the a.c. signal from the PMT into TTL pulses, which are counted by the NI PXI-6608.

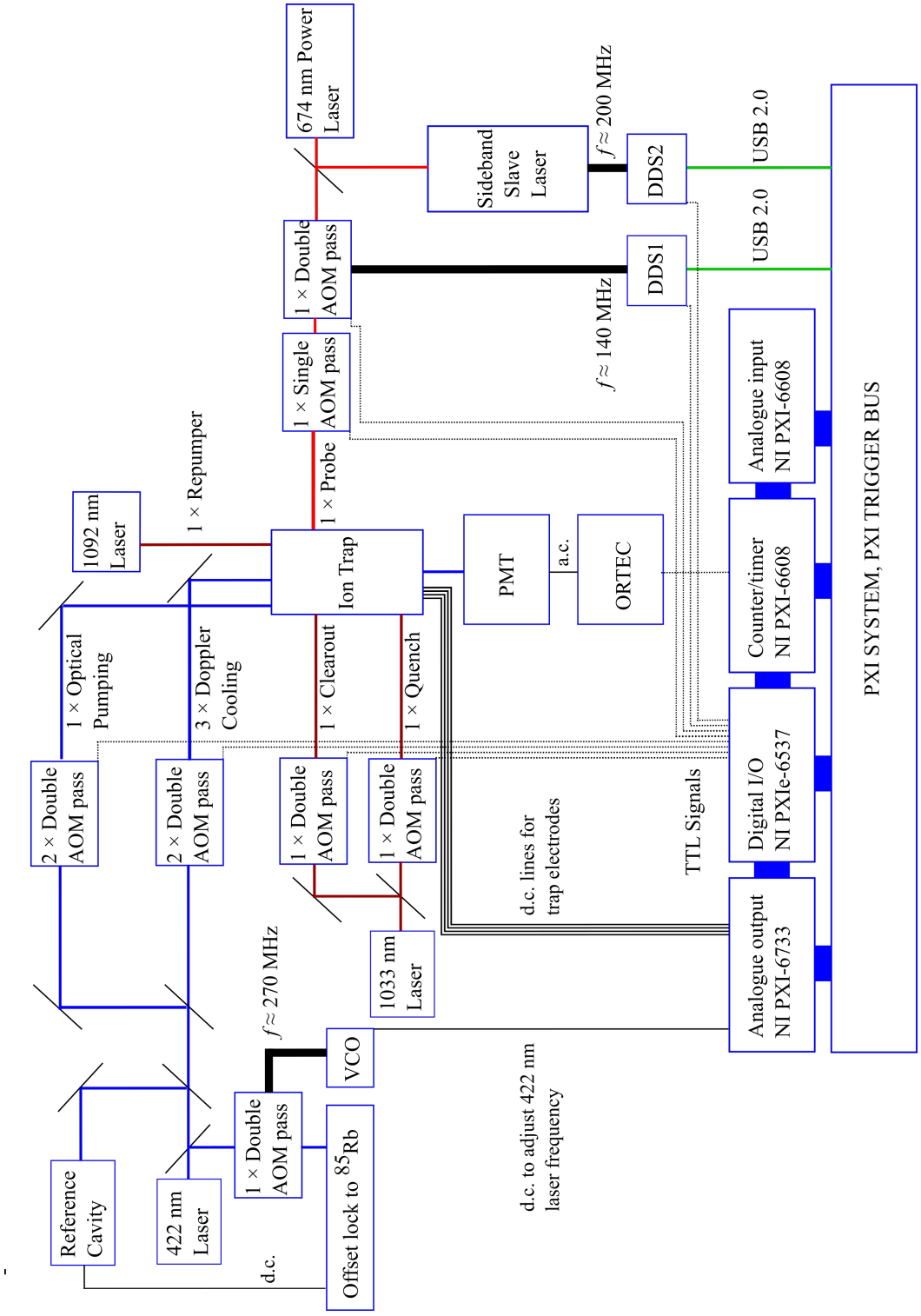

Figure 3.8: Schematic of the experimental control system. The PXI system is used to configure laser pulse sequences, count ion fluorescence and provide the d.c. voltages for the trap electrodes and the offset lock for the 422 nm laser.

3.5 Summary

The experimental apparatus used in the work presented in the rest of this thesis, with the exception of the 674 nm laser, has been described in this chapter. Firstly a brief description of the NPL microtrap was given, along with details of its installation in a UHV environment and electrical connectivity. An account of the various laser systems was also given, as well as a description of the arrangement of the laser outputs with respect to the microtrap. Particularly, the 1033 nm low drift cavity was constructed and installed in the course of this thesis. Finally the experimental control system was described; this has been significantly updated during this work to enable the agility and stability of the 674 nm laser system, as described in chapters 5 and 6.

Chapter 4

Experimental Techniques

4.1 Introduction

There are several experimental prerequisites that must be fulfilled before high-fidelity gate operations with trapped ions can be attempted. To achieve confinement in the Lamb-Dicke regime, it is necessary for the spatial extent of the ion's motion to be much smaller than the wavelength of the interrogating laser. To achieve this, the ion must be Doppler cooled in order to reduce the size of its motional wavepacket. Furthermore, the ion must be positioned at the RF null of the pseudopotential in order to minimise excess micromotion. The Zeeman splitting of the quadrupole transition must be precisely controllable; this with a measurement of the secular frequencies provides complete information of all the transition frequencies to be used in a gate operation. Also for the gate fidelity not to be limited by imperfect state preparation, the internal and external state of the ion must be initialised with high fidelity. Finally, to realise QIP with trapped ions, deterministic transport of ions between trapping segments of a microtrap is desirable [8].

This chapter details the experimental techniques used to satisfy the above requirements. Following a brief description of the Doppler cooling of a single $^{88}Sr^{+}$ ion and the related method of measuring the ion state, an account of the first full micromotion minimisation in the microtrap is given. A method of minimising the magnetic field at the ion, based on optical pumping to a dark state with the

1092 nm laser, is also described. After this step, a well defined bias field can be applied to implement precise splitting of the Zeeman components. Together with a measurement of the secular frequencies using Rabi spectroscopy, this enables complete determination of the quadrupole spectrum. Two methods of preparing the ion in a specific Zeeman sub-level are also presented; the second of which is a frequency-resolved technique which is demonstrated here for the first time with $^{88}Sr^{+}$. An account of the progress towards ground state cooling in the microtrap is also given. Finally, the first demonstration of basic ion transport in the microtrap architecture is presented.

4.2 Doppler cooling and state readout

After photoionisation [98] and trapping in the pseudopotential, Doppler cooling is implemented in order to reduce the energy of the ion to a level where confinement in the Lamb-Dicke regime is possible. This is a well established technique [107, 108, 109] that relies on momentum transfer between a laser beam and the atomic sample. In this experiment, the 422 nm cooling laser is detuned by -$\Gamma_{eff}/2 = 2\pi$ 20 MHz from the $S_{1/2}$ - $P_{1/2}$ transition to provide optimal cooling [85, 108], where Γ_{eff} is the effective transition linewidth due to saturation broadening and Zeeman splitting. The three cooling beams are each oblique to all three of the principal trap axes (see figure 3.3), and can therefore maintain Doppler cooling independently. However, three beams are required for full micromotion minimisation in the three spatial dimensions (see section 4.3). At this detuning, cooling with each beam produces a measured fluorescence rate of $\sim 2{\times}10^4$ s^{-1} for a Doppler cooling beam power of ~ 1.5 μW and spot size of $2w_0 = 70$ μW. The resulting Gaussian beam intensity I relates to the saturation intensity [96] I_{sat} of the $S_{1/2}$ - $P_{1/2}$ transition as $I/I_{sat} = 2$.

Dehmelt's electron shelving technique [91] provides a convenient means of measuring the state of the ion. Starting from the $S_{1/2}$ state, the ion can cycle on the Doppler cooling transition and a count rate of $R_S = 2{\times}10^4$ s^{-1} is observed on the PMT. However when the ion is in the 'shelved' $D_{5/2}$ state, it can not scatter photons at 422 nm and the PMT counts only the background level at $R_D = 300$ s^{-1}. Hence the ion state can be inferred from the measured fluorescence

rate on the PMT. After state manipulation with the 674 nm laser, the count rate is measured in a detection time bin of duration t_d (see figure 3.1). Assuming a Poissonian distribution of the count rate, a state detection threshold is calculated [85] so that the probability of mistaking a shelved ion for one that is cycling on the cooling transition is equal to mistaking an ion that is cycling on the cooling transition for one that has been shelved in the $D_{5/2}$ state. With $t_d = 1.5$ ms, the probability of incorrectly determining the state of the ion due to counting statistics only is less than 1×10^{-6}.

4.3 Minimising micromotion

Even when cooled to the motional ground state, a trapped ion experiences a driven motion at the RF trapping frequency Ω_{RF} due to the finite extent of the ion's motion about the RF null. Stray potentials on the trap electrodes, vacuum windows etc. produce d.c. electric fields that displace the ion from the RF null, resulting in a significant increase in the amplitude of this motion. This is known as excess micromotion, and causes extra sidebands at $\pm\ \Omega_{RF} = \pm$ 8.2 MHz to be imposed on the motional spectra in addition to those due to the secular motion in the pseudopotential. Excess micromotion also reduces the coupling strength of the probe laser with the carrier and secular sideband transitions. Therefore the excess micromotion must be reduced as much as possible before coherent spectroscopy experiments are conducted. Practically, this is achieved by applying voltages on the compensation electrodes (see figure 3.2) to produce fields that cancel out those due to stray charges, thus returning the ion to the RF null.

Three methods of increasing sensitivity are used to reduce the micromotion. Firstly, the compensation voltages are adjusted so that the position of the ion, as observed on the CCD camera, is minimally sensitive to changes in the amplitude of the RF driving field. Secondly the RF-correlation technique [110] is used to achieve fine compensation of the micromotion as follows. When the 422 nm laser is detuned by - $\Gamma_{eff}/2$ from the cooling transition, the fluorescence signal from an ion subject to micromotion is modulated at Ω_{RF} due to the Doppler effect, with an amplitude that increases with the severity of micromotion. As this signal is of

too high a frequency to be observed in real time, a time-to-amplitude converter measures the time delay between a photon detection on the PMT and the next zero crossing of the RF drive field and converts the recorded value to a digitized amplitude. By plotting a histogram of these amplitudes over many measurements, a signal is produced that effectively demonstrates the fluorescence modulation over a cycle of the RF drive frequency. When the micromotion is reduced in one cooling beam with the RF-correlation technique, there is still a possibility that the micromotion has simply been projected into a plane normal to the $\hat{k}$-vector of the beam. Therefore to minimise micromotion in 3 dimensions, the amplitude of the RF-correlation signal is reduced iteratively between all three Doppler cooling beams. The third and most sensitive method of detecting excess micromotion is to measure the coupling strength of the 674 nm probe laser with the micromotion sidebands in a frequency scan over the quadrupole transition (see section 4.5). By making small adjustments to the compensation electrode voltages, this coupling strength is reduced towards zero after repeated scans. However, as there is only one 674 nm beam, it is again possible that this method projects small amounts of excess micromotion into the plane that is normal to the beam $\hat{k}$-vector.

With reference to figure 3.2(a) (page 36), the micromotion was compensated in the microtrap as follows. The ion is trapped in the middle segment, where electrodes dc 2 and co 2 on the front side act as compensation electrodes. On the left of the middle segment, the endcap (ec) and dc 3 are connected to form one endcap on both sides of the chip. Similarly on the right the ec electrode and dc 4 are connected on both sides to form the other endcap. All other electrodes are grounded. To achieve full compensation, the micromotion amplitude was minimised in Doppler cooling beams 1 and 2 and the RF-correlation signal due to residual micromotion in beam 3 was recorded for several positions of the ion along the trap axis, as shown in figure 4.1(a). Sinusoidal fits to each RF-correlation trace were used to measure the signal contrast, which is plotted in figure 4.1(b) as a function of the ion displacement from the centre of the central segment. A linear fit describes the data well, suggesting a linear gradient in the electric field along the trap axis, relating to a harmonic potential. Therefore the RF null is a single point, attributable to the finite length of the RF electrode. This is in contrast to an ideal linear Paul trap where the RF electrode is of infinite length

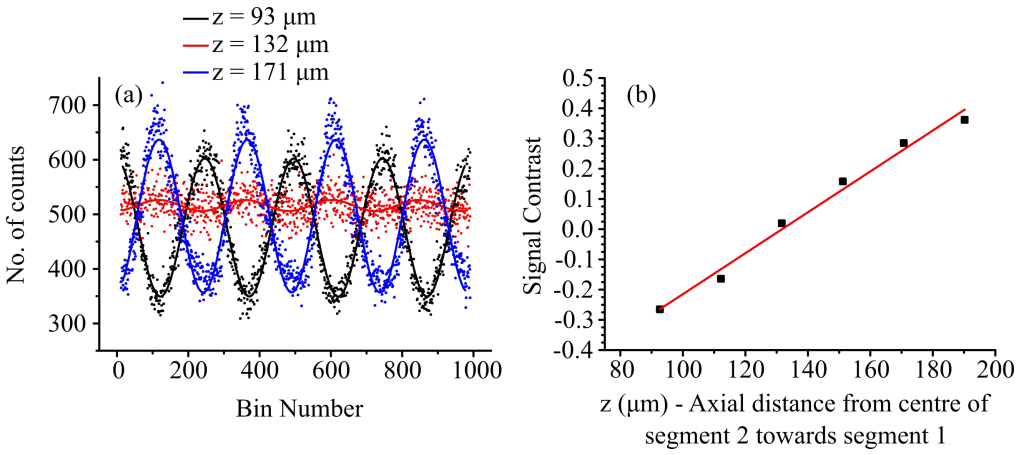

Figure 4.1: (a) RF-correlation signals from cooling beam 3 for three positions of the ion along the trap axis. Each measurement is the result of 15 s of integration time, and the converted amplitudes are in 1024 bins. In each case the micromotion was fully minimised in cooling beams 1 and 2. A sinusoid is fitted to each trace to measure the signal contrast. (b) Measured signal contrast (black) as a function of z, the axial distance from the centre of segment 2 towards the centre of segment 1 (see figure 3.2(a), page 36). A linear fit (red) yields the ion position for minimum residual micromotion.

and the RF null extends along the trap axis. After positioning the ion at the RF null, as determined by the fit of figure 4.1(b), the micromotion can be minimised in all three beams simultaneously. After being fully compensated, no further adjustment of the compensation voltages is required for at least several hours. However on the timescale of several days, significant changes to the compensation voltages may be required in order to maintain the minimisation of the excess micromotion.

4.4 Minimising magnetic field

In order to implement precise control of the Zeeman splitting of the quadrupole transition, the ambient field due to the earth's magnetic field, ion pumps etc. must first be nulled. The $D_{3/2}$ - $P_{1/2}$ repumper transition is split into six Zeeman components; two π components with $\Delta m_j = 0$ and four σ components with $\Delta m_j = \pm 1$. When viewing transversely to the magnetic field, the π and σ

components are plane polarised orthogonally to each other. Therefore all six Zeeman components can be driven by rotating the linear polarisation of the 1092 nm repumper beam. However in the special case where the repumper polarisation is parallel to the magnetic field direction, only the π transitions are driven ($\Delta m_j = 0$) and the ion is optically pumped into the $D_{3/2}(m_j = -3/2)$ state. When the magnetic field strength at the ion is reduced to zero, the quantisation axis of the ion is defined by the polarisation of the repumper laser. In this case the quantisation axis of the ion is aligned with the repumper polarisation; again the selection rule $\Delta m_j = 0$ is enforced and the ion is optically pumped into the dark state, which in turn means the ion can no longer cycle on the 422 nm Doppler cooling transition.

Therefore, these selection rules allow the magnetic field at the ion to be coarsely minimised by reducing the fluorescence rate on the 422 nm transition as follows. Repumper 1 and the Doppler cooling beams are incident on the ion (see figure 3.3). By adjusting the current in orthogonal pairs of coils in $\hat{x}$, $\hat{y}$ and $\hat{z}$ the 422 nm florescence rate is minimised for vertical polarisation of repumper 1. After this step it is not known if the field is minimised or simply aligned to the polarisation of repumper 1. Therefore the process is repeated where repumper 1 is horizontally polarised. By iterating between the two polarisation settings and minimising the fluorescence rate, the Zeeman splitting is reduced to ~ 200 kHz, as measured from a scan over the 674 nm quadrupole transition. This corresponds to a field of ~ 2 μT. After this coarse minimisation, further fine adjustments to the compensation coils can be made to reduce the Zeeman splitting (as observed from further 674 nm scans) to ~ 50 kHz, corresponding to a field of ~ 0.5 μT. When working in zero magnetic field, repumper 2 is also incident on the ion from a different angle compared to repumper 1 (see table 3.1). This prevents optical pumping to the $D_{3/2}(m_j = -3/2)$ state and the full fluorescence rate is restored.

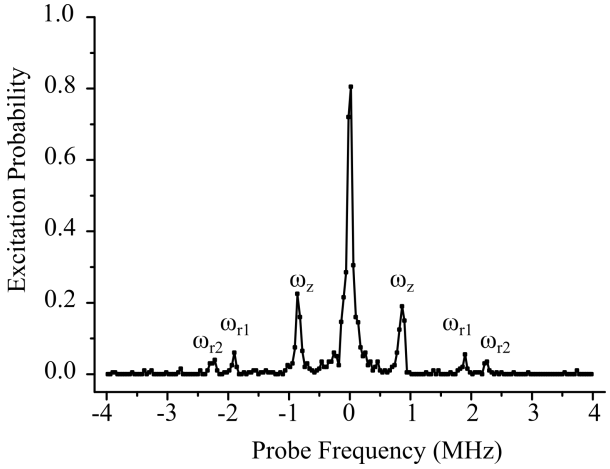

Figure 4.2: Spectrum of the quadrupole transition in zero magnetic field. 200 measurements are made at each setting of the detuning. The secular frequencies at ω_z, ω_{r1} and ω_{r2} are determined from the measurement.

4.5 Spectroscopy of the quadrupole transition

Following Doppler cooling and state preparation, the ion is coherently manipulated on the $S_{1/2}$ - $D_{5/2}$ quadrupole transition (see figure 3.1). In the simplest form this consists of a square 674 nm excitation pulse that performs a single rotation on the Bloch sphere. More complicated manipulation sequences, such as Ramsey and spin-echo spectroscopy with square and amplitude-shaped pulses, are presented in chapter 7. Rabi (single-pulse) spectroscopy is also used to determine the efficiency of the state preparation methods that follow this section.

Here Rabi spectroscopy is used to measure the resonant frequencies and associated coupling strengths of the carrier and sideband components of the quadrupole transition. In such a measurement, the 674 nm pulse frequency is varied as the intensity and duration are held constant. For each setting of the detuning, 100-200 interrogation and measurement cycles are performed to build statistics on the ion state. Figure 4.2 shows a scan over the quadrupole transition in zero magnetic field; the pulse duration and power is 10 μs and 1 mW respectively.

The secular frequencies are dictated by the pseudopotential in the microtrap. For example, in figure 4.2, the applied RF signal was 73 V peak-peak and the voltage on the endcaps, configured as described in section 4.3, was 5 V. This yields

an axial frequency of $\omega_z = 865$ kHz. The radial motion is split into two components parallel to the principal trap axes; $\omega_{r1} = 1.925$ MHz and $\omega_{r2} = 2.26$ MHz are along lines between the RF and dc electrodes respectively (see figure 3.2(b)). For the results presented in the rest of this chapter, the secular frequencies are as presented here unless otherwise stated.

4.6 State preparation

4.6.1 Polarization-resolved optical pumping

For high-fidelity quantum gates, the ion must be efficiently prepared in the ($m_j = -1/2$) sub-level of the $S_{1/2}$ ground state via optical pumping. A circularly polarised 422 nm beam with a $\hat{k}$-vector that is parallel to the applied magnetic field direction can only drive $\Delta m_j = \pm 1$ transitions in the $S_{1/2}$ - $P_{1/2}$ manifold, with the sign depending on the handedness of the circular polarisation. For σ^- light, only the $\Delta m_j = -1$ transition is driven and the ion is optically pumped into the $S_{1/2}(m_j = -1/2)$ sub-level, as demonstrated in figure 4.3(a).

Efficient optical pumping could not be achieved with 422 nm light that was prepared with a circular polarisation before the vacuum window. It was postulated that this was due to optical phase shifts induced by the birefringence of the vacuum windows and associated anti-reflection coatings [111]. To verify this, the ellipticity of the initially linearly polarised 674 nm beam was measured after passing through two vacuum windows that were subject to the mechanical stress associated with the UHV environment. The angle of incidence was 37° (the measurement could not be made on the optical pumping beam itself as it does not exit the chamber). The same experiment was conducted with two windows that were not under the mechanical stress (see figure 4.3(b)), but otherwise in the same geometry. Significantly more ellipticity was observed for the windows under mechanical stress when the incident polarisation was not aligned with the fast or slow axis of the birefringent material; clearly circularly polarised light can not pass through vacuum windows without becoming elliptical. A Berek polarisation compensator was therefore employed to compensate for the ellipticity induced by

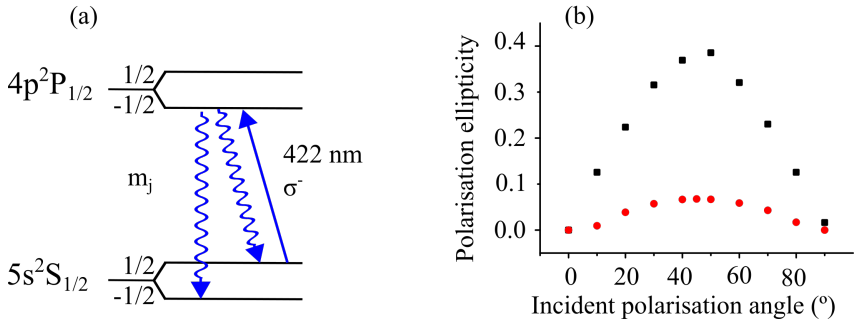

Figure 4.3: (a) The ion is excited on the $S_{1/2}(m_j = 1/2)$ - $P_{1/2}(m_j = -1/2)$ transition with σ^- polarised light, from where it spontaneously decays to either of the two Zeeman sub-levels of the ground state. After many absorptions the population is efficiently prepared in the $S_{1/2}(m_j = -1/2)$ state, as no further excitation is possible after the ion decays to that level. (b) The ellipticity of 674 nm test beam at 37 °angle of incidence after two vacuum windows with (black) and without (red) mechanical stress as a function of the initial polarisation.

the window, enabling circularly polarised light to be produced inside the vacuum chamber.

Rabi spectroscopy of two Zeeman components of the 674 nm transition in a magnetic field of $B = 290$ μT was used to determine the optical pumping efficiency; this is calculated by comparing the number of excitation events as the 674 nm laser frequency is scanned over the $(m_j = -1/2)-(m_j = -5/2)$ and $(m_j = 1/2) - (m_j = 5/2)$ Zeeman components. With the Berek compensator in place, an efficiency of 98.8 % was measured for a 20 μs pulse of σ^- polarised 422 nm light. This is limited by imperfect alignment of the beam to the magnetic field direction and the residual ellipticity of the polarisation. The requirement that the optical pumping beam is parallel to the magnetic field also places constraints on the geometry of the apparatus.

4.6.2 Frequency-resolved optical pumping

Optical pumping can also be implemented by exciting a particular Zeeman component of the 674 nm quadrupole transition in the applied bias field [25]. This frequency-resolved optical pumping (FROP) technique is inherently more efficient than the polarisation-resolved method due to the higher selectivity in exciting a particular Zeeman component. Also, with FROP, the 674 nm beam does not have to be aligned to the magnetic field direction, which can therefore be set to maximise the coupling strength to a particular Zeeman component as required. Also, pumping to either Zeeman sub-level of the $S_{1/2}$ state can be achieved simply by changing the frequency of the pumping pulse. This is in contrast to the polarisation-resolved technique where a $\lambda/4$ plate must be manually adjusted to create σ^+ or σ^- light.

The principle of the technique is as follows (see figure 4.4(a)). The 674 nm laser and the 1033 nm quench beam are simultaneously incident on the ion. After excitation on the $S_{1/2}(m_j = 1/2)$ - $D_{5/2}(m_j = -3/2)$ transition, the ion is quenched by excitation to the $P_{3/2}$ manifold and subsequent spontaneous decay to either sub-level of the $S_{1/2}$ state. However no further excitation can occur if the ion decays to the $(m_j = -1/2)$ sub-level as the 674 nm laser is far detuned from any resonant transition. Efficient optical pumping is achieved as the probability of a decay to the $S_{1/2}(m_j = -1/2)$ state approaches unity for a sufficiently long pumping duration. The 1033 nm quencher is employed so that the absorption rate on the pumping transition is not limited by the $D_{5/2}$ state lifetime.

A FROP pulse of 900 μs duration and power of 1 mW was used to prepare the ion in the $S_{1/2}(m_j = -1/2)$ state. This was detuned by 100 kHz from the unperturbed frequency of the $S_{1/2}(m_j = 1/2)$ - $D_{5/2}(m_j = -3/2)$ transition to compensate for the quencher-induced AC Stark-shift [85]. In order to measure the optical pumping efficiency, the number of excitations were compared as the 674 nm laser was scanned over the $S_{1/2}(m_j = 1/2)$ - $D_{5/2}(m_j = -3/2)$ and $S_{1/2}(m_j = -1/2)$ - $D_{5/2}(m_j = -5/2)$ transitions, as shown in figure 4.4(b). As these two transitions have different relative intensities (see figure 2.5(b), page 29), the power of the spectroscopy pulse was empirically adjusted for each scan so that the Rabi frequency was 62.5 kHz. An optical pumping efficiency of 99.8 % was

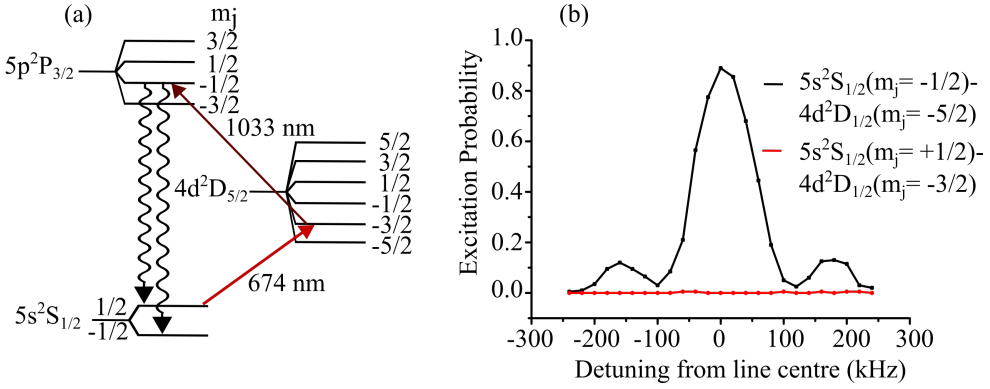

Figure 4.4: (a) The ion is excited on the $S_{1/2}(m_j = 1/2)$ - $D_{5/2}(m_j = -3/2)$ transition by the 674 nm laser and then to the $P_{3/2}$ manifold with the 1033 nm laser. From there the ion spontaneously decays to either of the Zeeman sub-levels of the $S_{1/2}$ ground state. After repeated cycles, the ion is optically pumped to the $(m_j = -1/2)$ state. (b) Rabi spectroscopy of the two Zeeman components after a 900 μs FROP pulse is used to determine an optical pumping efficiency of 99.8 %.

measured due to the FROP pulse alone. No further increase in pumping efficiency was observed when a 422 nm σ^- pulse preceded the FROP pulse. FROP is therefore a very efficient and versatile state preparation technique, although the required pumping time is significantly longer than with the polarisation resolved technique. However this could be reduced if more 674 nm laser power were available for the FROP pulses.

4.6.3 Resolved sideband cooling

The Doppler limit places a fundamental constraint on the motional state of the ion after cooling with the 422 nm laser. For example an axial frequency of 865 kHz yields a limit of $n_z \sim 11$, which is insufficient for some applications such as the Cirac-Zoller gate [112]. The well-established technique of resolved sideband cooling (RSC) [22] can be used to further cool the ion to the motional ground state ($n_z = 0$) as follows. When the ion absorbs on a red sideband of the 674 nm quadrupole transition, the vibrational number of the associated mode is reduced by 1 quanta (see figure 4.5(a)). The metastable $D_{5/2}$ state is quenched by the

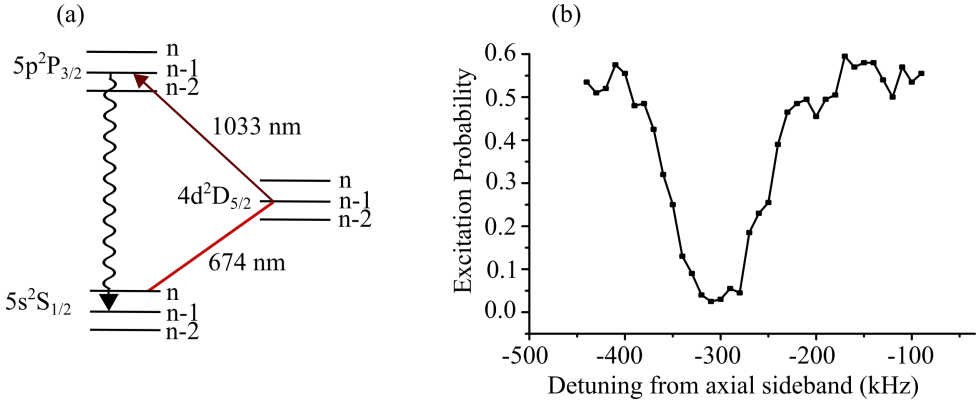

Figure 4.5: (a) Absorption on the red axial sideband of the $S_{1/2}(m_j = -1/2)$ - $D_{5/2}(m_j = -5/2)$ transition reduces the vibrational number of the mode by one quanta. As the motional state is typically preserved in the quench process, the ion is cooled after many sideband absorptions. (b) Reduction in coupling strength on the red axial sideband as the RSC pulse detuning is scanned across the Stark shifted cooling transition.

1033 nm laser via excitation to the $P_{3/2}$ state and subsequent spontaneous decay back to the ground state. As this process predominantly occurs without change in vibrational number, the ion is cooled after successive red sideband absorption and quench cycles.

Equation 2.40 (page 25) dictates that the coupling strength on the red sideband approaches zero as the motional number n is reduced. Therefore when cooling to the ground state is achieved, no further interaction with the 674 nm laser occurs and the ion remains cold. Immediately after sideband cooling, Rabi spectroscopy is used to measure the coupling strength on each sideband; a ratio of the two measured values is used to determine the mean motional state according to [12, 90]:

$$\bar{n} = \frac{1}{\left(\frac{\Omega_{n,n+1}}{\Omega_{n,n-1}}\right)^2 - 1}. \tag{4.1}$$

The following experiment was conducted to demonstrate cooling towards the motional ground state of the axial mode at ω_z. After Doppler cooling, a RSC pulse of 5 ms duration and 1 mW power is applied to the red axial sideband

of the $S_{1/2}(m_j = -1/2)$ - $D_{5/2}(m_j = -5/2)$ transition simultaneously with the quench beam at 1033 nm (see figure 3.1). The quencher induces an AC Stark shift on the $|D\rangle$ state and therefore shifts the resonant frequency of the RSC transition; 100 μW of quench light focused to a spot size of $2w_0 = 180$ μm induces a Stark shift of - 300 kHz. After the RSC pulse, a spectroscopy pulse of 1 mW power, 85 μs duration and fixed detuning is applied in resonance with the unshifted red axial sideband in the absence of the quencher in order to probe the coupling strength. When the RSC pulse frequency is scanned across the Stark shifted sideband, this coupling strength is significantly reduced, as shown in figure 4.5(b). This is a signature of a reduction in the mean motional number of the axial mode according to equation 2.40 (page 25).

In the sideband cooling experiments, the greatest observed sideband asymmetry related to a mean vibrational number of the axial mode of $\bar{n}_z = 0.3$. The main obstacle to achieving ground state cooling is the relatively low axial frequency of $\omega_z = 865$ kHz; due to the risk of electrical breakdown, the microtrap could not be operated at a higher frequency during this work. Apparent instabilities in the trap heating rate also limited progress towards true ground state cooling, and made this result difficult to reproduce reliably. However the technique presented here is expected to yield cooling to $\bar{n}_z \simeq 0$ when using a new generation microtrap, where secular frequencies of $\sim$ 2-3 MHz should be attainable.

4.7 Ion transport

The ability to deterministically transport qubits between trapping segments has been identified as a vital resource for QIP with ion traps [8], and the NPL microtrap has been designed with this criteria in mind [90]. To demonstrate basic ion transport between microtrap segments, a multichannel arbitrary waveform generator (MAWG) [113] was used to provide the electrode voltages instead of the NI PXI-6733 card. The MAWG provides 24 independent channels, each with an update rate of 25 MS/s in a range $\pm$ 9 V with 16 bit resolution.

With reference to figure 3.2(a) (page 36), the ion was transported from segment 2 to segment 1 and back to segment 2 to form a complete shuttling cycle.

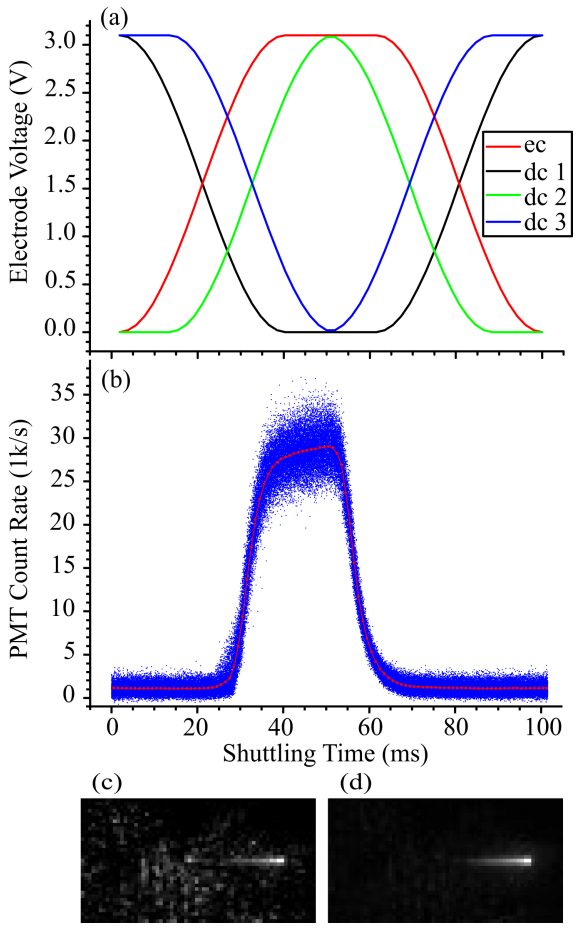

Figure 4.6: (a) The voltages applied to the trap electrodes to implement a complete shuttling cycle in 100 ms. (b) Fluorescence signal from 1000 shuttling events at a cycle frequency of 100 Hz (blue). The data is averaged into time bins of 1 ms (red). (c) CCD image of 150 ion shuttling events at 1 kHz in a 1 s continuous exposure. (d) Similarly an image of 100 shuttling events at 10 Hz over a 10 s continuous exposure.

The voltages used to achieve this, as applied to the endcap on the right of the image, dc 1, dc 2 and dc 3 are shown in figure 4.6(a). To verify successful transport, the CCD camera was set to image the ion on arrival at the focus of cooling beam 1 at the centre of segment 1. Similarly the PMT was focused to the centre of cooling beam 2 in the centre of segment 2 to monitor the return of fluorescence after a complete cycle. 1000 shuttling events were completed with no loss of the ion at a cycle frequency of 10 Hz. The fluorescence over all measurements, as monitored on the analogue output channel of the discriminator, is shown in figure 4.6(b), as well as the averaged signal in time bins of 1 ms. Exponential fits to the rise and fall times of the signal yield $\tau_{rise} = 3.86$ ms and $\tau_{fall} = 3.64$ ms, attributed to the response time of the PMT discriminator analogue output. Consequently the fluorescence signal cannot be measured faithfully with the PMT analogue output for cycle frequencies of > 100 Hz. Although the CCD camera is also limited in temporal resolution, the spatially resolved nature of the detection process enabled transport at higher shuttling frequencies to be verified by acquiring a single exposure over many cycles. For example an exposure time of 1 s was used to monitor 150 shuttles at a cycle frequency of 1 kHz; the resulting image is shown in figure 4.6(c). Similarly, figure 4.6(d) shows 100 shuttles at a cycle frequency of 10 Hz over an exposure time of 10 s. Ideally, the successful transport of single ions at shuttling frequencies up to ~ 100 kHz could be detected by counting fluorescence events from the PMT. However this was not implemented in the work presented here.

Currently, the shuttling frequency is limited by the impedance matching to the trap electrodes and the maximum voltage output of the MAWG. With improved electrical connectivity and amplification, shuttling frequencies of 1 MHz should be achievable [53, 54]. After careful calculation of the voltage waveforms that are expected to cause minimal heating of the ions, it will be possible to test the coherence of superposition and entangled states under transport.

4.8 Summary

Several experimental techniques related to high-fidelity operations with a single trapped ion have been presented in this chapter. Using the RF-correlation technique, the excess micromotion in the microtrap was fully compensated in three dimensions. A linear gradient of the electric field was found to exist along the axis of the trap due to the finite extent of the RF electrode, in contrast to an ideal linear Paul trap. The magnetic field at the ion was successfully minimised to ~ 0.5 μT by minimising the fluorescence due to optical pumping to the $D_{3/2}(m_j = -3/2)$ state with the 1092 nm laser. With the B-field minimised, simple Rabi spectroscopy enabled a measurement of the ion secular frequencies for a particular trap setting. These were in good agreement with predictions from the trap design [90]. With a bias field applied, optical pumping to the $S_{1/2}(m_j = -1/2)$ sub-level was achieved with 98.8 % efficiency using a 20 μs pulse of σ^- light at 422 nm. A higher efficiency of 99.8 % was observed using a frequency-resolved technique with the 674 nm beam, however this was at the expense of a much longer pumping pulse duration of 900 μs. Progress towards ground state cooling was also demonstrated; the lowest measured mean motional number of $\bar{n}_z = 0.3$ was limited by the low value of ω_z and the erratic trap heating rate, which made the result difficult to reproduce. However the same experimental technique should be well suited to ground state cooling with a new generation microtrap. Finally deterministic ion shuttling at frequencies up to 1 kHz has been demonstrated; higher frequencies will be achievable with imminent upgrades to the apparatus. The techniques presented here are the foundation for future high-fidelity gate operations in the microtrap architecture.

Chapter 5

674 nm Laser Agility

5.1 Introduction

In trapped-ion QIP, agile lasers are used to coherently manipulate the qubit, which may be encoded in electronic ground and metastable excited states via an optical transition [22], or in ground-state hyperfine levels via a Raman transition [114]. In both instances, state-manipulation lasers are required to deliver a sequence of optical pulses tuned to a variety of transitions (eg, carrier, red and blue motional sidebands), with an arbitrary combination of amplitude and phase. These sequences are essential for implementing quantum gates [16, 112], algorithms [51, 52] and teleportation [47, 48] with trapped ions. The same techniques have been employed in quantum metrology with trapped ions [25, 81]; the example of quantum logic spectroscopy [78] resulted in optical frequency references at record levels of precision [77]. In optical frequency standards, laser phase agility can be used to create asymmetric optical Ramsey lineshapes [24] suited to oscillator stabilisation [115]. A more generalised Ramsey scheme relying on laser pulses that are individually specified in duration, phase and frequency can significantly suppress unwanted systematic shifts in optical atomic clocks [74]. These applications require fast and accurate switching of optical parameters. For trapped-ion qubits [112], sequences of multiple pulses must be short compared to the coherence time of the atomic system. Small errors in any parameter of each pulse will reduce the fidelity of logic operations, especially when accumulated over long sequences.

This chapter documents the development and characterisation of a laser system which transfers the phase, amplitude and frequency agility, as well as fast switching capability, of direct digital synthesis (DDS) RF sources to a single laser beam. The 674 nm laser system is designed to address the $S_{1/2}$ - $D_{5/2}$ optical qubit transition in $^{88}Sr^{+}$, and is ideal for generating sequences of multiple pulses, including composite pulses [116], with high accuracy. Temporally-profiled optical pulses tailor the excitation pulse Fourier spectrum, thus minimising the power spectral density in the vicinity of off-resonant transitions, and maximising quantum gate fidelities. A second acousto-optic modulator permits the generation of a bichromatic laser field for implementing the Mølmer-Sørensen entangling gate [39, 41]; this requires frequency components that are tuned close to the red and blue motional sidebands of the qubit carrier transition, which are typically separated by a few MHz.

Agility in optical phase is demonstrated with high precision (≤ 10 mrad) and accuracy (< 0.1 %). An automated calibration procedure delivers amplitude-shaped optical pulses, with durations ranging from 500 ns to 500 ms, in good agreement with the desired functional form. A high optical extinction ratio of $> 5 \times 10^{11}$ is measured, which is defined as the ratio of the maximum optical power that can be delivered to the ion to the power of the nominally extinguished state. A sideband injection lock that transfers the frequency agility of a DDS source to the laser beam is also presented, as well as switches between single and bichromatic frequency operation on a sub-μs time scale. The contents of this chapter are based on a journal article that was published during the course of this work [117].

5.2 Agile laser experimental setup

The coherent manipulation of optical qubits requires a frequency-stabilised laser that can be switched in phase, amplitude and frequency with negligible loss of optical coherence. It is also essential to achieve a carrier transition Rabi frequency of up to ~ 500 kHz; in turn this enables sideband transition Rabi frequencies much greater than the decoherence rates usually encountered in ion traps. Typically, this requires ~ 2 mW focused to $2w_0 \approx 30$ µm [24]. Previous to this work,

a frequency-stabilised extended-cavity diode laser (ECDL, 674 nm) of limited power (4 mW) was used [24]. The laser system described here (see schematic in figure 5.1) uses optical injection locking to phase lock a 30 mW 'power laser' to a frequency-agile 'sideband slave' ECDL, permitting multiple AOM passes and fibre coupling to enable fast switching with high extinction, while still providing adequate laser power for driving the $^{88}Sr^{+}$ transition. Furthermore, the system enables agility in optical phase (ϕ), amplitude (E) and frequency (ν) without destroying the optical coherence. The principle of this injection-lock approach can be extended to ∼1 Hz laser linewidths [118], where coherence times of optical atomic transitions up to ∼1 s have been demonstrated [119].

5.2.1 Sideband slave laser

The sideband slave laser inherits the frequency stability of a stable source via a sideband injection lock [120] (see 'Sideband slave laser', figure 5.1). The master injection signal is either provided by a locally stabilised system or by an ultra-stable laser that is delivered from a neighbouring laboratory via a phase-noise cancellation system (see chapter 6). In either case, the injection signal is delivered to the sideband slave via a fibre coupler (FC4) and reverse coupling through a 30 dB optical isolator. Sidebands are imposed on the sideband slave output via weak modulation of the diode current at $f_{mod} \sim 150$ MHz, as provided by the frequency doubled output of DDS2. One of these sidebands optically locks to the injection signal, resulting in a sideband slave output that is offset from the master by $\pm f_{mod}$. Only a small injection signal (~ 20 μW) is used to avoid locking to the carrier instead of the weaker sidebands. This yields a small capture range for the sideband lock, which is only maintained for a few seconds with passive stability. Therefore an active stabilisation method is used as follows.

The frequency doubled output of DDS2 at $f_{mod} \sim 150$ MHz is divided into two paths with a power splitter. The lower path forms one input to a mixer after an RF line stretcher, and the upper path modulates the laser current. When one of the sidebands is injection locked to the master, an optical beat note at f_{mod} is measured at the avalanche photodiode (APD1), with a phase that varies through π as the sideband slave frequency is tuned through the capture range. The output

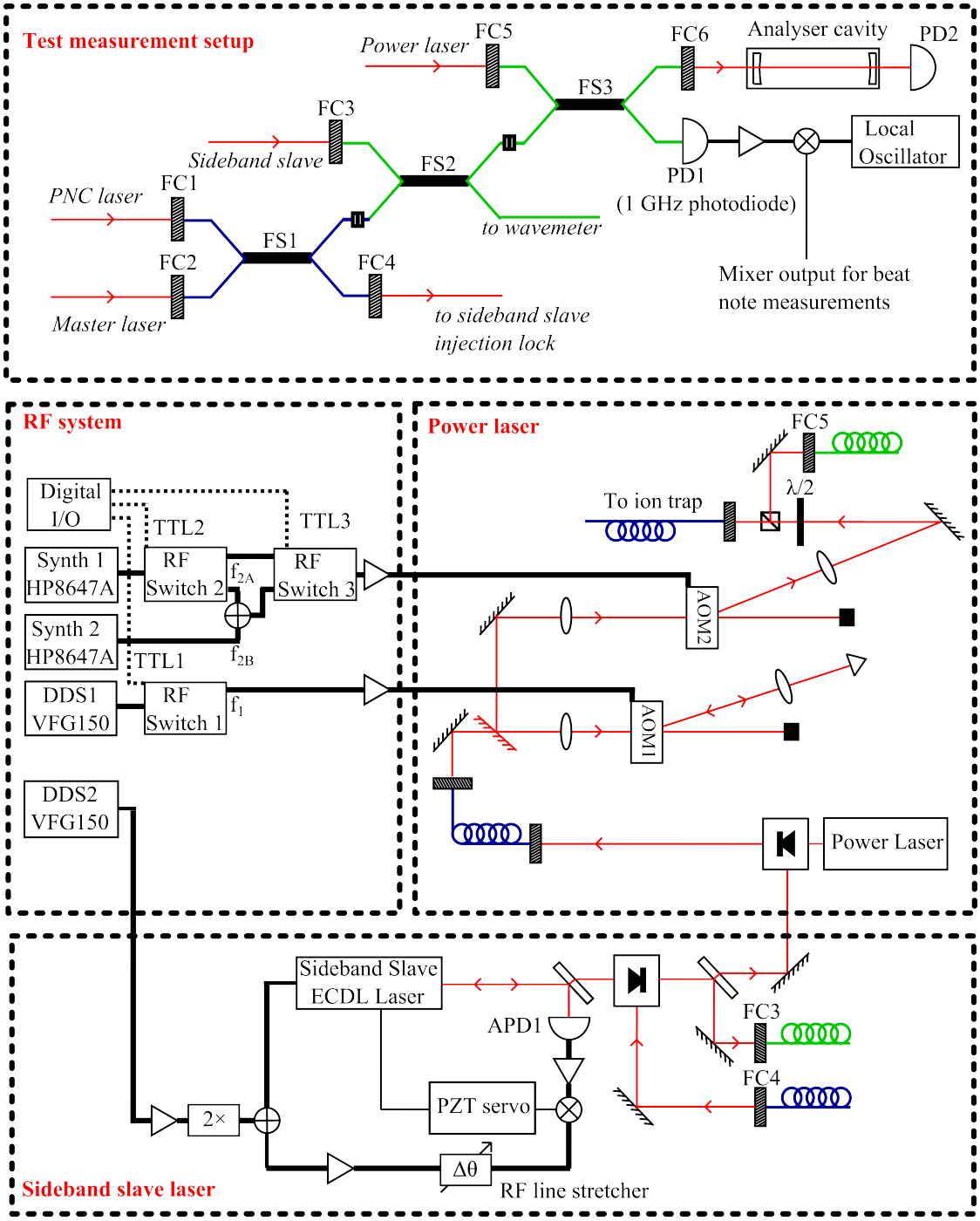

Figure 5.1: Schematic of the sideband slave laser, power laser, RF system, and test measurement setup. Each is described independently in section 5.2.

of the mixer contains a d.c. difference signal that depends on this relative phase; this is integrated to provide feedback to the sideband slave to maintain its output at the centre of the injection lock capture range. The RF line stretcher is used to precisely match the signal path lengths from the power splitter to the mixer so that the error signal is maximally insensitive to changes in f_{mod}.

With the actively stabilised sideband lock engaged, the frequency agility of DDS2 is transferred to the output of the sideband slave over a range of ± 10 MHz. Due to the nature of optical locking, the response speed is limited only by the switching speed of the DDS output itself (5 ns). Furthermore, the sideband slave output power does not depend on f_{mod} as would be the case when using an AOM to implement frequency changes.

5.2.2 Power laser

The power laser (30 mW) is injected with 1 mW of the sideband slave output via the exit port of a 40 dB optical isolator to form a second optical lock (see 'Power laser', figure 5.1). With this approach, the linewidth of the power laser is only limited by that of the master. A single-mode PM fibre cleans the mode and decouples the optical alignment between the power laser and the AOM setup. AOM1 (at frequency f_1), in double-pass configuration, provides the control of optical ϕ and E. The return pass light is vertically displaced from the incident beam, and is picked off with a compact mirror. A second modulator (AOM2) in single-pass configuration enables bichromatic operation (at frequencies f_{2A}, f_{2B}). Each AOM runs at $\sim$ 140 MHz, giving a total frequency shift of $\sim$ 420 MHz. Light is focused to $2w_0 = 100$ μm inside both AOMs to achieve a measured $1/e^2$ rise time of 30 ns, whilst maintaining a single-pass diffraction efficiency of 80 %. Varying f_{2A} changes the diffraction efficiency of AOM2 and the coupling efficiency to the second PM fibre. When compared to single-frequency operation at 140 MHz, the power out of the second PM fibre is reduced by 5 % (20 %) for a bichromatic frequency difference $\delta f_2 = (f_{2A}\text{-}f_{2B}) = 4$ MHz (8 MHz). After losses due to modulation and fibre-coupling, up to $P_1 = 2$ mW can be delivered to the ion; when focused to $2w_0 = 30$ µm, this intensity will meet the Rabi frequency criterion. The low power of the extinguished state (P_2) at the second PM fibre

output was measured using a single-photon avalanche photodiode (PerkinElmer SPCM-AQR-14-FC), resulting in an extinction ratio of $P_1/P_2 > 5 \times 10^{11}$. This high level of extinction is essential to minimise unwanted perturbation and subsequent decoherence of the qubit state between programmed excitation pulses. As an example, in a Rabi spectroscopy experiment, the interval in between state preparation and detection is typically 100 μs (see figure 3.1). If the Rabi frequency due to pulses of power P_1 is $\Omega_R = 100$ kHz, then the Rabi frequency due to the extinguished state P_2 would be such that the excitation probability after this 100 μs period would be less than 2.5×10^{-4}. This is near-compatible with the QIP fault-tolerant threshold of 10^{-4} [121, 122].

5.2.3 RF system

The agility in optical ϕ, E and ν of the system is derived from two DDS RF sources (Toptica Photonics VFG150). DDS1 is used to drive AOM1 after amplification (see 'RF system', figure 5.1), and implements phase shifting and amplitude modulation. DDS2 is used to switch the optical frequency ν via the sideband injection lock (see section 5.3.4). For each DDS, all signal parameters can be switched once every internal clock cycle of 5 ns. The RF parameters of phase θ, power P and frequency f_1, can be tuned in the ranges (with resolution): $0 \leq \theta < 2\pi$ (< 1 mrad), - 54 dBm $\leq P \leq$ - 4 dBm (16 bits), and 1 MHz $\leq f_1 \leq$ 150 MHz (< 50 mHz). The 30 ns rise time of AOM1 becomes the limiting factor in the switching speed of phase and amplitude, and the speed of frequency changes is only limited by the internal clock cycle of the DDS. The DDS output has noise components across its full frequency range. In the case of DDS1 these are largely filtered by the bandwidth of AOM1; in an optical beatnote spectrum ($\pm$ 25 MHz range), the largest noise features are at - 45 dBc (decibels relative to the carrier). A high isolation (80 dB) RF switch (Minicircuits ZASWA-2-50DR+) extinguishes f_1 from AOM1 and is controlled by signal TTL1. The phase and power output of DDS2 are kept constant.

As the agility in optical ϕ, E and ν is fully provided by the two DDS sources, analog RF synthesisers are used to drive AOM2 due to their superior noise characteristics. Synthesisers at frequencies f_{2A} and f_{2B} drive AOM2, and are coupled

into the same transmission line using a power splitter. Two high isolation RF switches, activated by control signals TTL2 and TTL3, enable three modes of operation: 1) both f_{2A} and f_{2B} are blocked, so AOM2 serves as an optical attenuator, 2) only f_{2A} drives AOM2, giving single-frequency operation, or 3) both f_{2A} and f_{2B} (with $\delta f_2 \sim 4$ MHz) drive AOM2, producing a bichromatic laser field. Using attenuators, the powers in each input line to RF switch 3 are arranged to ensure that AOM2's diffraction efficiency is identical for operation modes 2 and 3. All RF and digital I/O sources are phase locked to a 10 MHz reference.

5.2.4 Test measurement setup

Routine measurement of system properties, e.g. noise spectra, optical beatnotes and amplitude-shaped pulses, is enabled by a test setup (see 'Test measurement setup', figure 5.1) based on a network of 2×2 fibre splitters and a 1 GHz photodiode (Thorlabs-DET02AFC). The power laser and the sideband slave laser are coupled in at fibre couplers FC5 and FC3 respectively (the master signal is coupled in at inputs FC1 or FC2 , see chapter 6). The network is configured so that the master, sideband slave and power laser are all incident on a 1 GHz fast photodiode (PD1) and a Fabry-Pérot scanning cavity (the transmission is monitored by PD2). The master and sideband slave are additionally incident on a wavemeter. Under typical operating conditions, when AOM1 is supplied with the maximum DDS amplitude, the measured power (P_{meas}) of the power laser at PD1 is $P_{max} \sim 100$ μW.

Phase changes and the phase stability of amplitude shaped pulses are measured by monitoring the 420 MHz beatnote between the power laser after three AOM passes and the sideband slave. This is demodulated to the desired frequency using a local oscillator and an RF mixer. Frequency changes as implemented by the sideband injection lock are measured in a similar manner to phase shifts. The master and sideband slave light is blocked when characterising either the temporal profile of optical pulses or bichromatic operation. Amplitude-shaped pulses are measured directly at PD1; 12-bit measurement resolution was required for enhanced precision. In the case of bichromatic operation, a beatnote at $\delta f_2 = 4$ MHz is detected at the same photodiode.

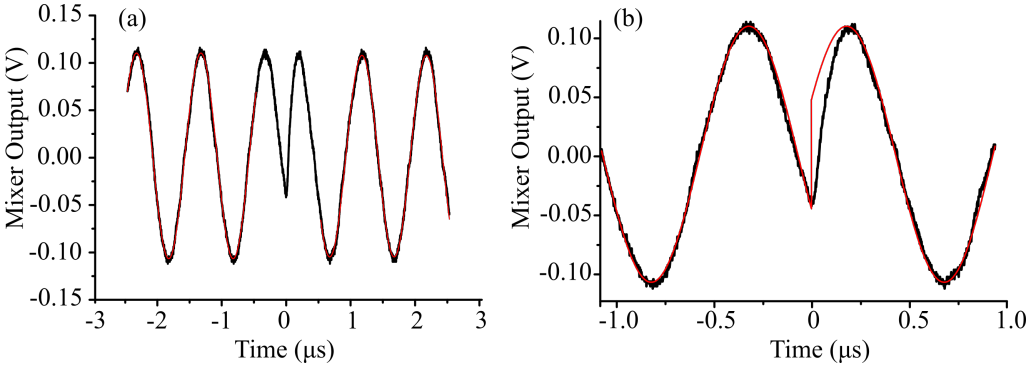

Figure 5.2: A single-shot measurement of a phase step $\delta\phi = \pi$. (a) Two fits (red) to the data (black), on either side of the phase step, are used to calculate $\delta\phi$. The central 1 μs of the trace is ignored in the fitting procedure. (b) A zoomed-in version of the same data (black) with the fit from before the phase step extended throughout (red), including $\delta\phi = \pi$ at the programmed switching time (t = 0).

5.3 System characterisation

5.3.1 Phase agility

Accurate phase control of the optical beam is essential in trapped-ion quantum information processing, where sequences of up to $\sim$ 30 coherent optical pulses, including composite pulses, are employed [48]. Similarly, spectroscopic measurements using optical Ramsey [24], and hyper-Ramsey [74] techniques also rely on accurate phase control. In these applications, any inaccuracies in implementing phase steps will accumulate over the sequence and lead to decreased coherence times.

A programmed phase shift $\delta\phi = (\phi_1 - \phi_2) = \pi$ in the 1 MHz demodulated signal, as described in section 5.2.4, is shown in figure 5.2(a). The timing of the phase step can be controlled with 5 ns resolution, and the accuracy is only limited by the 10 MHz reference stability. Sinusoidal fits to the 1 MHz signal are taken either side of the phase step using the Levenberg-Marquardt (L-M) fitting algorithm [123] to calculate the measured phase step value, using only $\delta\phi$ and amplitude as fitting parameters. The central 1 μs of the trace is ignored in the fitting procedure as the signal is non-sinusoidal in a short period after

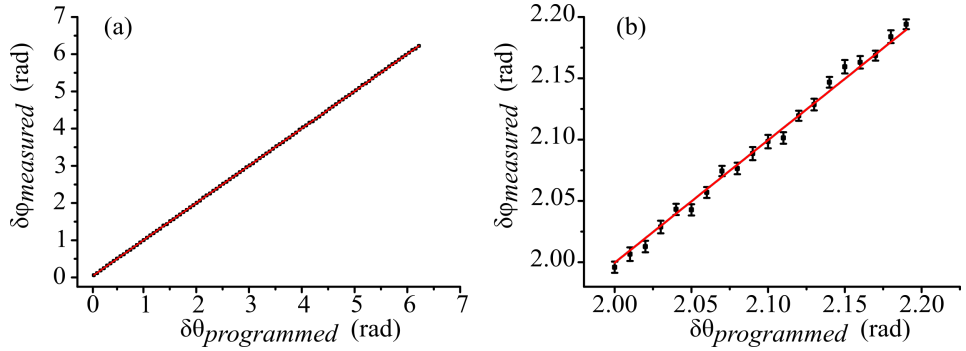

Figure 5.3: Measured phase change ($\delta\phi_{measured}$) as a function of the programmed value ($\delta\theta_{programmed}$). (a) From 0 to 2π rad in increments of $\pi/50$ rad, where each data point is the average of 25 single-shot measurements, with fitted gradient of 1.00086(2). Error bars are smaller than the data points in this plot. (b) Higher resolution measurement (10 mrad increments, 45 single-shot measurements per point) with fitted gradient of 1.000(5).

the phase shift. In figure 5.2(b), the fit to the data before the phase change is extended in duration, and shifted by π at the programmed switching time. The extended function converges to the data after $\sim$ 200 ns, which is determined by the AOM's 30 ns rise time and the non-linearity of the mixer; the latter feature was determined by an independent RF measurement.

The average of 25 single-shot phase shift measurements is plotted against the programmed value, and repeated over the range $0 \leq \theta < 2\pi$, as shown in figure 5.3(a). A linear fit yields a gradient of 1.00086(2), showing accurate phase control over the full range. Figure 5.3(b) shows a higher resolution measurement, where the average of 45 single-shot measurements per programmed value is plotted in increments of 10 mrad, and the fitted gradient is 1.000(5). In both figures the error bars are shown as the standard deviation of the mean. Amplification noise in the demodulated signal (at $\sim$ 4.5 % of the peak-to-peak signal) prevents phase steps at the limit of resolution of the DDS ($<$ 0.1 mrad) from being resolved in the measurement. This could have been improved by appropriate filtering of the beat note signal, or by increasing the amount of light coupled into the test measurement setup.

5.3.2 Amplitude calibration and agility

By controlling the temporal profile of an optical pulse's amplitude, the power spectral density remote from the carrier frequency can be greatly suppressed when compared to the case of a square pulse. The Blackman function is a favoured form due to its high side lobe suppression under a Fourier transform; other related functions perform a similar role [124]. In coherent interactions with trapped ions, this reduces unwanted off-resonant excitation of nearby transitions. When addressing a weaker motional sideband transition, minimising the interaction with the stronger off-resonant carrier is crucial to maximising coherence of the operation. Amplitude-shaped optical pulses were critical in a two qubit trapped-ion entangling gate of record fidelity [41].

To account for the non-linear response of AOM1, and enable production of optical pulses with arbitrary temporal shape, an automated calibration routine was developed. This sets the amplitude of DDS1 via USB and records the photodiode (PD1) signal with a 14-bit digitiser. Firstly, optical power is recorded at PD1 as a function of the DDS RF amplitude in order to evaluate the AOM response (see figure 5.4(a)). A polynomial fit to the data acts as a calibration function to specify the DDS amplitude for a desired optical power. A 5th order polynomial was found to produce an insufficient quality of fit to the data as seen from the significant modulation in the regular residuals in figure 5.4(b). A fit to a 9^{th} order polynomial however (figure 5.4(c)) resulted in residuals with a significantly lower modulation. To verify the 9^{th} order calibration, a linear ramp in programmed optical power (P_{prog}) from 0 to P_{max} is recorded as in figure 5.5(a). Figure 5.5(b) shows the same data and fit on a logarithmic scale. After the calibration, the optical power at the ion can be set arbitrarily relative to the maximum power available (2 mW). To set an absolute power at the ion, the ratio of powers at PD1 and before the ion trap window must be measured at the maximum amplitude setting of DDS1. The calibration procedure's duration is < 5 s, enabling small alignment drifts to be accounted for intermittently.

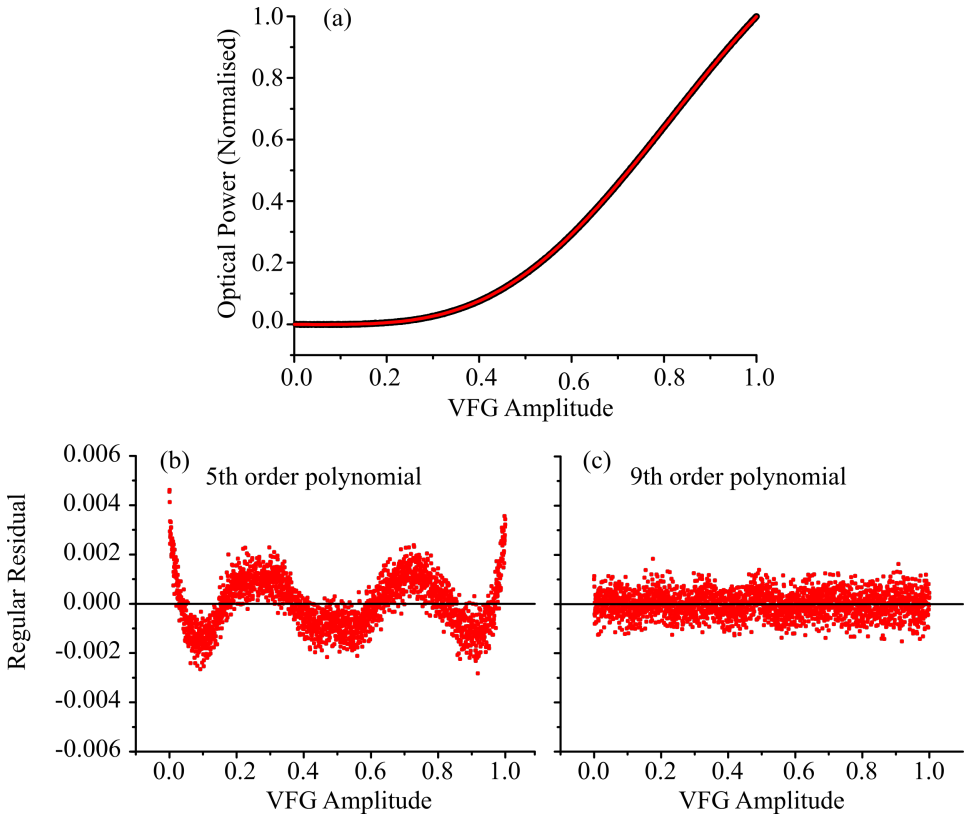

Figure 5.4: (a) The measured (normalised) power (black) as a function of the VFG amplitude setting. A 9$^{\text{th}}$ order polynomial fit (red) is also shown. (b) and (c) show the regular residuals for 5$^{\text{th}}$ and 9$^{\text{th}}$ order polynomial fits respectively.

The calibrated system produces amplitude-shaped pulses with high accuracy. A Blackman pulse of duration $2T$ and amplitude E_0 has a profile of the form [124]:

$$E(t) = \begin{cases} E_0[0.42 - 0.5\cos(\pi t/T) + 0.08\cos(2\pi t/T)] & \text{for } 0 \geq t \geq 2T \\ 0 & \text{elsewhere.} \end{cases} \quad (5.1)$$

To create an optical pulse with electric field amplitude $E(t)$, the system is programmed to generate a pulse of the form $E^2(t)$ in power. The data in figure 5.6(a) shows a measurement of a Blackman pulse of 500 μs duration, fitted to $E^2(t)$ with the L-M algorithm, using only E_0 as a free parameter. Figure 5.6(b)

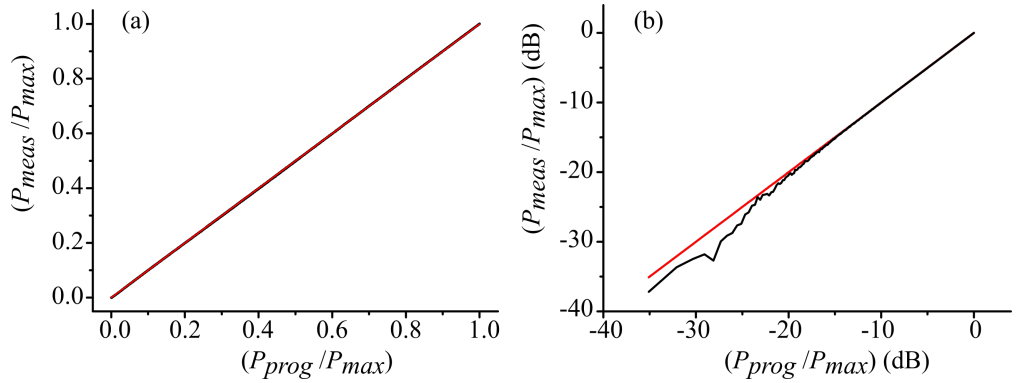

Figure 5.5: Calibrated optical response. Fibre output (P_{meas}) as a function of the programmed optical power (P_{prog}), shown on a (a) linear-linear and (b) log-log scale. The linear fit (red) to the data (black) yields a gradient of 0.99938(2). Deviation from linear behaviour is only significant at powers at least 20 dB below the peak power.

shows the same data on a logarithmic scale; the deviation from the ideal form near the noise floor of the measurement is clear. This is expected from the deviation of the fit and data at low optical powers in figure 5.5(b). Due to this deviation, Blackman pulses with a peak power >10 dB lower than that shown in figure 5.6 are expected to deviate significantly from the desired functional form.

The coefficient of determination (COD) indicates quantitatively how much of the deviation in the data about the mean is attributable to the fitted model [125], with COD = 1 indicating a perfect fit of all data points. The fit of figure 5.6 gives COD > 0.99995, demonstrating a close agreement between the data and the ideal $E^2(t)$ form. Blackman pulses can be produced accurately over six orders of magnitude in duration, as shown in figures 5.7(a-d), where each fit to $E^2(t)$ has a COD > 0.99992. The excellent match of a pulses measured shape to the programmed form is limited by AOM1 at very short times by the AOM rise time, and at durations of a few seconds by alignment drift due to thermal effects.

A more stringent test of calibration procedure accuracy is to calculate the discrete Fourier transform (DFT) of the measured pulse shape. A programmed Blackman pulse of duration $2T$ = 500 µs, as shown in figure 5.6, was measured over 200 single shots and averaged to reduce measurement noise. The resulting

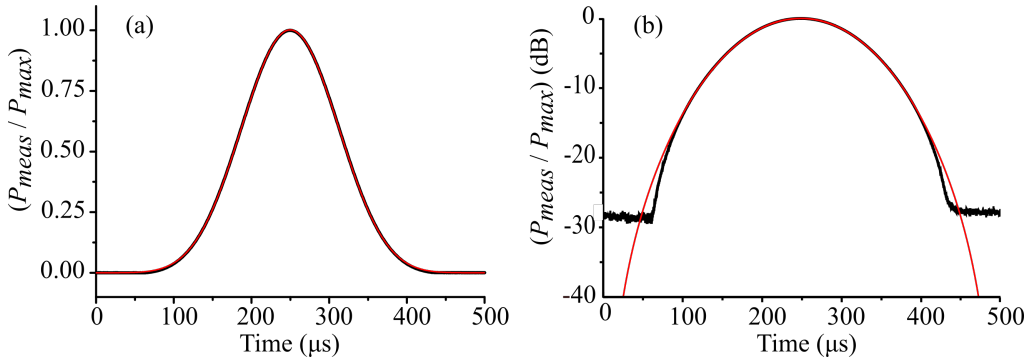

Figure 5.6: Data (black, average of 200 single-shot measurements) and fit (red) of a measured Blackman pulse of duration $2T = 500$ μs. The data points are recorded at intervals of 0.224 μs and the fit is of the form $E^2(t)$ (see equation 5.1). The optical power recorded from the test fibre output (P_{meas}) is scaled to the maximum power available ($P_{max} = 100$ μW). The data and fits are plotted with the measured power axis on a (a) linear, and (b) logarithmic scale. The latter shows the fit deviates from the data at low powers and settles completely at the noise floor of the measurement.

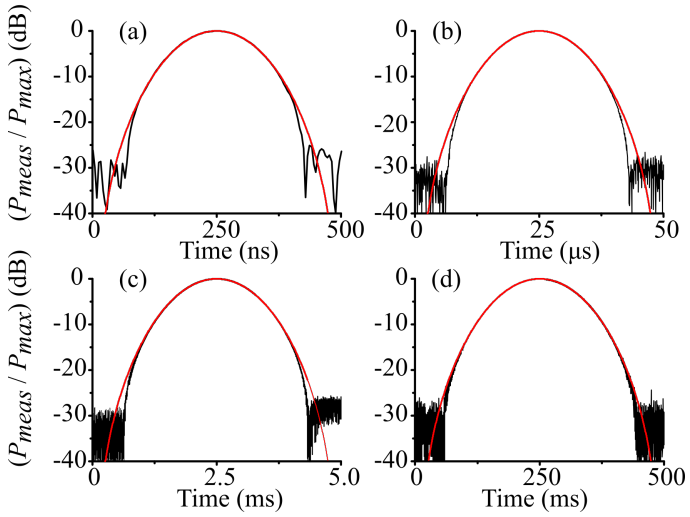

Figure 5.7: Accurate Blackman pulse shapes are produced with durations varying over six orders of magnitude: (a) 500 ns, (b) 50 μs, (c) 5 ms and (d) 500 ms. The COD fitting parameter is > 0.99992 for each. To record (a), it was necessary to increase the optical power to $P_{max} = 1$ mW.

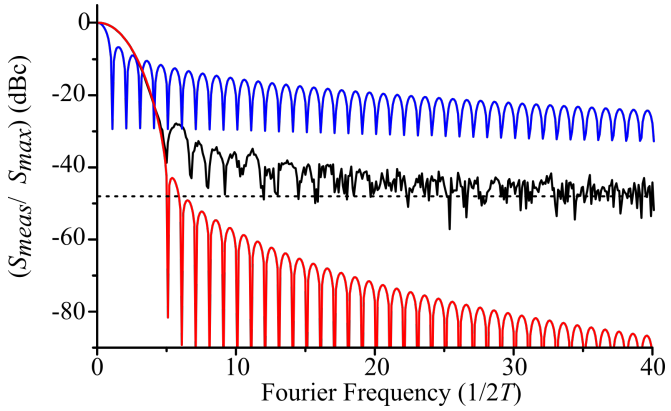

Figure 5.8: The power spectral density distribution of measured optical pulse shapes as determined by a discrete Fourier transform (DFT). A Blackman pulse of duration $2T = 500$ μs (black) is compared to a square pulse (blue) of the same duration and the same integrated optical power. The measured power spectral density (S_{meas}) is quantified with respect to the carrier maximum (S_{max}). The Blackman pulse exhibits a substantial reduction in S_{meas}/S_{max} at the higher Fourier frequencies as expected; quantifying this reduction is limited by the measurement noise floor (independently determined to be 48 dBc, as shown by the dashed line). The DFT of the fit to the Blackman pulse in figure 5.6 is also presented (red) and shows a close match to the DFT of measured pulse above the measurement noise floor. For each DFT, the sample interval was 16 ns and the sample length was 312,505.

data was processed by the DFT algorithm, as shown in Fig. 5.8. For comparison, the DFT was calculated for a measured square pulse of the same duration and integrated power, as well as for the simulated function $E^2(t)$ with $2T = 500$ μs. In the range where the Fourier frequency is greater than $25/2T = 50$ kHz, the power spectral density of the Blackman pulse is ~ 27 dB below that of the square pulse. This difference demonstrates the advantage of using amplitude-shaped pulses for coherent excitation experiments. The discrepancy between data and theory for the Blackman pulse (beyond $5/2T = 10$ kHz) is due to the residual non-linearity of the calibrated system and the noise floor of the averaged data, measured at 48 dBc. The effect of this reduction when resonantly driving a π-pulse on a blue motional sideband was considered. The sideband's parent carrier, detuned by the ions motional frequency, is the closest strong transition which can be driven

off-resonantly. By setting the duration of a Blackman pulse so that $1/2T < 0.1$ of this detuning, the power spectral density resonant with the carrier is close to the measurement noise floor. Taking this as an upper limit, a 2 % reduction in the fidelity of the operation is estimated. If the spectral density was at 60 dBc, as expected from the DFT of an ideal Blackman pulse, this infidelity would reduce to 0.2 %.

5.3.3 Phase stability during amplitude shaping

Any phase instabilities during an interrogation pulse lead to the same decoherence effects as described in section 5.3.1. It is therefore essential to verify that the amplitude-shaping process does not induce unwanted phase shifts during a pulse. Measuring the temporal profile of a laser pulse directly at a photodiode does not yield any information about the optical phase. However, phase shifts can be monitored during a pulse by demodulating the beat note between the AOM-shifted power laser and the sideband slave as detailed in section 5.2.4. The resulting waveform is described by the demodulated beat frequency f_{beat} under a Blackman envelope $E(t)$:

$$V(t) = E(t)\sin(2\pi f_{beat}t). \tag{5.2}$$

The measured waveform with $f_{beat} = 5$ kHz was fitted to $V(t)$ with the L-M algorithm with only E_0 as a free parameter, as shown in figure 5.9. The fit yields a COD = 0.977, which is dominated by imperfect fit of the envelope to $E(t)$. This is due to the non-linearity of the mixer output with input power, and is particularly noticeable and the start and end of the pulse. However the carrier is well described by $\sin(2\pi f_{beat}t)$, demonstrating there is not a significant optical phase shift during the amplitude-shaped pulse. The absolute phase of the carrier signal changes from shot-to-shot when measuring beat note signals due to low-frequency (< 100 Hz) phase-noise caused by mechanical vibrations of mirror mounts, air currents etc. However for coherent control it is only necessary for the relative phase to be stable during a single interrogation sequence (see chapter 7).

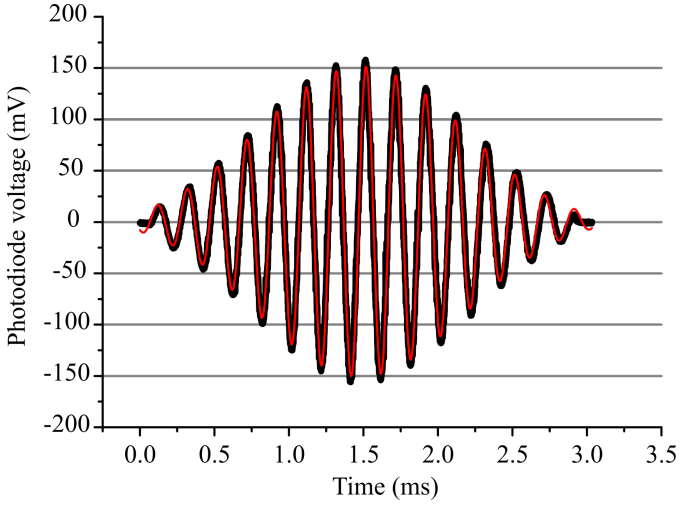

Figure 5.9: The 5 kHz beat signal (black) forms the carrier under a Blackman envelope. A fit (red) with equation 5.2 demonstrates the phase is maintained throughout the duration of the amplitude-shaped pulse.

5.3.4 Frequency agility

For coherent control of trapped ions, extensive pulse sequences may address different transitions consecutively, necessitating frequency switching on a timescale much less than the gate operation time. The system developed here enables arbitrary sequences of single-frequency or bichromatic pulses; the latter feature is required for the Mølmer-Sørensen entangling gate operation [39, 41].

Frequency shifts are precisely implemented by changing the modulation frequency f_{mod} of the sideband injection lock as described in section 5.2.1. A sub-μs frequency switch of magnitude 2 MHz, as typically required for bridging between the sideband and carrier transitions in sideband cooling, is shown in figure 5.10. Here the 420 MHz beat note between the AOM shifted power laser and the sideband slave is initially demodulated to 2 MHz. At t = 1.75 μs the output of DDS2 is increased by 2 MHz, resulting in a shift of the demodulated beat frequency to 4 MHz. Sinusoidal fits (red) to the data (black) either side of the frequency switch, with the only the amplitude as a free parameter and $f_{BEATA} = 2$ MHz, $f_{BEATB} = 4$ MHz show that the programmed step is accurately implemented.

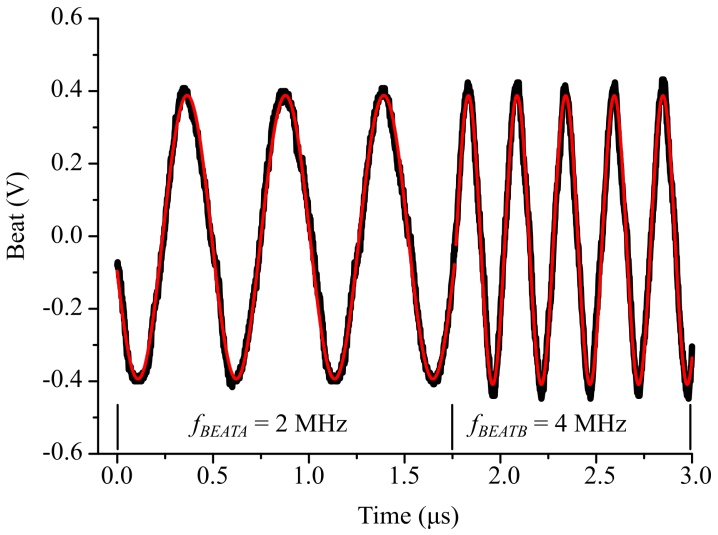

Figure 5.10: A frequency switch of 2 MHz is implemented at t = 1.75 μs. The data (black) and fit (red) of the demodulated beat signal is shown with f_{BEATA} = 2 MHz and f_{BEATB} = 4 MHz before and after the frequency switch respectively.

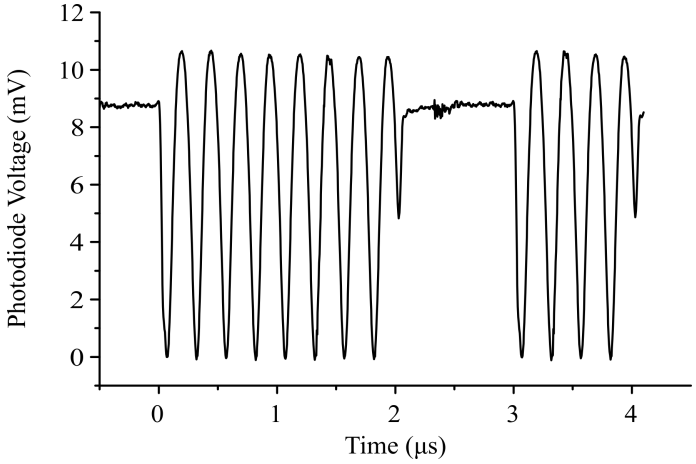

Figure 5.11: Switching between single-frequency and bichromatic modes of operation. A 4 MHz beat signal is observed when the system is in bichromatic mode. The displayed data is the average of 39 single-shot measurements. The noise features (at 1.4, 2.4 and 3.4 μs) are due to pick up of the TTL control signal in the measurement process.

In bichromatic mode, AOM2 is driven with $f_{2A} = 138$ MHz and $f_{2B} = 142$ MHz so that the optical beam carries two frequencies, separated by approximately twice the axial trapping frequency of the ion [41] ($\sim$ 4 MHz in typical experiments [22, 97]) as required in the Mølmer-Sørensen scheme [41]. In single-frequency mode only f_{2A} drives AOM2. To demonstrate fast switching between modes, changes between bichromatic and single-frequency operation are measured. In bichromatic mode, a 4 MHz beatnote is detected at the photodiode (see figure 5.1), whereas in single-frequency mode only a d.c. voltage is detected. Figure 5.11 shows an example sequence, with 2 μs of a 4 MHz beat, followed by 1 μs of single-frequency operation, followed by 1 μs of the 4 MHz beat. Control signals TTL2 and TTL3 are derived from a digital I/O source that shares the same 10 MHz reference as all RF sources, enabling precise control of the number of beat periods in a bichromatic pulse.

5.4 Summary

The construction and characterisation a 674 nm laser system that is fully agile in phase, amplitude and frequency for the purpose of coherent optical interactions with trapped $^{88}Sr^{+}$ ions has been described in this chapter. Measurements demonstrate that the agility of a DDS RF source is transferred to the optical beam via an AOM with high precision and accuracy. The phase of the optical beam can be switched in $\sim$ 30 ns with a measurable resolution of 10 mrad and accuracy better than 0.1 %. An automated procedure calibrates the non-linear response of the RF and AOM system, which enables amplitude-shaped pulses of arbitrary shape and duration to be produced. In turn, this facilitates tailoring of the Fourier transform of an optical pulse; comparing the DFT of measured Blackman and square pulses demonstrates the significant reduction of spectral density at Fourier frequencies remote from the carrier in the former. Blackman pulses with durations ranging over six orders of magnitude from 500 ns to 500 ms, in good agreement with the desired functional form, have been demonstrated. Furthermore the amplitude modulation of the pulses did not produce any extra optical phase shifts. The optical system is configured to implement frequency switches via a sideband injection lock and switch between single-frequency and

bichromatic operation on sub-microsecond timescales. These combined abilities are ideal for implementing the Mølmer-Sørensen entangling gate operation in $^{88}Sr^{+}$. Additionally, switching of optical pulses is achieved with a high extinction ratio of 5×10^{11}, which is an essential feature for maintaining atomic coherence in the absence of light during pulse sequences. In respect of trapped ions, the techniques presented are highly relevant to applications in quantum information processing and precision quantum metrology. Some of these require accurate and high resolution phase control, such as recent proposals for generating Dicke and N00N states in trapped ions [126], as well as for high-fidelity local addressing of trapped atoms/ions by composite sequences of laser pulses [127]. Beyond ions, the general principles are also relevant to neutral atom systems used in quantum information with cavity QED [128], and atom interferometry for precision inertial sensing [129, 130, 131].

Chapter 6

674 nm Laser Stability

6.1 Introduction

Highly stable lasers are required in several fields of research, including gravitational wave detection [132], frequency metrology [66] and quantum information processing (QIP) [83]. Gravitational wave detectors employ sophisticated schemes for the continuous stabilisation of laser power [133, 134] and beam pointing [135]. These, along with the ultra-stable oscillators used in optical frequency standards [136], represent the state of the art for continuous wave (cw) systems. In contrast, cw lasers are externally modulated to form pulses as required for qubit preparation [22, 25, 27] and gate operations [22, 114, 137] in trapped-ion QIP, and for precision spectroscopy of single-ion [69] and neutral-atom based [138] optical frequency standards.

In QIP and quantum metrology, the pulse power and beam pointing determine the optical intensity sampled by the atoms, and thus effect the coupling strength of the atom-laser interaction. Variations in this coupling strength reduce the repeatability of the interactions over a sequence of measurements under otherwise identical conditions, thus degrading the fidelity of quantum logic operations and the precision of spectroscopic measurements. QIP applications employ sequences of short pulses (1 μs $\leq T \leq$ 100 μs), with varying durations [47, 48], temporal shapes [41, 117] and peak powers. Certain quantum-enhanced metrology schemes require short pulses for entangled state preparation, followed by long, low power

pulses (1 μs $\leq T \leq$ 100 μs, $P <$ 10 nW) for spectroscopic measurements. This motivates agile lasers with stability over a large dynamic range in peak power and duration.

The purpose of this chapter is to present an amplitude-modulated laser with long-term power [133, 134], beam pointing [139, 140, 141, 142] and frequency stability [133, 136]. Firstly, a general overview of the experimental setup for the stabilisation schemes is described. The characterisation of the system begins with an assessment of the frequency stability of the local stable laser and the phase-noise cancelled ultra-stable laser. A feedback loop that is designed to stabilise the power of optical pulses over a range of 10^5 is then described, followed by a detailed assessment of the achieved levels of stability over this range. This is followed by a description of a feedback loop that is used stabilise the position of the beam at the ion over long periods. By changing the setpoint of this feedback loop, the excitation probability of a single ion is measured as the beam is raster scanned across the ion, from which the beam radii at the ion are deduced. A measurement of the long term stability of the pulse power and beam position concludes the chapter, along with calculations of the expected impact of the results on the infidelity of single qubit gate. The work presented in this chapter was conducted in close collaboration with Ben Yuen, who made significant contributions to the pulse power and beam position stabilisation systems. Furthermore, Guido Wilpers was partly responsible for the installation and characterisation of the phase-noise cancellation setup.

6.2 Stable laser experimental setup

In chapter 5, an agile laser that produces accurately shaped pulses that each have a precisely defined phase, peak power and frequency [117] was demonstrated. In this section, a description is given of the apparatus that enhances the capabilities of this system to include stabilisation of the pulses in frequency, power, and beam pointing. An overall diagram showing all aspects of the stable laser system is shown in figure 6.1. Detailed flow diagrams of the feedback loops used to stabilise the power and beam position are given later in sections 6.3.2 and 6.3.3 respectively.

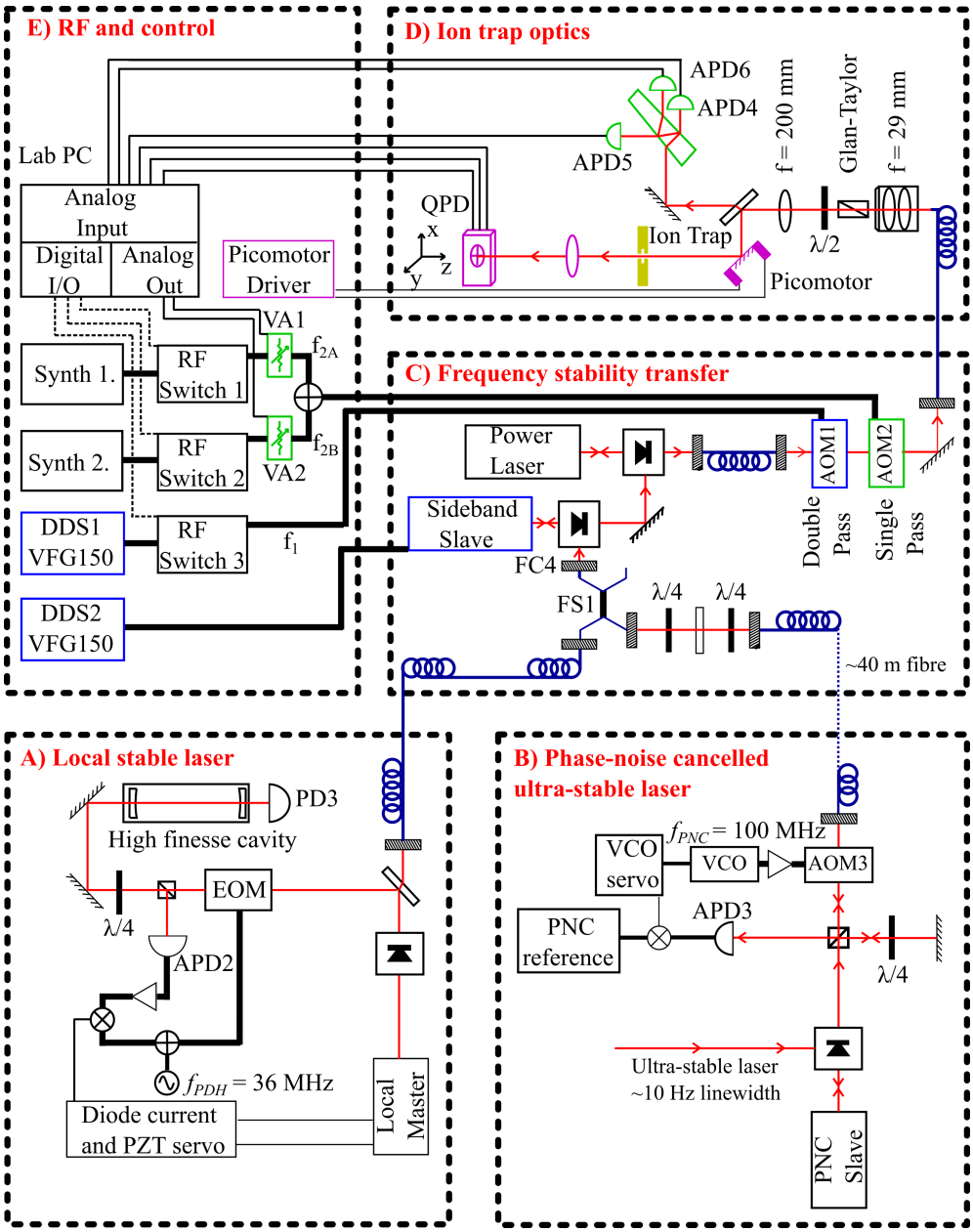

Figure 6.1: Schematic of the apparatus used to stabilise the frequency, pulse power and beam pointing of an amplitude-modulated 674 nm laser. Components highlighted in blue are configured to generate the agile pulse sequences. Similarly green indicates apparatus used to stabilise the pulse powers, and purple denotes the beam pointing stabilisation equipment.

6.2.1 Local stable laser

A stable laser of modest linewidth ($\sim$ 2 kHz) is realised with an ECDL laser that is locked to a medium finesse ($F \sim 2000$) cavity (see A, figure 6.1). ULE glass and optical contacting of the mirror substrates to the cavity spacer ensures the lowest possible temperature sensitivity. The cavity is situated in a vacuum chamber that is evacuated to $1{\times}10^{-6}$ mbar and temperature stabilised to $\pm$ 10 μK to yield a drift rate of 100 Hz/s.

The Pound-Drever-Hall technique [143] is used to lock the ECDL to the stable cavity. Here a electro-optic modulator (EOM) imposes sidebands at $f_{PDH} = 36$ MHz on the beam before it is incident on the medium finesse cavity. The optical beatnote between the reflected carrier and sidebands has a phase that varies as the centre frequency is scanned across the cavity resonance. This is detected at APD2 and demodulated to form a d.c. error signal, enabling feedback to the ECDL current and grating angle. The locked laser linewidth is therefore reduced from its free running value.

6.2.2 Phase-noise cancelled ultra-stable laser

For maximum frequency stability, an injection lock to an ultra-stable laser ($\sim$ 9 Hz linewdith [144]) is used (see B, figure 6.1). The ultra-stable source also utilises a Pound-Drever-Hall lock, however the stable cavity has a much higher finesse ($F \sim 200000$) and a lower drift rate ($\sim$ 2 Hz/s). The stable injection signal is delivered via 40 m of PM fibre from a neighbouring laboratory. The acoustic vibrations induced in the fibre add significant phase noise to the signal, typically broadening the laser linewidth from $\sim$ 10 Hz to $\sim$ 1 kHz. Therefore a phase-noise cancellation (PNC) system is employed to effectively eliminate optical path length variations along the 40 m fibre.

Only a small amount of ultra-stable light (100 μW) is available for this experiment (the source is primarily used for a $^{88}Sr^{+}$ ion frequency standard in a separate laboratory). Therefore a free running 'PNC slave' laser at 674 nm is injection locked to the ultra-stable source. This yields sufficient optical power (5 mW) for the PNC system and injection locking of the sideband slave laser (see section 5.2.1). The phase-noise cancellation method used is similar to that

of the original proposal [145]. The PNC slave output is separated into two paths with a polarising beam splitter. The first beam is frequency-shifted by AOM3 ($f_{PNC} \approx 100$ MHz) and is coupled into the 40 m fibre. The beam is retro-reflected at the fibre output to form a 80 m total optical path length. After a second modulation by AOM3, the beam is incident on APD3. The second beam is incident on APD3 without any modulation or fibre coupling. A beat-note at $2 \times f_{PNC}$ is therefore detected at APD3, with a phase that varies directly with the optical path length variations of the fibre. The 200 MHz beat is demodulated to d.c. with a reference oscillator to form a discriminant. This is integrated to provide feedback to the modulation input of the VCO that drives AOM3; this implements small shifts in f_{PNC} that effectively compensate the phase-noise induced in the fibre.

6.2.3 Stability transfer

The stability of the local stable laser or the PNC ultra-stable laser is transferred to the sideband slave and power lasers by the beam delivered by FC4 as described in chapter 5 (see C, figure 6.1). The use of FS1 enables either stable source to be selected easily without any optical realignment. The second output of FS1 provides a signal for the test measurement setup as described in section 5.2.4.

6.2.4 Ion trap optics

Light is delivered to the ion via a PM fibre, the output of which is collimated with a multi-element achromatic lens of $f = 29$ mm (see D, figure 6.1). A second achromatic lens ($f = 200$ mm) focuses the beam to a radius $2w_0 \sim 50$ μm at the ion. A Glan-Taylor polariser and a half-wave plate produce a pure, rotatable polarisation. A portion (~ 5 %) of the beam is used for monitoring the pulse powers; two reflections from a wedged optic, and the transmitted beam, are measured with independent avalanche photodiodes. Where the optical power incident on APD4 is P_0, APD5 and APD6 measure $\sim P_0/20$, and $\sim P_0/20^2$ respectively. With this cascaded arrangement of APDs, a signal-to-noise ratio of > 100 is guaranteed over a range of 10^5 in optical power. The system is calibrated

so that voltage readings on each APD can be converted directly to a power at the ion P_i, and all optical powers are given as such throughout this chapter.

The beam that is incident on the vacuum system window is at an angle 37° from normal incidence. After exiting via the second window, the beam is then incident on a quadrant photodiode (QPD) (Thorlabs PDQ80A). The beam at the centre of the ion trap is imaged onto the QPD with a magnification of ~ 10 with a $f = 100$ mm lens, and the QPD signals are used to infer the position of the beam focus in the plane of the ion. The beam pointing is altered via a piezo-actuated mirror (New Focus Picomotor 8885, angular resolution 1.5 μrad). When combined with a translation stage that sets the axial position of the focusing lens; this enables precise positioning of the beam waist inside the vacuum chamber. The beam position is set in a repeatable manner with the QPD as a spatial reference, thus circumventing the significant hysteresis of the Picomotor. As the light is delivered to the ion trap via single-mode fibre, contributions to the QPD signals from instabilities in the transverse mode of the beam are assumed to be negligible.

6.2.5 RF and control

To achieve the desired stability, the RF and control setup was modified slightly from that described in section 5.2.3 (see E, figure 6.1). Variable attenuators (VAs) were added to enable active stabilisation of the pulse powers. In single frequency mode, only VA1 is used. In bichromatic mode, VA1 and VA2 are adjusted independently to equalise the optical powers of each frequency component. Any of f_1, f_{2A}, f_{2B} can be blocked with high extinction (80 dB) with the RF switches.

Two channels of an analogue output card (NI PXI-6733) control the attenuation of VA1 and VA2, which act as actuators in the power stabilisation feedback loop. The attenuation level that stabilises the pulse powers is calculated from samples of APD4, APD5 and APD6; these are acquired at a rate of 500 kHz (during the optical pulses only) by an analogue input card (NI PXI-6254) and are averaged over each pulse to give a single value for the pulse power. Furthermore, sum and difference signals of the QPD are used to derive a discriminant for the beam pointing stabilisation system.

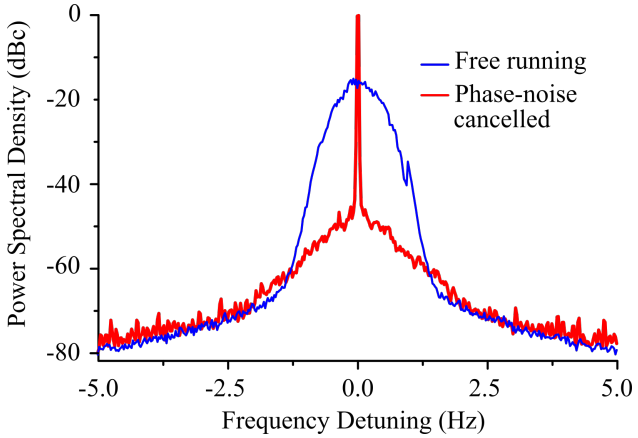

Figure 6.2: An optical beat note between the PNC slave and the output of the 40 m fibre has a FWHM linewidth of $\leq$ 10 mHz with the phase-noise cancellation loop engaged (red) after 10000 s of averaging time. Also shown is the beat spectrum with no active feedback (blue).

6.3 Results

6.3.1 Frequency stability

Experiments utilising optical qubits require a highly stable laser to manipulate the internal state of the trapped atoms. In QIP, high frequency stability permits multiple rotation pulses to be implemented within the system coherence time. Similarly optical atomic clocks benefit from the narrow Fourier-limited linewidths achieved ($\sim$ 1 Hz) when interrogating the sample with a highly stable source [119].

Optical beat notes are used to verify that the frequency stability of the ultra-stable source [144] is faithfully transferred to the injection signal for the sideband slave laser. For the measurement, the output of the 40 m fibre was placed locally to the input. This enabled a beat note between the injection locked PNC slave and the output of the 40 m fibre (see figure 6.1) to be measured on an out-of-loop APD. The resulting beat note spectrum is shown in figure 6.2; The FWHM $\leq$ 10 mHz linewidth of the locked beat signal, measured over 10000 s of averaging time, is significantly less than the demonstrated linewidth of the ultra-stable source (FWHM = 9 Hz, [144]), hence the signal is transferred across the 40 m

fibre with negligible loss of stability. Also shown is the significant line broadening that occurs when no feedback is employed.

A further optical beat note measurement between the phase-noise cancelled ultra-stable source and the local master enables an estimate of the linewidth of the latter. This is because frequency fluctuations of the ultra-stable laser contribute negligible broadening of the beat note signal compared to the local master. The measured FWHM of 1.9 kHz is in agreement with a previously measured upper limit of (2.4 kHz), inferred from interrogations of a single $^{88}Sr^{+}$ ion [24].

6.3.2 Pulse power stability

The power stabilisation system is designed to eliminate variations in the power of the agile pulse sequences up to Fourier frequencies of $\sim$ 100 Hz, as these are expected to be the major limitation to achieving robust high-fidelity gates. Figure 6.3 shows a schematic of the feedback loop that is used to stabilise the power of the interrogation pulses. The loop is initialised by the user defining a pulse sequence, which for example may include long duration (5 ms) sideband cooling pulses and short spectroscopy pulses (20 μs) of varying powers. This sequence is communicated to DDS1 (see E, figure 6.1), and is executed so that the entire sequence is repeated at a 100 Hz cycle frequency. The data acquisition of the APD voltages is synchronised with the output of DDS1 via a TTL trigger signal so that data is recorded during the optical pulses only. The pulse with the greatest signal-to-noise ratio on any of the three APDs (see D, figure 6.1) is selected for active stabilisation. If the voltage measured on the chosen APD due to this pulse is V_1, then feedback is generated by comparing a running time average $< V_1 >$ over a specified number of pulses N and comparing this value to a user defined setpoint V_0. The feedback is applied to a variable attenuator (VA1) that provides fine control of the RF power that is supplied to AOM2, thereby stabilising the power of the beam at the ion. In order to prevent measurement noise from limiting the stability of the system, the APD signals are electronically filtered before the analogue input card. Passive RC filters were found to have insufficiently steep roll-off, so active 4th order Bessel filters, with a 3 dB cut-off frequency of $f_0 = 200$ kHz, were constructed for each APD channel.

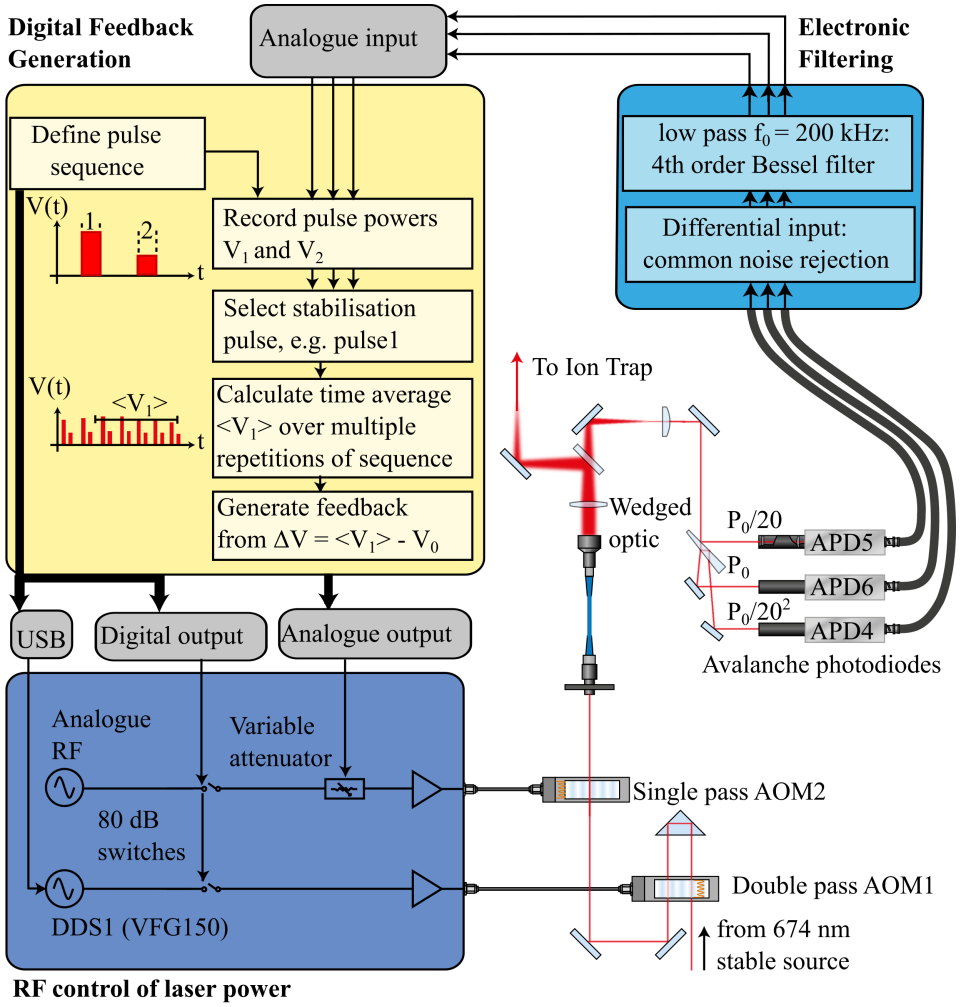

Figure 6.3: Graphical representation of the feedback loop that is used to stabilise power of interrogation pulses. The use of 3 cascaded APDs enables a dynamic range of 10^5. The context of this system with respect to the wider apparatus is clarified in figure 6.2.

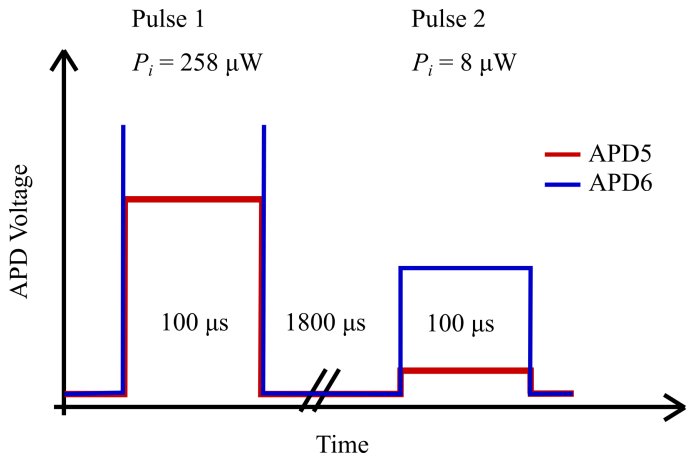

Figure 6.4: Schematic of the pulse sequence that is used to test the stabilisation system. Pulse 1 is selected for active stabilisation from measurements of APD5, whilst APD6 is saturated. However during pulse 2, APD6 has a greater signal-to-noise ratio then APD5, and is chosen to measure the stability of this pulse relative to the first.

The power stabilisation system is demonstrated using the optical pulse sequence shown in figure 6.4, which is repeated at 100 Hz, as is the typical cycle frequency of experiments when interrogating a trapped ion. Measurements of pulse 1 on APD5, of $P_i = 258$ μW and 100 μs duration, are used to generate feedback to the variable attenuator as explained above. The number of integration pulses was set to $N = 2$ and an equal weighting was given to each pulse. Pulse 2 is initially set to $P_i = 8$ μW and is of the same duration as pulse 1. No active feedback is applied to pulse 2, however the common power scaling of the system transfers some of the stability from pulse 1.

The power of pulse 1 is such that it saturates APD6. This effect was found to be a major limitation of the stabilisation system, as the APD output voltage was heavily distorted after a saturating pulse. The signal was found to recover to a steady state value with a double exponential decay, with time constants 85 μs and 9 ms, with the exponential decay amplitudes depending on the power of the saturating pulse. For the pulse sequence in figure 6.4, pulse 1 saturates APD6 so that the amplitude of the second exponential is negligible, therefore in this case the measurement of the second pulse is not affected. However care must be

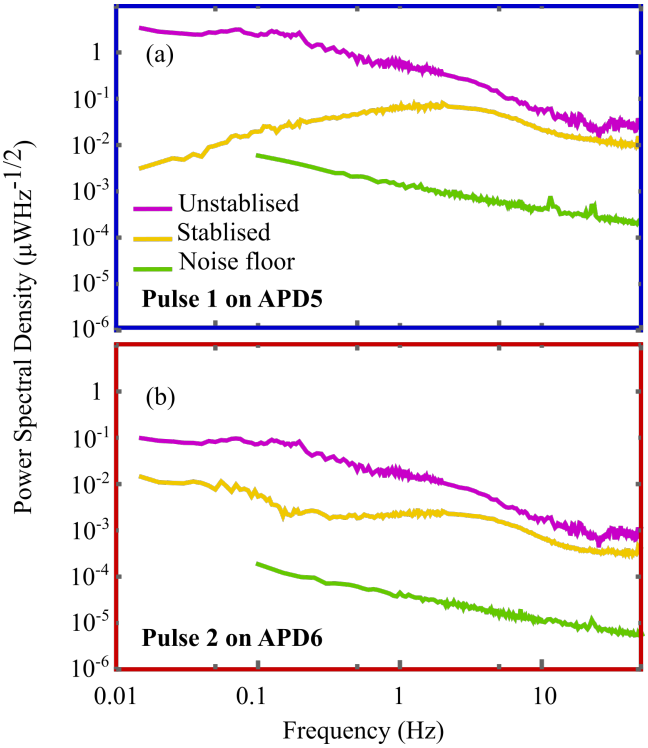

Figure 6.5: (a) Power spectral density of pulse 1 as measured on APD5 with (amber) and without (purple) active feedback. Also shown is the measurement noise floor (green). The pulses were monitored at a rate of 100 Hz over a period of 1 hour, resulting in 10000 measurements. (b) Power spectral density of pulse 2 as measured on APD6, again with (amber) and without (purple) active feedback. The measurement noise floor of APD6 is also shown (green).

taken so that, in a given pulse sequence, saturation effects do not compromise the measurement. APD saturation could be avoided by using an optical chopper to ensure only pulses that do not cause saturation are incident on each APD for a given sequence. However, these are not desirable in the vicinity of the ion trap apparatus due to induced vibrations etc. Electro-optic amplitude modulators, such as a Pockels cells combined with crossed polarisers, could be used as alternatives. However this would be at the cost of significant extra complexity, and would present an extra possible source of drift.

The short term effectiveness of the power stabilisation system was assessed as follows. The power of pulse 1, as measured on APD5, was recorded over 100 s.

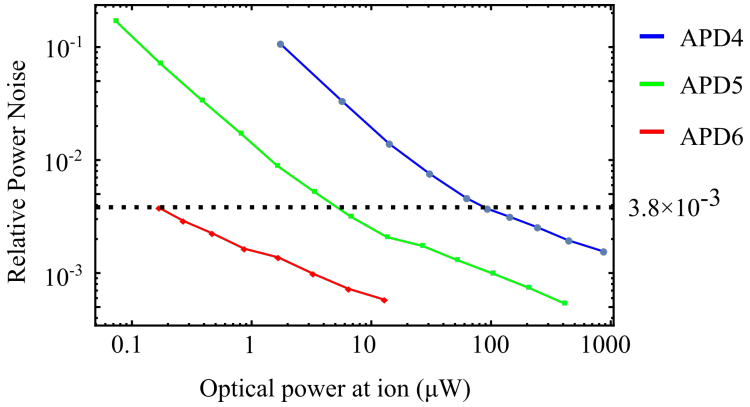

Figure 6.6: Relative power noise over 100 s for pulses of 100 μs duration. A value of $< 3.8 \times 10^{-3}$ is measured over a range of 10^4 in optical power.

Given that the cycle frequency of the experiment is 100 Hz, this corresponds to measurements of 10000 individual pulses. This measurement was carried out with and without active feedback being applied to pulse 1. The corresponding power spectral density (PSD) plots are shown in figure 6.5(a). Also shown is the corresponding PSD when there is no optical input to APD5, effectively demonstrating the noise floor of the measurement. There is a $\sim$ 1000 fold reduction in the PSD at 0.02 Hz when feedback to pulse 1 is engaged compared to the unstabilised case. As expected from the Nyquist theorem, the difference between the two cases reduces as the Fourier frequency approaches the sampling frequency of 100 Hz. Figure 6.5(b) shows data from the same experiment, and shows the PSD of pulse 2 as measured on APD6. As is clear from the figure, the gain in stability is only partially transferred to pulse 2 when active feedback is applied to pulse 1; only a ten-fold improvement in the PSD at a frequency of 0.02 Hz is observed. The most likely source of this limitation is small drifts in the efficiency of AOM2 as a function of applied RF power over the course of the measurement. This could be circumvented by applying independent feedback loops to each pulse, which would be a matter of increased software complexity only.

A further test was carried out in order to investigate the dynamic range of the system. For a sequence of only one pulse of 100 μs duration, the pulse power was again recorded over 100 seconds at a repetition frequency of 100 Hz. The relative

power noise, defined as the standard deviation of all 10000 pulses over the mean value, was measured as the setpoint of the feedback loop was varied from 100 nW to 900 μW. For each setpoint, feedback was generated from measurements of the APD with the greatest signal-to-noise ratio. Figure 6.6 indicates that the relative standard deviation is $< 3.8 \times 10^{-3}$ for a range of almost 10^4 in optical power at the ion. It is reasonable to expect that APD4 would offer similar stability levels up to 20 mW if sufficient laser power were available. Here a measurement time of 100 s was chosen as this is the typical time taken to acquire a single spectrum, such as that shown in figure 4.2. Measurements of the long-term stability of the system, as required for quantum gates with repeatable high fidelity over several hours, are presented in section 6.4.

6.3.3 Beam pointing stability

Experiments involving the trapping of single ions and neutral atoms typically use Gaussian laser beams for state preparation and manipulation. These are often focused to a small beam radius ($w_0 \sim 15$ μm) in order to increase the optical intensity sampled by the atoms, therefore maximising the atom-laser coupling strength. However with decreasing beam radius, this interaction strength becomes increasingly sensitive to variations in the beam pointing. Laser beams focused inside a vacuum chamber are also subject to sources of optical aberration, such as spherical aberration from focusing lenses or astigmatism due to optical windows. Consequently there can be considerable uncertainty as to the true beam radius in the vicinity of the trapped atom(s). To solve these experimental challenges, a system was developed that stabilises the position of the laser focus inside a compact ultra-high vacuum system [101] to an adjustable set-point. This enables automatic alignment of the beam to a position that maximises the atom-laser interaction strength, and measurements of the beam radii using a single trapped ion as a probe. In a linear string of ions, the alignment procedure could be used to determine the beam positions that maximise the coupling to each ion.

The beam position in the plane of the QPD is measured by comparing the optical powers incident on each quadrant (see Fig.6.7). The difference signals z_{diff}

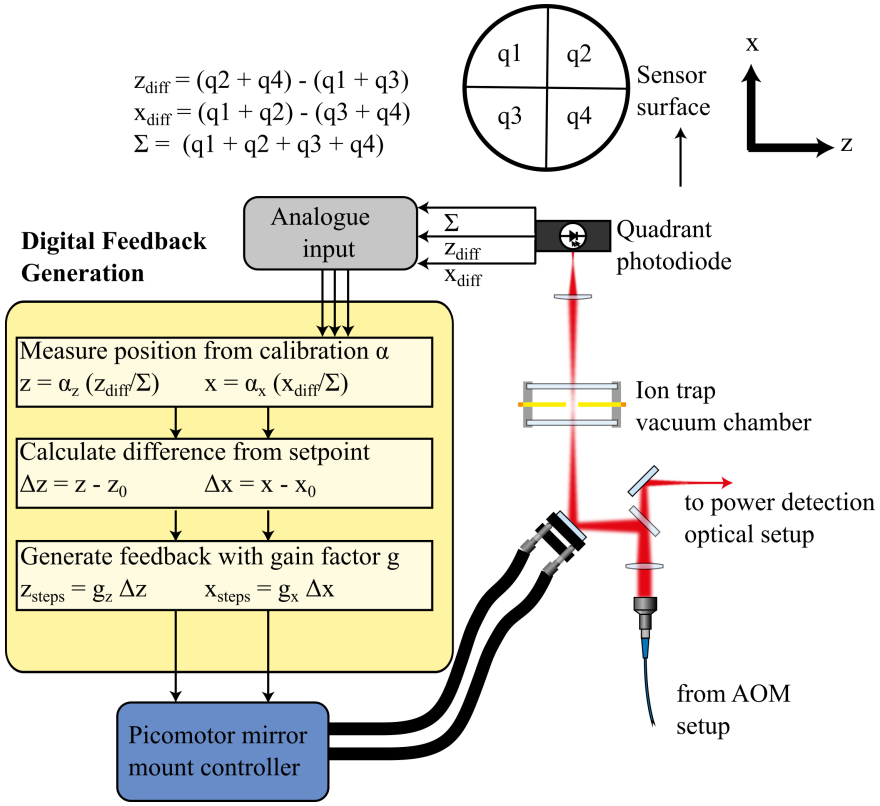

Figure 6.7: Graphical representation of the feedback loop that is used to stabilise the relative position of the beam focus in the plane of the trapped ion. The context of this system with respect to the wider apparatus is clarified in figure 6.2.

and x_{diff} are made independent of the laser intensity by dividing by a sum signal Σ that measures the power incident on all four quadrants. Through an external calibration, factors α_x and α_y are calculated which convert the QPD signals into a measurement of the relative beam position in the plane of the ion in z and x. To stabilise the beam position, the two normalised difference signals are subtracted from user-defined set points z_0 and x_0 to form an error signal. Proportional feedback to the Picomotor reduces this error signal to zero within the limits of the angular resolution of the actuator. To demonstrate the stabilisation method, the beam position on the QPD was monitored over two measurement runs of 22 hours, once with no feedback and once with the stabilisation engaged (see Fig. 6.8). With active feedback, the RMS deviation of the calibrated beam position

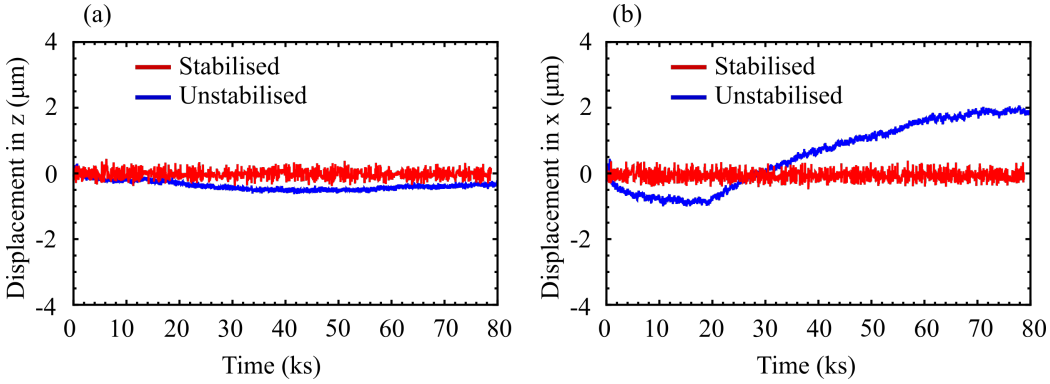

Figure 6.8: Measurement of the relative beam position at the ion in z (a) and x (b) with (red) and without (blue) active feedback. The RMS deviation of the stabilised signal is $\sim$ 150 nm in z and x.

at the ion was $\sim$ 150 nm in both z and x. The implications for the infidelity of a simple quantum gate due to beam position variations at this level are discussed in section 6.4.

Single pulse (Rabi) spectroscopy was used to measure the excitation probability of a single $^{88}Sr^{+}$ ion as a function of beam position, as set using the feedback loop as described above. After Doppler cooling and optical pumping, an excitation pulse of duration $2T = 3$ μs, resonant with the $S_{1/2}(m_j = -1/2)$ - $D_{5/2}(m_j = -5/2)$ transition at 674 nm, probes the atom-laser interaction strength. The resulting state is determined by measuring fluorescence rate on the $S_{1/2}$ - $P_{1/2}$ transition (further details of the spectroscopy sequence are given in chapter 4). By repeating the interrogation sequence 200 times for each setting of the beam position, the excitation probability is measured as the beam is raster scanned across the ion, as shown in figure 6.9. A fit to the data that accounts for the Gaussian intensity profile of the laser beam and the evolution of the internal state due to a resonant excitation pulse is also shown. The transverse intensity profile of a 2-dimensional Gaussian beam is given by:

$$\beta(z,x) = \exp\left\{ -2\left(\frac{z-z_0}{w_z}\right)^2 - 2\left(\frac{x-x_0}{w_x}\right)^2 \right\}, \tag{6.1}$$

where w_z, w_x and z_0, x_0 are the beam radii and the offsets from an arbitrary

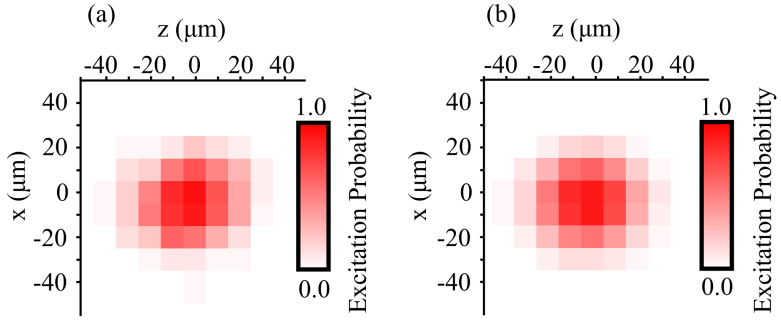

Figure 6.9: (a) Measurement of the excitation probability of the ion at 674 nm as a function of the beam position. The excitation pulse was 3 μs in duration and tuned to the $S_{1/2}(m_j = -1/2)$ - $D_{5/2}(m_j = -5/2)$ transition in $^{88}Sr^+$. (b) The fit to the results. The inferred beam radii at the ion are $w_z = 27(3)\,\mu$m and $w_x = 24(3)\,\mu$m.

centre point in the z and x directions respectively. The excitation probability p_e of a single ion after a resonant driving pulse of duration $2T$ is given by the Rabi formula:

$$p_e(\Omega_R, T) = \sin^2(\Omega_R T), \tag{6.2}$$

where Ω_R is the Rabi frequency on resonance. This is related to the laser intensity as $\Omega_R \propto \sqrt{\beta}$, and so varies as the beam is scanned across the ion. Equations 6.1 and 6.2 combine to give a final expression for the excitation probability:

$$p_e(z, x, T) = \sin^2(\sqrt{\beta(z, x)}T). \tag{6.3}$$

The raster scan shown here was acquired prior to the long-term stabilisation data shown in figure 6.8, and a different method was used to calibrate the position of the beam at the ion at this time. This was done by comparing the QPD signals when the beam was maximally aligned to the ion in two locations of a well known separation, as verified by imaging the ion with a CCD camera of known pixel size (see section 3.3.8); here the magnification of this imaging system was the dominant source of error in the calibration. A 2-dimensional fit to the data shown in figure 6.9(a) with equation 6.3 yields fitted beam radii of $w_z = 27(3)\,\mu$m

and $w_x = 24(3)\,\mu$m (the ellipticity is expected due to the astigmatism caused by the non-normal incidence of the beam on the vacuum window, see section 6.2.4). To verify this result, an out of vacuum measurement of the beam was made with an identical optical setup, except a CCD beam profiler was placed in the position of the ion. The measured beam radii of $w_z = 25.8\,\mu$m, $w_x = 24.1\,\mu$m agree with the in-vacuum measurements within their associated errors. Therefore the raster scan is an accurate method of measuring the beam radii in an ultra-high vacuum chamber, as well as a convenient method of automatically aligning the beam to the ion.

6.4 Effects of stabilisation on long term gate fidelity

A long term goal of this experiment is to implement robust gate operations with a fault-tolerant fidelity. It is therefore instructive to estimate the levels of infidelity that can be expected when implementing simple qubit rotations with the stable laser. It is first necessary to evaluate the long-term stability of both the pulse power and beam position over the course of many hours. The two-sample Allan deviation [146] is used to graphically illustrate this long-term stability. For the beam position measurements, this is simply plotted for $r = \sqrt{z^2 + x^2}$ using the data shown as a time series in figure 6.8. However a separate experiment was performed to evaluate the long term power stability. In order to achieve the best long-term stability, it was necessary to reduce the APD gain by a factor of 15 compared to the results shown previously in this chapter. This significantly reduces the operating range of the system, however the full range could be recovered if a laser source of sufficiently high power were available. In the experiment presented here, a greater proportion of the available signal out of the second PM fibre was diverted to the cascaded APD setup to compensate for this gain reduction. Therefore the maximum power available at the ion was reduced to $P_i = 18\ \mu$W. To test the long-term power stability, active stabilisation was applied to a single pulse of $P_i = 18\ \mu$W and 100 μs duration at a cycle frequency of 100 Hz, and the average power of pulses over 1 second was recorded over a

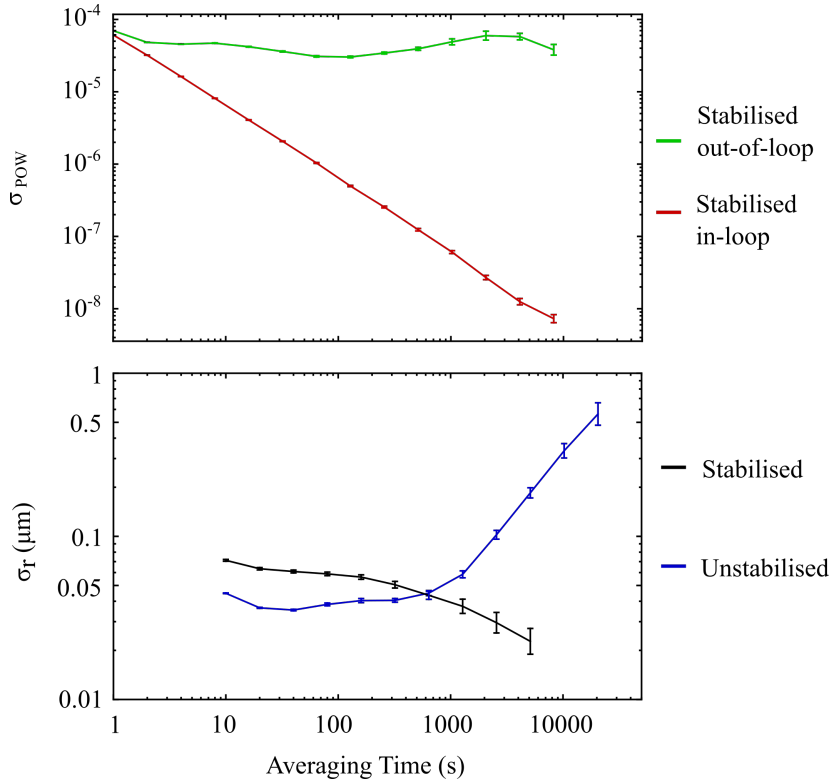

Figure 6.10: (a) Allan deviation of pulses of $P_i = 18$ μW average power for in-loop (red-APD5) and out-of-loop (green-APD6 attenuated) measurements, given as the fractional deviation in absolute power at the ion. (b) Similarly the Allan deviation of the beam position at the ion with (black) and without (blue) active feedback, as generated from measurements of the QPD.

period of 43 hours. For the purposes of this test, the optical input to APD6 was attenuated so that its voltage output during the pulse was the same as APD5. This served as an out-of-loop measurement.

Figure 6.10(a) shows the fractional Allan deviation for the pulse power σ_{POW} for both the out-of-loop (APD6) and in-loop (APD5) measurements for averaging times ranging from 1 to 8000 seconds. There is a significant difference between the in-loop and out-of-loop measurements, however a separate measurement showed this is mainly due to the relative drift of the inherent dark-current of the APDs. Similarly figure 6.10(b) shows the Allan deviation of the measured position of the beam at the ion σ_r with and without active stabilisation. As is expected from

the data plotted in figure 6.8, active feedback slightly increases the measured deviation for short averaging times (this effect could potentially be eliminated by further optimisation of the feedback gain). However for times greater than 1000 s there is clear benefit to engaging the feedback loop, with a standard deviation of < 30 nm for averaging times greater than 5000 s.

From the Allan deviation data for the pulse power and beam position, the corresponding contributions to the standard deviation in the expectation value σ_{EP} after a simple qubit rotation can be calculated. A hypothetical $\pi/2$ rotation is considered for a pulse of 18 μW power with a Gaussian beam waist $w_0 = 22.5$ μm that is initially perfectly centred on the ion at $r_0 = 0$ μm. Under these ideal conditions, the excitation probability after the pulse is 0.5. The contribution to σ_{EP} from σ_{POW} is calculated by considering the Rabi formula (equation 2.16, page 16) in the case of zero detuning. The substitution $\Omega_R = 2\pi\sqrt{\frac{P}{P_i}}$ is made to account for the dependence of the Rabi frequency on the pulse power P relative to $P_i = 18$ μW to give:

$$\rho_{DD} = \sin^2\left(2\pi\sqrt{\frac{P}{P_i}}T\right). \tag{6.4}$$

First order error-propagation then dictates that

$$\sigma_{EP} = \frac{\partial\rho_{DD}}{\partial P}\sigma_{POW}. \tag{6.5}$$

The contribution from σ_r to σ_{EP} is calculated similarly, however the substitution

$$\Omega_R = 2\pi\sqrt{\mathrm{Exp}\Big(-2\frac{(r-r_0)^2}{w_0^2}\Big)}, \tag{6.6}$$

is made to account for the variation of the Rabi frequency due to shifts of the beam centre r about r_0 to yield:

$$\rho_{DD} = \sin^2\left(2\pi\sqrt{\mathrm{Exp}\Big(-2\frac{(r-r_0)^2}{w_0^2}\Big)}T\right). \tag{6.7}$$

As the Gaussian beam profile has zero slope at its centre, the Rabi frequency is first-order insensitive to small shifts in r, and only the second-order error

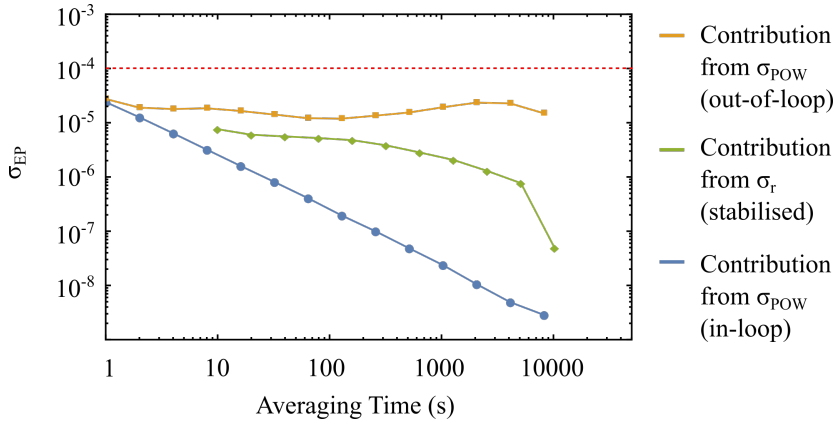

Figure 6.11: Allan deviation of the expectation value of a hypothetical $\pi/2$ rotation about an ideal value of 0.5 due to measured stability of the pulse power and position. The out-of-loop power measurement shows the system is sufficiently stable to maintain σ_{EP} at a value below the fault-tolerant threshold (red dashed line) for averaging times up to 8000 s.

contribution is considered as:

$$\sigma_{EP} = \frac{1}{2}\frac{\partial^2 \rho_{DD}}{\partial r^2}\sigma_r^2. \tag{6.8}$$

Figure 6.11 shows the contribution to σ_{EP} from σ_{POW} as deduced from in-loop and out-of-loop measurements of the pulse powers. Also shown is the contribution from σ_r in the case where the beam position at the ion is actively stabilised. Insight into the results may be gained from the following example. Consider an experiment lasting 200 s that consists of continuous cycles of qubit preparation, rotation via a nominal $\pi/2$ pulse and state measurement. When considering only the variations in the beam position (green line), the data implies that over many experiments the standard deviation in the average expectation probability measured in the first 100 s minus that measured in the second 100 s will approach $\sim 1.5{\times}10^{-5}$. The contributions to σ_{EP} from σ_{POW} as deduced from the out-of-loop measurement suggest an upper limit of $\sim 3{\times}10^{-5}$ over all averaging times, which is below the fault-tolerant target of $< 10^{-4}$. The data presented here therefore suggests that, in the absence of other sources of gate infidelity, the stable laser is ultimately capable of implementing single qubit rotations with an infidelity below the fault-tolerant threshold.

6.5 Conclusions

This chapter has described a stable laser system that is designed for implementing single rotations of an optical qubit with an infidelity approaching the fault-tolerant threshold. This is achieved via active stabilisation of the frequency, power and beam pointing of the pulses used to interrogate the ion. Through a phase-noise cancellation setup and optical injection locking, the frequency stability of an ultra-stable laser was transferred faithfully to the system. Using light that is picked off before the ion trap, a cascaded series of APDs is used to monitor the power of the interrogation pulses. With active feedback, the PSD of 10000 pulses over 100 s was reduced 1000-fold compared to the case where no stabilisation was employed. The relative power noise of 100 μs duration pulses was measured as $< 3.8 \times 10^{-3}$ over a range of 10^4 in optical power at the ion over 100 s. Furthermore, a stabilisation system was demonstrated that reduces RMS variations of the beam position in the plane of the trapped ion to ~ 150 nm over 22 hours. By changing the setpoint of this feedback loop, the excitation probability of a $^{88}Sr^{+}$ ion was measured as function of beam position in a single pulse spectroscopy experiment. This enabled the beam radii at the ion to be measured accurately. Long term measurements of the stabilised pulse powers and beam position suggest that the system is capable of implementing quantum gates where errors due to the addressing laser are less than the fault-tolerant threshold.

Chapter 7

Single-ion Spectroscopy with an Agile Laser

7.1 Introduction

A successful implementation of QIP [61] will require gate operations with fidelities above a fault-tolerant threshold [83]. Single and multi-qubit quantum gates with fault-tolerant fidelities have been demonstrated in a limited number of physical systems [41, 62] due to significant technical and fundamental advances. The gate fidelity, intuitively considered as the success probability of a target operation, is in practice defined by the combined error rate in an experimental sequence that executes the gate. For example, a typical single qubit operation with a trapped ion proceeds as follows. State initialisation begins the sequence, consisting of optical pumping to a desired electronic level and sideband cooling to the motional ground state of the system. Both are routinely achieved with fidelities exceeding 99 % [22, 25, 27]. Each operation is concluded with a measurement to determine the qubit state by imaging state-dependent fluorescence; a recent study demonstrated a single ion detection fidelity of 99.99 % [44]. In between initialisation and measurement, the qubit is manipulated with pulsed laser [22] fields that coherently transfer population between the qubit levels. This presents the most challenging aspect and is typically the dominant source of gate infidelities, especially as some operations involve sequences of many consecutive qubit rotations [47, 48].

One source of decoherence due to the state manipulation laser is off-resonant excitation into states outside of the computational basis of the qubit. This is particularly problematic when using short rotation pulses, as the wider spectral width leads to a greater probability of coupling to off-resonant transitions. This effect hence imposes a limit on the speed of quantum gates. The rate of off-resonant excitation can, however, be mitigated by smoothly shaping the temporal profile of the pulses, as was critical in achieving a two ion entangling gate fidelity of 99.3 % [41]. Similarly, an entangling phase gate using superconducting Josephson junction qubits also used pulse shaping of a microwave driving field to achieve an entangling gate fidelity of 99.4 % [62, 147]. Shaping of ultrafast laser pulses enabled selective entanglement of two ions in a five ion register with a fidelity of 95 % due to the suppression of multimode couplings [148]. Optimised pulse shapes also promise a route towards high-fidelity operations with qubits based on Rydberg states of single atoms [149]. Furthermore, a recent theoretical study has elucidated the potential speed up of gate operations when using shaped pulses [150], and interesting phenomena such as power narrowing have been predicted for some pulse shapes [151]. It is therefore clear that the temporal shape of qubit pulses is an important parameter for achieving high-fidelity gates.

Random rotation errors due to instabilities in the state manipulation laser and electromagnetic fluctuations in the environment are also significant sources of decoherence. These effects can be mitigated by reducing sources of noise [136] and through the use of spin-echo [87, 137] and noise filtering techniques [152] that serve to protect the qubit from technical decoherence. Spin-echo techniques have also been used for the spectral analysis of noise in the laboratory environment [153, 154]. Dephasing of the system due to ion heating also effectively reduces the system coherence, motivating a large body of work in understanding and reducing the so called anomalous heating in ion traps [155, 156, 157].

The purpose of this chapter is to demonstrate the capabilities of the agile laser via coherent control of the $^{88}Sr^{+}$ qubit with reference to their application to high-fidelity gate operations. Firstly, a theoretical description of the evolution of the qubit due to excitation with pulses of arbitrary shape is presented, along with a method of quantifying the associated reduction in off-resonant excitation

due to pulse shaping. After an initial demonstration of coherent control, spectral lineshapes due to excitation with square and amplitude-shaped pulses are measured. Using the formalism developed in this chapter, a maximum 11 dB reduction in off-resonant excitation due to pulse shaping is inferred for the case of a single qubit gate. The phase agility of the laser is also demonstrated with Rabi and Ramsey spectroscopy. Spin-echo experiments are conducted in an attempt to protect the qubit from technical noise in the experiment, and are used to identify limiting sources of decoherence. Finally, high-resolution spectroscopy of the quadrupole transition is performed to find a maximum coherence time of 1 ms.

7.2 Effect of pulse shape on qubit control

This section presents a model to describe the evolution of the qubit for excitation pulses of arbitrary temporal shape. From simulated spectral lineshapes, a reasoning is presented that quantifies the expected reduction in off-resonant excitation due the use of an amplitude-shaped pulse compared to a square pulse. This same reasoning is applied to experimental lineshapes in section 7.4.

An idealised two-level atom is considered, with energy levels $|S\rangle$ and $|D\rangle$ with a natural frequency splitting of ω_0 and with a natural linewidth Γ_{DS}. These are coupled by near resonant laser radiation at ω_L, with phase Φ and bandwidth Γ_L. To account for the effects of pulse shaping, a set of optical Bloch equations [24, 84] are generalised from those presented in section 2.3 to include a time-dependent Rabi frequency $\Omega_R(t)$. The optical Bloch equations describing the evolution of a two-level system with a laser pulse sequence are thus:

$$\dot{\tilde{\rho}}_{DS} = [i\delta - (\Gamma_L + \frac{1}{2}\Gamma_{DS})]\tilde{\rho}_{DS} - i\frac{\Omega_R(t)}{2}e^{-i\Phi}(\rho_{DD} - \rho_{SS}), \tag{7.1}$$

$$(\dot{\rho}_{DD} - \dot{\rho}_{SS}) = -\Gamma_{DS}[1 + (\rho_{DD} - \rho_{SS})] + i\Omega_R(t)(e^{-i\Phi}\tilde{\rho}^*_{DS} - e^{i\Phi}\tilde{\rho}_{DS}), \tag{7.2}$$

where ρ_{SS} and ρ_{DD} are the ground and excited state populations respectively, $\tilde{\rho}_{DS}$ represents the coherence and $\delta = (\omega_0 - \omega_L)$ is the detuning from resonance.

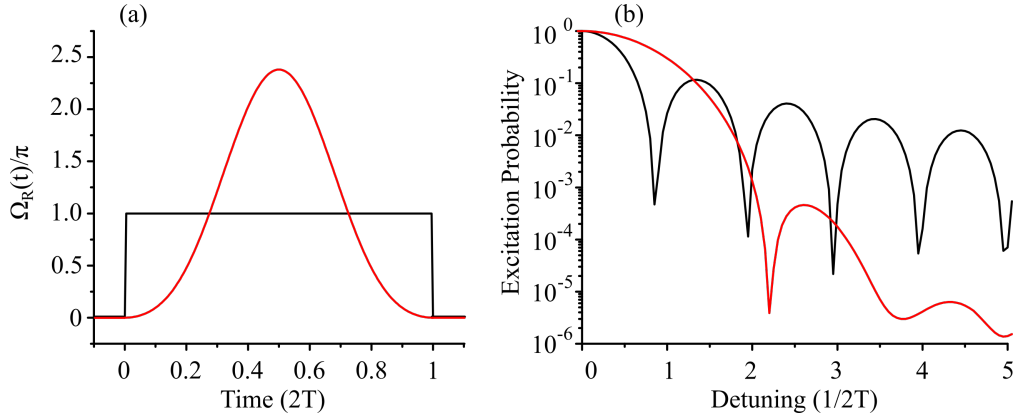

Figure 7.1: (a) Plot of E(t) for square and Blackman pulses. The area under each pulses is π, meaning all the population is transferred to the excited state when $\delta = 0$. (b) Excitation linewidths produced by the pulses shown in (a). The Blackman lineshape tails off more quickly compared to the square pulse lineshape, although the central feature is wider.

The equations are solved numerically with initial conditions $\rho_{SS} = 1$, $\rho_{DD} = 0$ and $\tilde{\rho}_{DS} = 0$ at $t = 0$. At the completion of the pulse at $t = 2T$, integration of the equations leads to $\rho_{DD} = 1$ when $\Omega_R(t)t = \pi$ and the laser is on resonance ($\delta = 0$). Such an interaction is termed a 'π pulse'. Off resonance ($\delta \neq 0$), the value of ρ_{DD} at $t = 2T$ depends on the shape of $\Omega_R(t)$, which is related to the optical pulse electric field amplitude $E(t)$ as $\Omega_R(t) \propto E(t)$.

In this chapter, amplitude-shaped pulses with a Blackman functional [124] form are employed, with an amplitude envelope $E(t)$ defined as in equation 5.1 (page 76). This functional form is practically identical in shape to a Gaussian, but with zero values at the beginning and end of the pulse. Figure 7.1(a) shows a square and Blackman pulse in the time domain. Both pulses have an area of π, and therefore produce complete population transfer for $\delta = 0$. The probability of excitation to the upper state as a function of detuning, $\rho_{DD}(\delta)$, is shown in figure 7.1(b). The excitation lineshape due to a Blackman pulse has a wider central feature compared to a square pulse, but the excitation probability tails off more quickly. This is related to the power spectral density of the square and amplitude-shaped pulses, as discussed in section 5.3.2.

The expected reduction in off-resonant excitation due to pulse shaping is quantified by considering the probability P_{OR} of exciting a hypothetical off-resonant transition, located at δ_{OR}, when $\delta = 0$. For cases when $P_{OR} \ll \rho_{DD}$, the level of off-resonant excitation is well approximated by,

$$P_{OR} = \rho_{DD}(\delta_{OR})\frac{\Omega_{OR}}{\Omega_R}, \tag{7.3}$$

where Ω_{OR} is the Rabi frequency that characterises the coupling strength between the laser and the off-resonant transition. For the case of $\delta_{OR} = 2.5/2T$, excitation with a Blackman pulse gives a ~ 100 fold reduction in the value of P_{OR} compared to a square pulse.

In the absence of pulse shaping, it is always possible to extend the duration of a square pulse (in the limit of the system coherence time) so that P_{OR} falls below the fault-tolerant threshold, at the expense of a reduced gate speed. Increasing the secular frequencies to the maximum permitted values is also an obvious method of reducing P_{OR} on sideband transitions for a given pulse duration and shape. However pulse shaping is a preferred technique, as due to the steeper gradient of the Blackman lineshape envelope in Fig. 7.1b, only small increments in pulse duration result in a large reduction in P_{OR}, whereas much bigger increases in duration are needed for square pulses. To illustrate this, figure 7.2 shows a plot of the excitation linewidth for a square pulse of $2T = 5$ μs and a Blackman pulse of $2T = 10$ μs. The Blackman lineshape envelope reaches $\rho_{DD} = 1 \times 10^{-3}$ at $\delta = 200$ kHz, whilst the square pulse lineshape reaches this level at $\delta = 3.3$ MHz. Therefore the expected value of P_{OR} is ultimately a trade-off between the gate speed, the detuning of the off-resonant level and its coupling strength relative to the target transition. However, pulse shaping offers significant reductions in P_{OR} for only modest reductions in the gate speed.

The simulations presented in this section assume the ion is initialised in the motional ground state. However, in the experiments presented in this chapter, the ion is in a thermal state. The implications of this with respect to the expected reduction in off-resonant excitation are discussed in section 7.4.

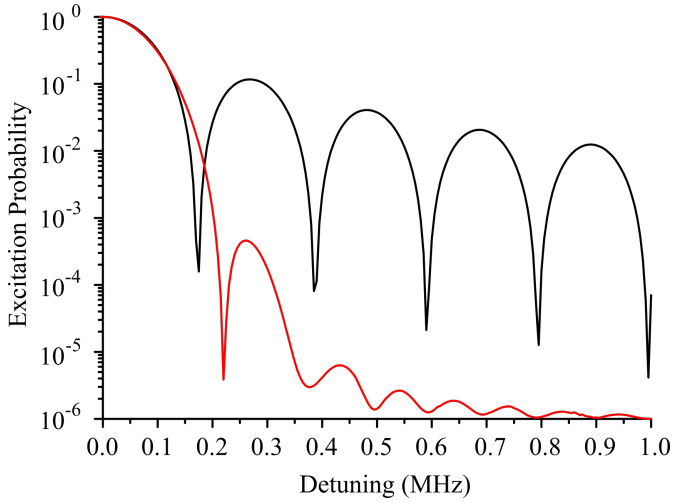

Figure 7.2: Excitation lineshapes for Blackman pulse of $2T = 10$ μs (red) and square pulse of $2T = 5$ μs (black). The peak Rabi frequency of each pulse is adjusted so that each produces complete population transfer on resonance.

7.3 Coherent control of the qubit

Single pulse spectroscopy of the quadrupole transition, as presented in section 4.5, is not an explicit demonstration of coherent control of the ion state with the 674 nm laser. The observation of Rabi oscillations is however an unambiguous demonstration of coherence. In such an experiment, the excitation probability is measured as a function of the duration of an interrogating pulse, with $\delta = 0$ and at a fixed intensity. For an ideal two level system in the absence of decoherence, the population oscillates with full contrast as a function of the pulse duration. However in reality two effects dampen the oscillation. Firstly the thermal distribution of the ion motional state causes dephasing due to the dependency of the Rabi frequency on the vibrational number (see section 4.6.3). Secondly, technical decoherence such as laser and magnetic field noise introduces random detuning errors which also reduce the contrast of Rabi oscillations with increasing pulse duration.

A demonstration of Rabi oscillations on the $S_{1/2}(m_j = -1/2)$ - $D_{5/2}(m_j = -5/2)$ qubit transition is shown in figure 7.3. The error bars are the statistical noise associated with each measurement, given as the (1σ) quantum projection noise [158]:

$$QPN(1\sigma) = \sqrt{\frac{\rho_{DD}(1-\rho_{DD})}{N}}, \tag{7.4}$$

where N is the number of interrogations performed at each setting of the parameters and ρ_{DD} is the measured excitation probability at each value of the pulse duration, calculated as the average value of N projective measurements. The size of the error bars demonstrate that the uncertainty in a single projective measurement increases from zero in the case where the Bloch vector points directly at one of the two poles on the Bloch sphere to complete uncertainty in the case where the Bloch vector points to the equator. In order to compare the quantum projection noise with experimentally measured error bars, it would have been necessary to calculate the standard deviation of many recorded values of ρ_{DD} at each value of the pulse duration. If the measured error bars were bigger than those dictated by equation 7.4, this would suggest that the measurement uncertainty were limited by technical noise, such as laser power and frequency variations, and not by the quantum projection noise. However, in this chapter only one value of ρ_{DD} was recorded for each data point, so only the quantum projection noise error bars are shown. Errors due to experimental fluctuations, such as drifts in laser frequency and ambient magnetic fields etc., are not explicitly accounted for. The 674 nm laser system was locked to the local master for the data presented in figure 7.3, as is the case in the rest of the experiments in this chapter unless stated otherwise.

A numerical model which integrates a set of optical Bloch equations, accounting for the effects of dephasing and decoherence, has been described in the PhD thesis of Valliappan Letchumanan [85]. Also included in this work is a method of fitting to data such as that shown in figure 7.3. In this method the excitation probability as a function of the pulse duration is approximated by superimposing sinusoidal solutions for each motional state n. Each solution is subject to the same decoherence rate Γ_L and is weighted according to the thermal distribution

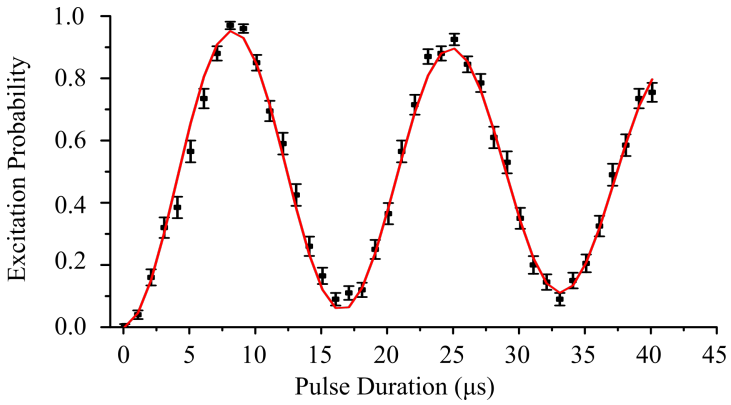

Figure 7.3: Rabi oscillation on the carrier of qubit transition, with error bars given as quantum projection noise. A maximum likelihood estimation technique is used to fit the solid line to the data, yielding a maximum likelihood value of the motional state of the axial mode of $\bar{n}_z = 11$. Each data point is the result of 200 interrogations.

given in equation 2.46 (page 26). To fit to the data, a method is used that iterates through values of $\bar{n}_z$, Ω_R and Γ_L to find a combination that maximises the probability of reproducing the observed data set. This technique is known as maximum likelihood estimation [159]. As there is some co-dependence between the parameters $\bar{n}_z$ and Γ_L, the value of Γ_L is constrained to 2 kHz $\pm$ 1 kHz in accordance with previously measured values (see section 6.3.1) in order to improve the estimate of $\bar{n}_z$. By applying this method to the data presented in figure 7.3, the estimated mean vibrational number of the axial mode is $\bar{n}_z = 11$. The other fitted parameters are the Rabi frequency $\Omega_R = 61.5$ kHz and $\Gamma_L = 1050$ Hz, the latter value is in rough agreement with that measured in section 6.3.1.

Dephasing is expected to be dominated by the axial motion, as the radial components are of > 2 times higher frequency and have a relatively weaker coupling to the 674 nm laser (see figure 4.2). Therefore dephasing due to the radial modes is neglected in the numerical simulations presented in the rest of this chapter, and only the value $\bar{n}_z = 11$ is used to describe the motional state of the ion.

7.4 Spectroscopy with amplitude-shaped pulses

The accurate and precise pulse shaping capabilities of the 674 nm agile laser were described and characterised in section 5.3.2. Furthermore the motivation for the amplitude-shaping of excitation pulses was elucidated in section 7.2 of this chapter. In this section, Rabi spectroscopy of the qubit transition is implemented experimentally using square and Blackman pulses. The resulting spectral lineshapes are compared with respect to the expected reduction in fidelity of a single qubit gate due to off-resonant excitation.

To investigate the effects of pulse shaping, an experiment was performed as to replicate the simulations presented in figure 7.2. The measured spectral lineshapes due to excitation with square pulses of $2T = 5$ μs and Blackman pulses of $2T = 10$ μs are presented in figure 7.4. The solid lines are simulations that account for the temporal shape of the excitation pulse and the motional state of the ion. A good agreement between the data and simulation exists in both instances. In the case of excitation with a Blackman pulse, the 'side-lobes' are effectively suppressed away from the carrier. This suppression can be readily quantified by comparing the lineshapes on a logarithmic scale as shown in figure 7.4(c). At a detuning of $\pm$ 0.27 MHz, there is a $\sim$ 11 dB reduction in excitation probability for the Blackman lineshape compared to the case of a square pulse, although this is at the expense of a longer pulse duration. This is significantly smaller than the 24 dB reduction one would expect from theory in the case of a ground state cooled ion at the same detuning (see figure 7.2). In practice, the thermal state of the ion limits the observable reduction in excitation probability due to pulse shaping for $\mid \delta \mid > 0.2$ MHz. Therefore, effective sideband cooling must be implemented to observe further reductions in the excitation probability at greater values of the detuning. If this were the case, the maximum reduction would be limited predominantly by laser and magnetic field noise and imperfections in the accuracy of pulse shaping.

With reference to figure 7.4, two experimental scenarios are considered with respect to the expected reduction in off-resonant excitation due to pulse shaping. Firstly the case when the desired excitation is on a carrier transition, and coupling to a hypothetical sideband at $\delta_{OR} = 0.27$ MHz is to be suppressed. A value of

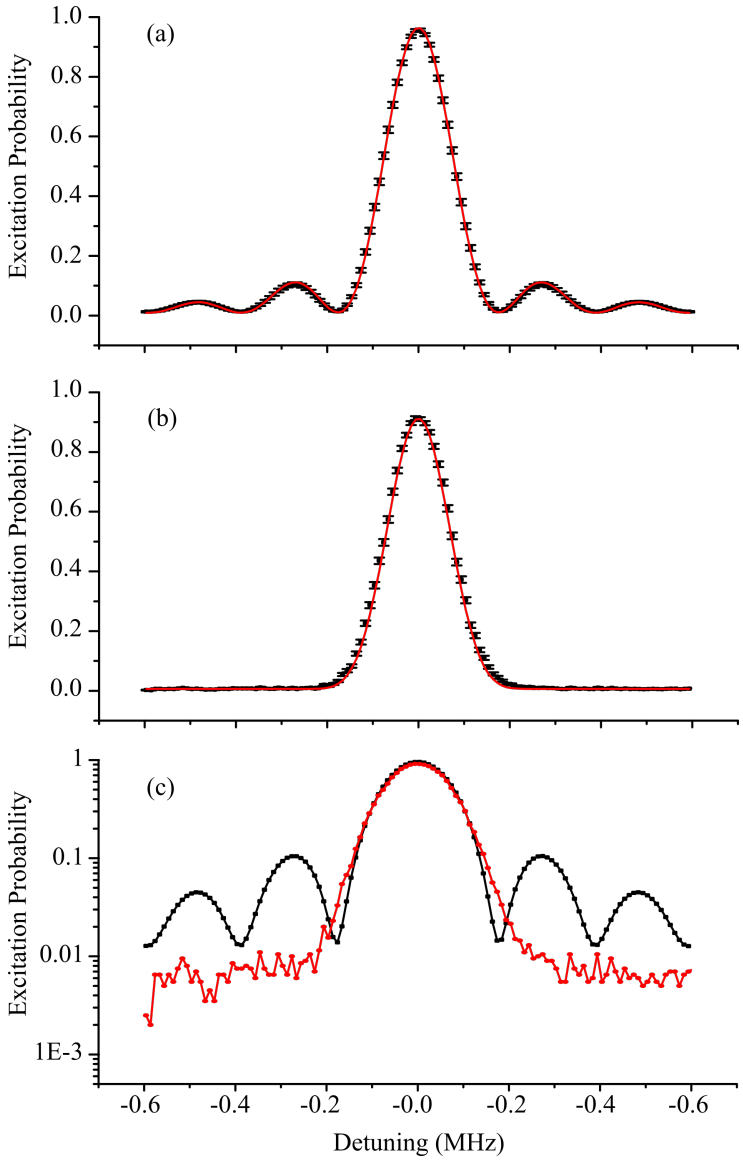

Figure 7.4: A frequency scan over the carrier transition using a square pulse of 5 μs duration (a) and a Blackman pulse of 10 μs duration (b). In both cases the red solid line is a numerical simulation that accounts for the temporal shape of the excitation pulse. In (c) the measured lineshapes due to excitation with square (black) and Blackman (red) pulses are shown on a logarithmic scale for comparison. 2000 interrogations are performed at each value of the detuning.

$\frac{\Omega_{OR}}{\Omega_R} = 0.25$ is assumed, as is typical of that found in an experiment (see figure 4.2). Using equation 7.3, this yields a value of $P_{OR} = 0.026$ for the square pulse and $P_{OR} = 0.002$ for the Blackman pulse. Secondly, the case of a targeted excitation on a sideband and unwanted off-resonant coupling on the carrier gives a ratio $\frac{\Omega_{OR}}{\Omega_R} = 4$. This gives $P_{OR} = 0.208$ for square pulse excitation and $P_{OR} = 0.016$ for Blackman pulse excitation. This latter scenario is the case when implementing the Mølmer-Sørensen gate, where entangled state generation occurs via simultaneous excitation on two sidebands that are symmetric about the carrier [39, 41]. In either case, the use of a Blackman pulse offers an 11 dB reduction in P_{OR} over a square pulse of half the duration.

Ramsey spectroscopy [24, 79] using amplitude-shaped pulses has also been performed (the concept of this technique was explained in chapter 2). Figure 7.5 shows a comparison of Ramsey spectra using square and Blackman shapes for the $\pi/2$ pulses. In each case, $\pi/2$ pulses of $2T = 10$ μs duration are separated by a free precession period of $\tau_R = 20$ μs. Numerical simulations are included in each figure using a model that accounts for the temporal shape of the Ramsey pulses. The envelope of figure 7.5(a) shows the coherent side-lobes as expected when using square-shaped interrogation pulses. In contrast, the envelope of the Ramsey lineshape is wider in figure 7.5(b) and tails off smoothly, as does the corresponding Rabi lineshape presented in figure 7.4. No loss of coherence is observed due to the use of Blackman over square-shaped interrogation pulses; this is further evidence that the phase coherence of the optical pulses is preserved in the pulse shaping process, as determined independently from optoelectronic measurements in section 5.3.3.

7.5 Phase agile spectroscopy

Accurate and precise phase modulation of the 674 nm laser was demonstrated in section 5.3.1, and was motivated in detail in the introduction to chapter 5. In this section this phase agility is demonstrated via coherent manipulation of a single $^{88}Sr^{+}$ ion, thus verifying that the phase steps can be implemented whilst maintaining coherence between the atom and 674 nm laser.

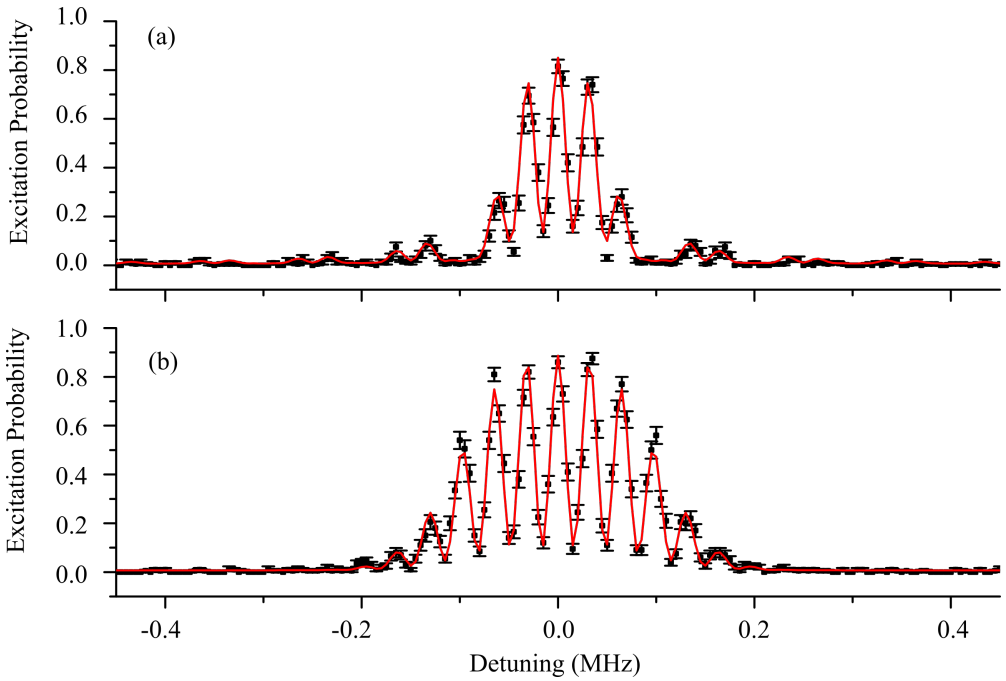

Figure 7.5: (a) Ramsey spectrum with square $\pi/2$ pulses of duration $2T$ =10 μs and a free precession period of τ_R = 20 μs. (b) A similar experiment, except Blackman shaped $\pi/2$ pulses of the same duration are used. The solid lines are numerical simulations of the Ramsey lineshapes that account for the temporal shape of the pulses. 200 interrogations are performed at each setting of the detuning.

The phase agility is demonstrated in both the time and frequency domains. Firstly, Rabi oscillations are demonstrated where the optical phase of the excitation pulse is switched by π at a programmed switching time (see figure 7.6). Also presented for comparison is a Rabi oscillation where no phase switch was made under otherwise identical conditions. The phase modulation effects a time reversal of the population evolution without reducing the contrast of the oscillation. Numerical simulations are included in both cases that account for the thermal state of the atom. In figure 7.6(c), the model accounts for a π shift in the optical phase of the interrogation laser at $2T$ = 15 μs. In this figure some of the data points deviate significantly from the simulation, possibly due to a change from the simulated ion temperature of $\bar{n}_z$ = 11 during the time taken to record this

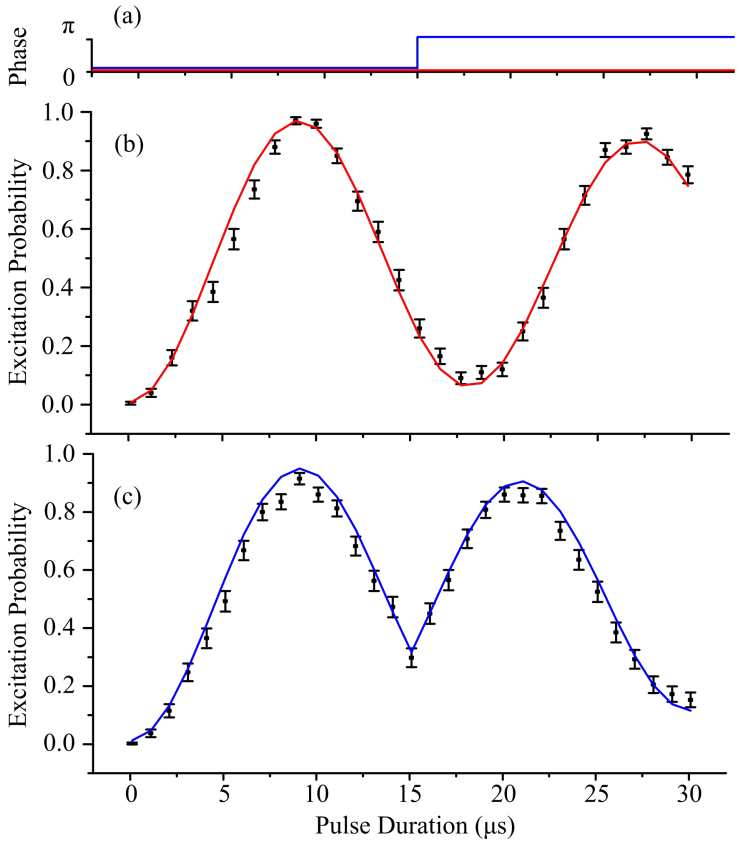

Figure 7.6: (a) The relative optical phase of the interrogation pulses used in (b) (red) and (c) (blue). In (c), the phase of the interrogation pulse is switched by π at $2T = 15$ μs. The solid lines are numerical simulations using the optical Bloch equations. 200 interrogations are performed at each setting of the pulse duration.

data. With previously demonstrated phase modulation techniques [24, 74], the phase is switched in a time period when light is not applied to the ion. However the technique presented here is unique as the phase is switched *during* the interrogation pulse. The system coherence is maintained as the optical switching time (30 ns, see section 5.2.2) is short compared to the microsecond timescale of the experiment.

Secondly, a phase-modulated Ramsey interrogation sequence is used to further verify that phase switching of the 674 nm laser does not compromise the coherence of the ion-laser interaction. Here Ramsey $\pi/2$ pulses of duration $2T = 4$ μs are separated by a free precession period of $\tau_R = 20$ μs. In figure 7.7(a), the two

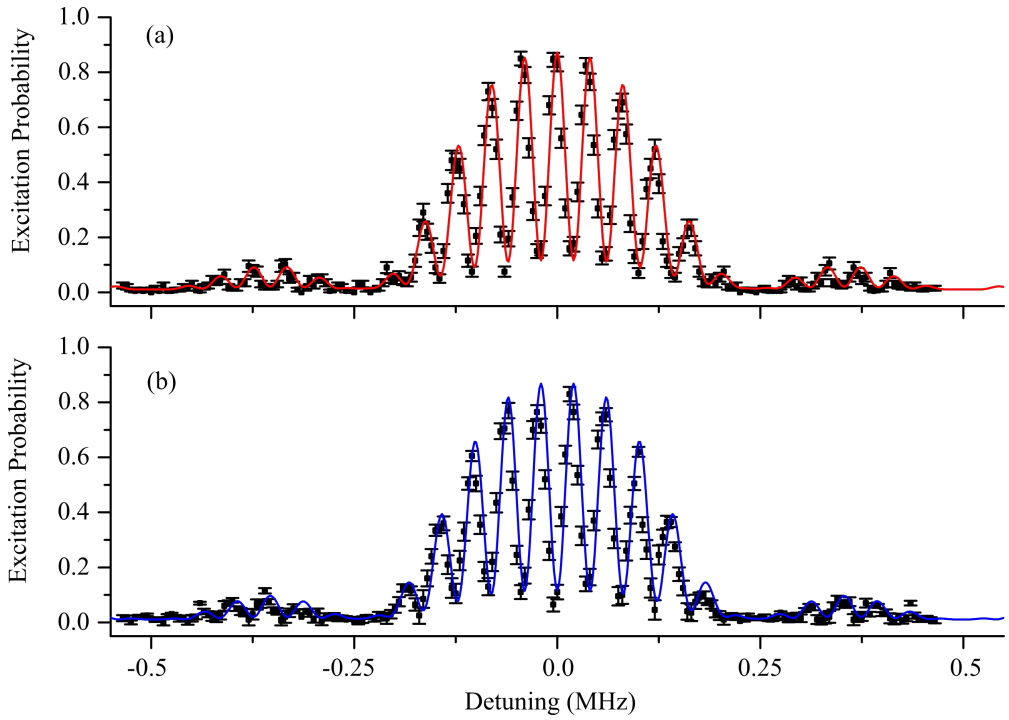

Figure 7.7: (a) Ramsey signal with no relative phase shift between the two $\pi/2$ pulses. In (b), an identical experiment is performed, except the phase of the interrogation laser is switched by π in between the Ramsey pulses. The solid lines are numerical simulations of the Ramsey lineshapes. 200 interrogations are performed at each setting of the detuning.

$\pi/2$ pulses have the same relative optical phase. However in figure 7.7(b) the phase of the second $\pi/2$ pulse is switched by π at a time half way through the free precession period. Again numerical simulations are presented; the conditions are identical for both plots, except the model accounts for the relative phase of the second Ramsey pulse in figure 7.7(b). The phase of the Ramsey fringe pattern is shifted by π as expected [24] due to the phase modulation of the second pulse, whilst the envelope is unaltered. Within the limits of the quantum projection noise, the phase-modulated Ramsey signal displays no reduction in contrast compared to the unmodulated case. Therefore it is reasonable to assume that the phase modulation does not reduce the coherence of the system.

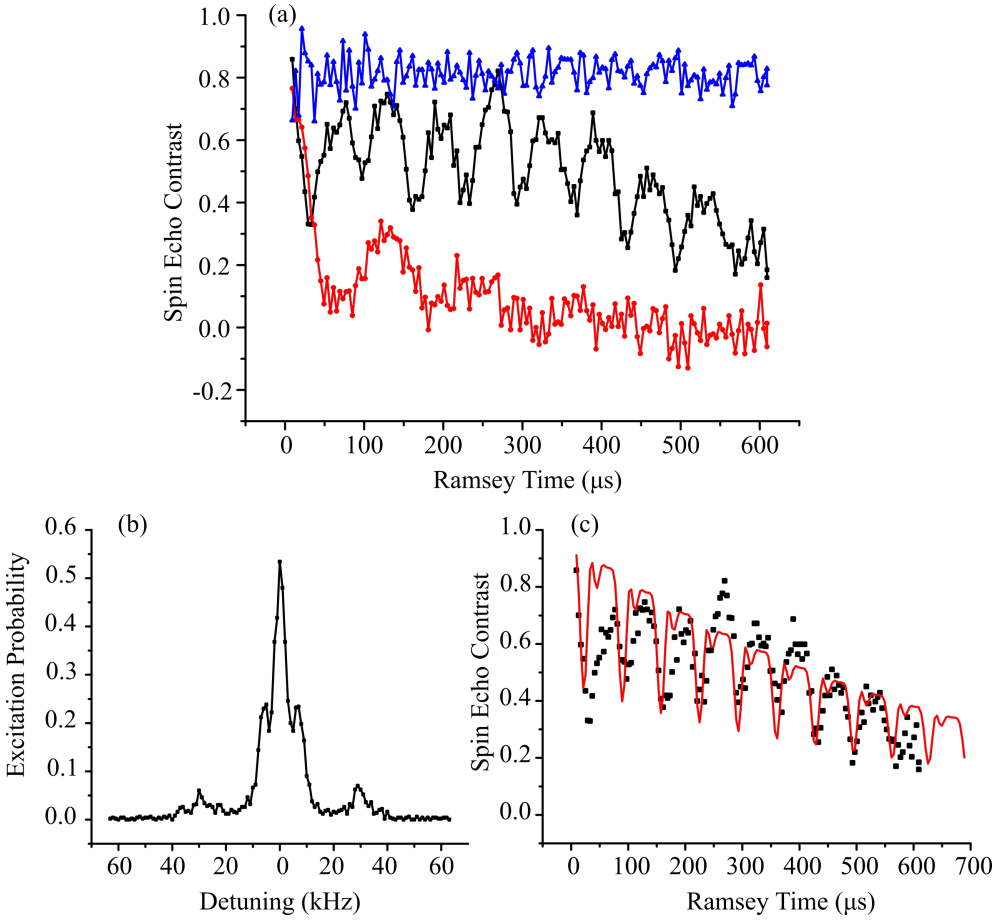

Figure 7.8: (a) Contrast as a function of Ramsey time for the spin-echo (black) and Ramsey sequences (red) when the 674 nm laser system is locked to the local master. Also shown is the spin-echo contrast when the 674 nm system is locked to the ultra-stable laser (blue). (b) A 674 nm frequency scan over the quadrupole transition shows the noise features that cause the oscillations in the spin-echo contrast shown in (c), which shows the black data from (a) and a numerical simulation as described in the main text.

7.6 Spin-echo spectroscopy

The principle of spin-echo spectroscopy was outlined in chapter 2, and the motivations for its use in ion trap systems, such as qubit storage and noise analysis, were discussed in the introduction to this chapter.

A basic spin-echo sequence is demonstrated in this section that significantly enhances the lifetime of the qubit. Square pulses of $2T = 4.5$ μs duration form the $\pi/2$ Ramsey pulses and are separated by two periods of free precession τ_{SE} and a $2T = 9$ μs duration π 'spin-echo' pulse (the total Ramsey time is the sum of the pulse durations and free precession periods). Two sets of data are acquired in order to produce each spin-echo decay presented in figure 7.8. Firstly, the excitation probability of the ion is measured as a function of the total free precession time (the pulse durations are unaltered) when the second Ramsey pulse has a zero phase shift with respect to the first. In the absence of decoherence and dephasing, the ion would be returned to the ground state at the end of this sequence. Secondly a similar experiment is performed, except the phase of the second Ramsey pulse is modulated by π with respect to the first; ideally complete population transfer to the excited state occurs in this scenario. If the excitation probabilities measured in the first and second experiments are P_{min} and P_{max} respectively, then the spin-echo contrast is defined as:

$$\text{Contrast} = \frac{P_{max} - P_{min}}{P_{max} + P_{min}}. \tag{7.5}$$

The black data in figure 7.8 shows the spin-echo contrast as a function of Ramsey time when the 674 nm laser is locked to the local stable laser (see section 6.2.1). Also shown in red is a similar experiment, except the spin-echo pulse is omitted; in which case the sequence reduces to a regular Ramsey experiment. Despite the spin-echo sequence offering significant improvement in the qubit lifetime for Ramsey times > 40 μs, there is a large amplitude oscillation in the spin-echo contrast at a frequency of ~ 15 kHz. After postulating that this was due to technical noise in the experiment, a medium resolution scan over the quadrupole transition was carried out using interrogation pulses of $2T = 200$ μs in order to identify any unwanted spectral features. This revealed unidentified features at $\pm$ 5.0 kHz and $\pm$ 29.6 kHz from the carrier (see figure 7.8(b)). A subsequent optical beat note measurement between the local master and the phase-noise cancelled ultra-stable laser also produced features at these frequencies. This suggests that the extra spectral features are the result of an unwanted frequency modulation of the master laser rather than unknown transitions of the trapped ion (e.g.

second order sidebands of a different Zeeman component). By including a sinusoidal modulation of the detuning δ at 29.6 kHz in the first term of equation 7.1, the effect of laser noise at this frequency on the spin-echo decay was simulated, as shown in figure 7.8(c). Whilst the simulation is only a reasonable match with the data, the result does suggest the oscillations in the spin-echo contrast are due the frequency modulation of the master laser. This is a basic demonstration of the applicability of the spin-echo technique for spectral analysis.

When an identical spin-echo experiment is conducted when the 674 nm system is locked to the ultra-stable laser, the contrast remains at ~ 0.85 up to the maximum recorded Ramsey time of 600 μs (blue, figure 7.8(a)). The contrast here is limited by the thermal state of the ion and intensity drifts of the probe laser. However the results show the long coherence times that could potentially be achieved with the ultra-stable laser. This is explored further in the next section, where the limits of coherence in the system are investigated.

7.7 High resolution spectroscopy

The precision of optical frequency standards and quantum metrology schemes utilising trapped ion systems is ultimately limited by the coherence time of the system. For optical qubits, a fundamental limit is the natural lifetime of the chosen transition, which for the $^{88}Sr^{+}$ qubit used in this work is 0.39 s [29]. However technical noise, due to instabilities in the addressing laser and ambient magnetic fields etc., causes decoherence on a timescale that is typically faster than that due to the transition lifetime.

In this section, high-resolution scans over the qubit transition are performed in order to find the maximum possible coherence time in the current experimental configuration. Initially interrogation sequences were executed at the maximum rate (~ 100 Hz) that is permitted by the experimental control system (see section 3.4). No hardware timing is implemented in this case, resulting in shot-to-shot jitter of a few milliseconds in the time between interrogation cycles from one sequence to the next. In this scenario, it was not possible to observe Fourier-limited linewidths of < 15 kHz. This limitation was attributed to a.c. magnetic field noise from the laboratory mains power supplies that causes random detuning

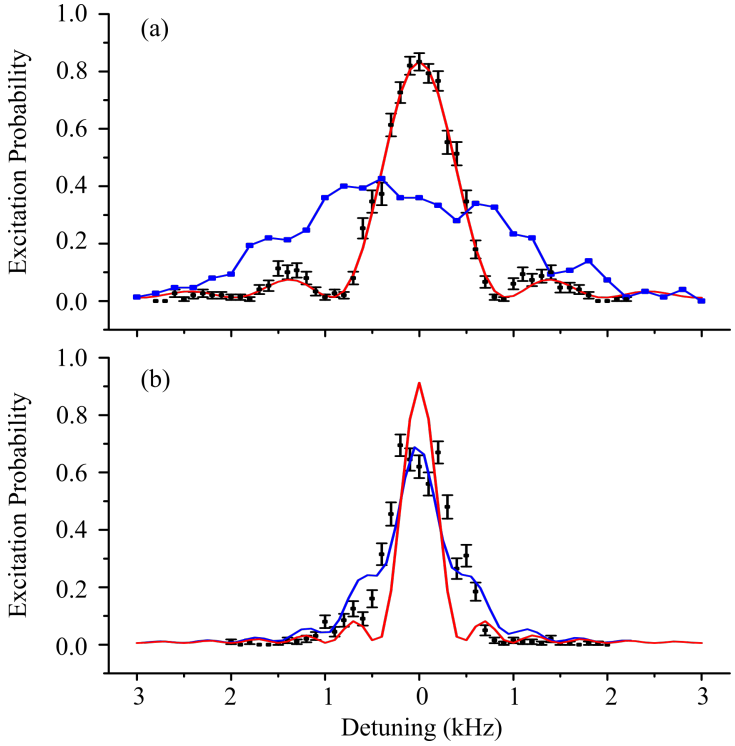

Figure 7.9: (a) Frequency scan over the qubit transition with a $2T = 1$ ms probe pulse when locked to the ultra-stable laser. The red solid line is a numerical simulation $\Gamma_L = 9$ Hz. Also shown in blue is the measured lineshape when locked to the local master. (b) A similar experiment with a $2T = 2$ ms interrogation pulse. The solid lines are numerical simulations with (blue) and without (red) accounting for 50 Hz magnetic field noise. 150 interrogations are performed at each value of the detuning in both figures.

errors in each interrogation due to the Zeeman effect; when averaged over many measurements, this results in a significant reduction in the system coherence.

Higher resolution was only achieved when the experimental sequence was triggered by the a.c. mains frequency at 50 Hz, as was the case with the high-resolution scans shown in figure 7.9(a). Here the spectral lineshape was measured using a probe pulse of duration $2T = 1$ ms under two conditions. Firstly when the 674 nm system was locked to the ultra-stable laser and secondly when locked to the local master. A numerical simulation, with $\Gamma_L = 9$ Hz, is also presented in the case of the ultra-stable laser. Here the simulated Rabi frequency is empiri-

cally adjusted to provide the closest match to the data. The simulation and data are in close agreement, and a Fourier limited linewidth of 1 kHz is observed in this case. Furthermore the side-lobes are a signature of coherence, and would not be observed if the linewidth were limited by technical noise. For example, when the 674 nm laser is locked to the local master, the observed linewidth is limited by that of the probe laser. The observed FWHM linewidth of 2.7 kHz is slightly larger than the value of 1.9 kHz measured from an optical beat note in section 6.3.1, possibly due to thermal drift of the centre frequency over the time required to acquire the data.

Figure 7.9(b) shows the measured lineshape using a $2T = 2$ ms interrogation pulse when locked to the ultra-stable laser. The absence of the side-lobes indicates a significant reduction in the system coherence, and the observed linewidth is greater than expected from the Fourier-limited case, which is demonstrated by a numerical simulation indicated by the red solid line. Decoherence due to the $\Gamma_L = 9$ Hz bandwidth of the ultra-stable laser should not be significant at this timescale, and is ruled out as the dominant source of decoherence. However the a.c. magnetic field due to the 50 Hz mains cycles through 10 % of its total period during the $2T = 2$ ms interrogation pulse, and is therefore a likely source of decoherence at this timescale. The blue solid line in figure 7.9(b) is a simulation where the detuning δ in equation 7.1 is modulated at 50 Hz. As the simulation is in rough agreement with the data, it is deduced that the maximum spectral resolution is limited by a.c. magnetic fields at the ion.

This source of decoherence will be greatly reduced by the imminent installation of a multi-layer mu-metal magnetic shield, which has been measured by Guido Wilpers to attenuate fields at 50 Hz up to a factor of 1000. A further significant limitation to the work presented in this section was the considerable difficulty in accurately and reliably setting the very low optical powers (~ 10 nW) required to achieve a π pulse with a $2T \sim 1$ ms interrogation pulse. This motivated an improvement to the system where optical pulses are produced with high stability over a large dynamic range, as described in chapter 6. This enhanced laser system, when employed simultaneously with the magnetic shield, should allow Fourier-limited linewidths of ~ 10 Hz to be observed.

7.8 Conclusions

The application of the agile laser system to high-fidelity operations with a single $^{88}Sr^{+}$ ion has been described in this chapter. Firstly a numerical model was presented that describes how the optical qubit evolves with excitation due to pulses of arbitrary temporal shape. Using simulated lineshapes, a method of quantifying the expected reduction in off-resonant excitation due to the temporal shaping of the optical pulse was described.

Experimentally, coherent control of the ion was initially shown via Rabi oscillations. From the decay of the coherence, an estimation was made of the mean motional number of the axial mode. This was used in the numerical simulations presented in the chapter. Spectral lineshapes were acquired in Rabi spectroscopy experiments that used both square and amplitude-shaped pulses. A maximum 11 dB reduction in the probability of off-resonant excitation of a hypothetical sideband was observed using a Blackman pulse over a square pulse of only half the duration. Greater reductions should be possible using Blackman pulses, however these could not be observed due to the thermal state of the ion. Ramsey spectroscopy was also performed using square and Blackman pulses to confirm that the pulse shaping process does not destroy the phase coherence of the atom-laser interaction. The phase switching capabilities of the agile laser were also demonstrated via two methods. Firstly, a π phase switch of the probe pulse in a Rabi oscillation experiment reversed the temporal evolution of the qubit. Secondly, a π relative phase modulation between two Ramsey pulses caused a π shift of a Ramsey fringe pattern. All observed lineshapes are well described by numerical simulations that account for the temporal shape of the excitation pulses. The model was extended beyond a previously existing version [85] in the course of this work to account for the effects of phase agility and pulse shaping in Rabi, Ramsey and spin-echo spectroscopy.

A basic demonstration of spin-echo spectroscopy has also been implemented. With the 674 nm laser locked to the local master, oscillations in the spin-echo contrast were observed at $\sim$ 15 kHz; these were attributed to technical noise in the interrogating laser. With the 674 nm system locked to the ultra-stable laser, a contrast of $\sim$ 0.85 was measured up to the maximum Ramsey time of 600 μs.

No oscillations in the contrast were detected in this case. Finally, high resolution scans over the qubit transition were carried out to measure a minimum Fourier-limited linewidth of 1 kHz; magnetic field noise was found to be the limiting source of decoherence. However this is still a $\sim$ 20 fold improvement on the coherence times found in previously published work from this experiment [24].

Chapter 8

Conclusions and Outlook

8.1 Summary

This thesis has described several experiments relating to the coherent spectroscopy of a single $^{88}Sr^{+}$ ion in a microfabricated ion trap. Specifically, this work has focused on the application of an agile and stable qubit manipulation laser system to implementing high-fidelity quantum gate operations, as would be required for fault-tolerant QIP with trapped ions. The techniques presented here are relevant to the long-term goal of this project, which is to implement robust single qubit and multi-qubit entangling operations in a scalable trapping architecture. A number of experimental techniques have been implemented for the first time using the microtrap, including a characterisation and elimination of the residual micromotion. After the minimisation of the magnetic field at the trapped ion, its motion in the pseudopotential was characterised using single-pulse (Rabi) spectroscopy, and the measured secular frequencies were found to be in good agreement with an earlier model [100]. Three aspects of high efficiency state preparation have also been demonstrated. Firstly, after compensating the stress-induced birefringence of the optical windows, σ^{-} 422 nm light could be produced at the ion, enabling optical pumping to the $S_{1/2}(m_j = -1/2)$ Zeeman level. A pumping efficiency of 98.8 % was measured for a pulse duration of 20 μs using this polarisation-resolved technique. As this method has inherent limitations to the efficiency, a second state preparation technique of frequency-resolved optical pumping was investigated for the first time using $^{88}Sr^{+}$. By selectively excit-

ing the $S_{1/2}(m_j = 1/2)$ - $D_{5/2}(m_j = -3/2)$ transition with 674 nm light in the presence of the 1033 nm quench, an optical pumping efficiency of 99.8 % was measured. Finally, progress has been made towards high efficiency ground state cooling [27]. A minimum mean occupation of the axial mode of $\bar{n}_z = 0.3$ was measured, limited by the low axial frequency of $\omega_z = 865$ kHz, as dictated by practical limitations of the microtrap. Furthermore, deterministic ion transport between segments of the microtrap has been demonstrated, albeit at a modest maximum shuttling frequency of 1 kHz.

A major part of this work has been the construction and characterisation of an agile laser at 674 nm that is designed to manipulate the qubit transition in $^{88}Sr^{+}$ [117]. The main motivation of this was to realise a system capable of implementing the most advanced coherent manipulation routines, where complex sequences of many pulses are required [47, 48]. By utilising a DDS RF source, phase steps could be accurately implemented at a minimum resolution of 10 mrad. The system is also capable of producing optical pulses of arbitrary temporal shape with high accuracy and precision for pulse durations ranging over 6 orders of magnitude. This enabled the Fourier spectrum of optical pulses to be tailored according to the requirements of a particular quantum gate. In terms of frequency agility, an upgrade of a sideband injection lock [120] enabled agile frequency switches to be made on a timescale limited only by the 5 ns response time of a DDS source. Switching between single frequency and bichromatic operation was also demonstrated on a sub-μs timescale, as required for implementing the Mølmer-Sørensen entangling gate [41]. This work represents a major upgrade to the previous system [24, 110], where each beam in an experimental sequence could only produce pulses of fixed phase, amplitude and frequency.

Also described in this work is the stabilisation of the system detailed above in terms of frequency, pulse power and beam pointing, as required to realise robust quantum gates with repeatable high fidelity. Crucially, the stabilisation schemes do not compromise the agility of the system. Through the use of a phase-noise cancellation system, the frequency stability of an ultra-stable laser was transferred to the agile laser to realise a linewidth of 9 Hz and drift rate of ~ 2 Hz/s [144]. Furthermore, by using a series of cascaded avalanche photodiodes to monitor a portion of the interrogation pulses, a relative power stability of 3.8 $\times 10^{-3}$ was

measured over a range of 10^4 in optical power through the use of active feedback for pulses of 100 μs duration. Similarly, by monitoring a quadrant photodiode, the position of the beam at the ion could be stabilised to 150 nm RMS over 22 hours at an adjustable setpoint. This enabled the beam to be accurately profiled inside the vacuum chamber by measuring the excitation probability of a single $^{88}Sr^+$ ion as a function of beam position. From calculations of the expected long-term fidelity of a simple qubit rotation implemented with the stable laser, it is deduced that the system is capable of implementing quantum gates with fault-tolerant levels of infidelity. Further to the construction of the agile and stable laser, several other technical improvements to the experiment were made during the course of this work. This includes the construction and characterisation of a temperature-controlled tunable cavity of low thermal drift, designed for the frequency stabilisation of the 1033 nm quench beam. The measured drift rate of 2 MHz/hr is a significant improvement on the previous version [90], and allows the quench laser to operate for many hours without the frequency having to be manually corrected. Also the experimental control system [85] was significantly updated to accommodate the advanced switching and stabilisation capabilities of the 674 nm laser.

This work concludes with a demonstration of the capabilities of the agile laser through the coherent spectroscopy of a single $^{88}Sr^+$ ion. Particularly, after a theoretical description of the advantages of pulse shaping with respect to high-fidelity gates, Blackman shaped pulses were used to demonstrate a 11 dB reduction in the expected level of off-resonant excitation compared to the case of square pulses. Further reductions could be expected if the ion was effectively sideband cooled. The phase agility of the laser was verified using Ramsey as well as time-domain Rabi spectroscopy, and it was deduced that the phase modulation process does not induce extra decoherence. Spin-echo sequences [87] were also successfully employed to significantly enhance the storage time of the qubit, and was used to effectively identify sources of technical noise in the experiment. Finally, the system coherence time was measured as 1 ms, limited by residual a.c magnetic field noise in the laboratory.

8.2 Future work

A major limitation to the work presented in this thesis has been the gradual degradation in the performance of the microfabricated ion trap used in all the experiments presented herein. This was manifest as an increasingly high and erratic heating rate, which made experiments such as sideband cooling infeasible to implement with high efficiency. Several procedures were attempted to mitigate this effect, including a week long bake of the trap and associated UHV apparatus. However no improvement in performance was found. A new batch of microfabricated ion traps are currently in production, and with an improved design and fabrication process, it is reasonable to expect that these traps will offer a low heating rate that is sustainable over a longer period of time. This will allow full optimisation of the sideband cooling process.

The characterisation of the agile and stable qubit manipulation laser, as presented in this thesis, suggests that the system is capable of performing gate operations with a fault tolerant fidelity. However this can only be verified when other sources of decoherence are not limiting factors. To enter this regime, highly efficient state preparation will have to implemented, as well as the reduction of magnetic field noise through the installation of a mu-metal shield. With these conditions satisfied, the Mølmer-Sørensen gate could be implemented with a fidelity matching or bettering the current record of 99.3 % [41] for optical qubits. A further target would be to match the recently achieved benchmark of 99.9% fidelity using $^{43}Ca^{+}$ hyperfine qubits [160].

High-fidelity entanglement creation will also allow the demonstration of quantum metrology schemes such as Heisenberg-limited spectroscopy [81] with optical qubits, and the creation of decoherence free sub-spaces [25]. Also, with an improved electronic configuration, it will be possible to implement deterministic ion transport on the microsecond timescale. With this capability, the decoherence of entangled and superposition states of two or more ions due to ion transport could be tested. If successfully implemented, these experiments would constitute significant progress towards practical QIP with trapped ions.

8.3 Research outputs

The work described in this thesis has resulted in the following publications:

- J. Thom, G. Wilpers, E. Riis, and A. G. Sinclair, Accurate and agile digital control of optical phase, amplitude and frequency for coherent atomic manipulation of atomic systems, Optics Express **21**, 18712 (2013), **Refereed Journal Publication**

- J. Thom, G. Wilpers, E. Riis, and A. G. Sinclair, Coherent manipulations in a microfabricated ion trap, Proceedings of the International School of Physics, Enrico Fermi Course CLXXXIX, Varenna (2015), **Refereed Proceedings Article**

- J. Thom, B.Yuen, G. Wilpers, E. Riis, and A. G. Sinclair, An optical system for high-fidelity quantum coherent control of an optical qubit, **Journal Publication in Preparation**

Presentations of this work given by the author of this thesis:

- An optical system for high-fidelity coherent quantum control of atomic systems, QuAMP, 1-4 September 2015, Sussex, **Poster Presentation**

- Agile coherent control of ions in a microfabricated ion trap, International Conference on Atomic Physics, 3-8 August 2014, Washington DC, **Poster Presentation**

- Coherent operations in a microfabricated ion trap, QuAMP, 8-12 September 2013, Swansea, **Oral Presentation**

- Coherent manipulations in a microfabricated ion trap, Enrico Fermi Summer School CLXXXIX, 22-30 July 2013, Varenna, **Poster Presentation**

Bibliography

[1] J. I. Cirac and P. Zoller, *Quantum Computations with Cold Trapped Ions*, Phys. Rev. Lett. **74**, 4091 (1995).

[2] R. Feynman, *Simulating physics with computers*, Int. J. Th. Phys. **21**, 467 (1982).

[3] P. Shor, *Algorithms for quantum computation: discrete logarithms and factoring*, in *Proceedings of the 35th Annual Symposium on the Foundations of Computer Science*, pp. 124–134, 1994.

[4] L. K. Grover, *Quantum Mechanics Helps in Searching for a Needle in a Haystack*, Phys. Rev. Lett. **79**, 325 (1997).

[5] D. Deutsch and R. Jozsa, *Rapid Solution of Problems by Quantum Computation*, Proc. Mat. Phys. Sci. **439**, 553 (1992).

[6] I. M. Georgescu, S. Ashhab, and F. Nori, *Quantum simulation*, Rev. Mod. Phys. **86**, 153 (2014).

[7] D. P. DiVincenzo, *The Physical Implementation of Quantum Computation*, Fortschr. Phys. **48**, 771 (2000).

[8] D. Kielpinski, C. Monroe, and D. J. Wineland, *Architecture for a large-scale ion-trap quantum computer*, Nature **417**, 709 (2002).

[9] D. L. Moehring *et al.*, *Design, fabrication and experimental demonstration of junction surface ion traps*, New J. Phys. **13**, 075018 (2011).

[10] R. B. Blakestad *et al.*, *High-Fidelity Transport of Trapped-Ion Qubits through an X-Junction Trap Array*, Phys. Rev. Lett. **102**, 153002 (2009).

[11] K. Wright *et al.*, *Reliable transport through a microfabricated X-junction surface-electrode ion trap*, New J. Phys. **15**, 033004 (2013).

[12] D. Leibfried, R. Blatt, C. Monroe, and D. Wineland, *Quantum dynamics of single trapped ions*, Rev. Mod. Phys. **75**, 281 (2003).

[13] D. Cho, S. Hong, M. Lee, and T. Kim, *A review of silicon microfabricated ion traps for quantum information processing*, Micro Nano Sys. Lett. **3** (2015).

[14] M. D. Hughes, B. Lekitsch, J. A. Broersma, and W. K. Hensinger, *Microfabricated ion traps*, Contemp. Phys. **52**, 505 (2011).

[15] C. Monroe, D. M. Meekhof, B. E. King, W. M. Itano, and D. J. Wineland, *Demonstration of a Fundamental Quantum Logic Gate*, Phys. Rev. Lett. **75**, 4714 (1995).

[16] D. Leibfried *et al.*, *Experimental demonstration of a robust, high-fidelity geometric two ion-qubit phase gate*, Nature **422**, 412 (2003).

[17] T. P. Harty *et al.*, *High-Fidelity Preparation, Gates, Memory, and Readout of a Trapped-Ion Quantum Bit*, Phys. Rev. Lett. **113**, 220501 (2014).

[18] S. Olmschenk *et al.*, *Manipulation and detection of a trapped* Yb^+ *hyperfine qubit*, Phys. Rev. A **76**, 052314 (2007).

[19] A. Keselman, Y. Glickman, N. Akerman, S. Kotler, and R. Ozeri, *High-fidelity state detection and tomography of a single-ion Zeeman qubit*, New J. Phys **13**, 073027 (2011).

[20] M. J. McDonnell *et al.*, *High-Efficiency Detection of a Single Quantum of Angular Momentum by Suppression of Optical Pumping*, Phys. Rev. Lett. **93**, 153601 (2004).

[21] J. A. Sherman *et al.*, *Experimental Recovery of a Qubit from Partial Collapse*, Phys. Rev. Lett. **111**, 180501 (2013).

[22] C. Roos *et al.*, *Quantum State Engineering on an Optical Transition and Decoherence in a Paul Trap*, Phys. Rev. Lett. **83**, 4713 (1999).

[23] S. X. Wang, J. Labaziewicz, Y. Ge, R. Shewmon, and I. L. Chuang, *Demonstration of a quantum logic gate in a cryogenic surface-electrode ion trap*, Phys. Rev. A **81**, 062332 (2010).

[24] V. Letchumanan, P. Gill, E. Riis, and A. G. Sinclair, *Optical Ramsey spectroscopy of a single trapped $^{88}Sr^{+}$ ion*, Phys. Rev. A **70**, 033419 (2004).

[25] C. F. Roos, M. Chwalla, K. Kim, M. Riebe, and R. Blatt, *'Designer atoms' for quantum metrology*, Nature **443**, 316 (2006).

[26] F. Diedrich, J. C. Bergquist, W. M. Itano, and D. J. Wineland, *Laser Cooling to the Zero-Point Energy of Motion*, Phys. Rev. Lett. **62**, 403 (1989).

[27] V. Letchumanan, G. Wilpers, M. Brownnutt, P. Gill, and A. Sinclair, *Zero-point cooling and heating-rate measurements of a single $^{88}Sr^{+}$ ion*, Phys. Rev. A **75**, 063425 (2007).

[28] C. Langer *et al.*, *Long-Lived Qubit Memory Using Atomic Ions*, Phys. Rev. Lett. **95**, 060502 (2005).

[29] V. Letchumanan, M. A. Wilson, P. Gill, and A. G. Sinclair, *Lifetime measurement of the metastable $4d^2D_{5/2}$ state in $^{88}Sr^{+}$ using a single trapped ion*, Phys. Rev. A **72**, 012509 (2005).

[30] T. Monz *et al.*, *14-Qubit Entanglement: Creation and Coherence*, Phys. Rev. Lett. **106**, 130506 (2011).

[31] D. A. Lidar, I. L. Chuang, and K. B. Whaley, *Decoherence-Free Subspaces for Quantum Computation*, Phys. Rev. Lett. **81**, 2594 (1998).

[32] D. Kielpinski *et al.*, *A Decoherence-Free Quantum Memory Using Trapped Ions*, Science **291**, 1013 (2001).

[33] K. R. Brown *et al.*, *Single-qubit-gate error below* 10^{-4} *in a trapped ion*, Phys. Rev. A **84**, 030303 (2011).

[34] P. Schindler *et al.*, *A quantum information processor with trapped ions*, New J. Phys. **15**, 123012 (2013).

[35] H. C. Nägerl *et al.*, *Laser addressing of individual ions in a linear ion trap*, Phys. Rev. A **60**, 145 (1999).

[36] N. Timoney *et al.*, *Quantum gates and memory using microwave-dressed states*, Nature **476**, 185 (2011).

[37] C. Piltz, T. Sriarunothai, A. Varón, and C. Wunderlich, *A trapped-ion-based quantum byte with* 10^{-5} *next-neighbour cross-talk*, Nat. Commun. **5** (2014).

[38] M. Riebe *et al.*, *Process Tomography of Ion Trap Quantum Gates*, Phys. Rev. Lett. **97**, 220407 (2006).

[39] A. Sørensen and K. Mølmer, *Quantum Computation with Ions in Thermal Motion*, Phys. Rev. Lett. **82**, 1971 (1999).

[40] K. Mølmer and A. Sørensen, *Multiparticle Entanglement of Hot Trapped Ions*, Phys. Rev. Lett. **82**, 1835 (1999).

[41] J. Benhelm, G. Kirchmair, C. F. Roos, and R. Blatt, *Towards fault-tolerant quantum computing with trapped ions*, Nature Phys. **4**, 463 (2008).

[42] G. Kirchmair *et al.*, *High-fidelity entanglement of* $^{43}Ca^{+}$ *hyperfine clock states*, Phys. Rev. A **79**, 020304 (2009).

[43] H. Dehmelt, *Monoion oscillator as potential ultimate laser frequency standard*, IEEE Trans. Instrum. Meas. **1001**, 83 (1982).

[44] A. Burrell, D. Szwer, S. Webster, and D. Lucas, *Scalable simultaneous multiqubit readout with 99.99% single-shot fidelity*, Phys. Rev. A **81**, 040302 (2010).

[45] M. Acton *et al.*, *Near-perfect Simultaneous Measurement of a Qubit Register*, Quant. Inf. Comp. **6**, 465 (2006).

[46] A. H. Myerson *et al.*, *High-Fidelity Readout of Trapped-Ion Qubits*, Phys. Rev. Lett. **100**, 200502 (2008).

[47] M. D. Barrett *et al.*, *Deterministic quantum teleportation of atomic qubits*, Nature **429**, 737 (2004).

[48] M. Riebe *et al.*, *Deterministic quantum teleportation with atoms*, Nature **429**, 734 (2004).

[49] S. Olmschenk *et al.*, *Quantum Teleportation Between Distant Matter Qubits*, Science **323**, 486 (2009).

[50] J. Chiaverini *et al.*, *Realization of quantum error correction*, Nature **432**, 602 (2004).

[51] K.-A. Brickman *et al.*, *Implementation of Grover's quantum search algorithm in a scalable system*, Phys. Rev. A **72**, 050306 (2005).

[52] S. Gulde *et al.*, *Implementation of the Deutsch-Jozsa algorithm on an ion-trap quantum computer*, Nature **421**, 48 (2003).

[53] R. Bowler *et al.*, *Coherent Diabatic Ion Transport and Separation in a Multizone Trap Array*, Phys. Rev. Lett. **109**, 080502 (2012).

[54] A. Walther *et al.*, *Controlling Fast Transport of Cold Trapped Ions*, Phys. Rev. Lett. **109**, 080501 (2012).

[55] N. A. Gershenfeld and I. L. Chuang, *Bulk Spin-Resonance Quantum Computation*, Science **275**, 350 (1997).

[56] B. E. Kane, *A silicon-based nuclear spin quantum computer*, Nature **393**, 133 (1998).

[57] E. Knill, R. Laflamme, and G. J. Milburn, *A scheme for efficient quantum computation with linear optics*, Nature **409**, 46 (2001).

[58] D. Loss and D. P. DiVincenzo, *Quantum computation with quantum dots*, Phys. Rev. A **57**, 120 (1998).

[59] R. Hanson, L. P. Kouwenhoven, J. R. Petta, S. Tarucha, and L. M. K. Vandersypen, *Spins in few-electron quantum dots*, Rev. Mod. Phys. **79**, 1217 (2007).

[60] Y. Makhlin, G. Schön, and A. Shnirman, *Quantum-state engineering with Josephson-junction devices*, Rev. Mod. Phys. **73**, 357 (2001).

[61] T. D. Ladd *et al.*, *Quantum computers*, Nature **464**, 45 (2010).

[62] R. Barends *et al.*, *Superconducting quantum circuits at the surface code threshold for fault tolerance*, Nature **508**, 500 (2014).

[63] A. D. Ludlow, M. M. Boyd, J. Ye, E. Peik, and P. O. Schmidt, *Optical atomic clocks*, Rev. Mod. Phys. **87**, 637 (2015).

[64] S. N. Lea, *Limits to time variation of fundamental constants from comparisons of atomic frequency standards*, Rep. Prog. Phys. **70**, 1473 (2007).

[65] R. M. Godun *et al.*, *Frequency Ratio of Two Optical Clock Transitions in* $^{171}\mathrm{Yb}^{+}$ *and Constraints on the Time Variation of Fundamental Constants*, Phys. Rev. Lett. **113**, 210801 (2014).

[66] H. S. Margolis, *Frequency metrology and clocks*, J. Phys. B: At. Mol. Opt. Phys. **42**, 154017 (2009).

[67] A. A. Madej, P. Dubé, Z. Zhou, J. E. Bernard, and M. Gertsvolf, $^{88}Sr^{+}$ *445-THz Single-Ion Reference at the* 10^{-17} *Level via Control and Cancellation of Systematic Uncertainties and Its Measurement against the SI Second*, Phys. Rev. Lett. **109**, 203002 (2012).

[68] P. Dubé, A. A. Madej, Z. Zhou, and J. E. Bernard, *Evaluation of systematic shifts of the* $^{88}Sr^{+}$ *single-ion optical frequency standard at the* 10^{-17} *level*, Phys. Rev. A **87**, 023806 (2013).

[69] T. Rosenband *et al.*, *Frequency Ratio of Al^+ and Hg^+ Single-Ion Optical Clocks; Metrology at the 17th Decimal Place*, Science **319**, 1808 (2008).

[70] T. Schneider, E. Peik, and C. Tamm, *Sub-Hertz Optical Frequency Comparisons between Two Trapped $^{171}Yb^+$ Ions*, Phys. Rev. Lett. **94**, 230801 (2005).

[71] M. Chwalla *et al.*, *Absolute Frequency Measurement of the $^{40}Ca^+$ $4s\ ^2S_{1/2} - 3d\ ^2D_{5/2}$ Clock Transition*, Phys. Rev. Lett. **102**, 023002 (2009).

[72] M. Roberts, P. Taylor, G. P. Barwood, W. R. C. Rowley, and P. Gill, *Observation of the $^2S_{1/2} - ^2F_{7/2}$ electric octupole transition in a single $^{171}Yb^+$ ion*, Phys. Rev. A **62**, 020501 (2000).

[73] V. I. Yudin *et al.*, *Hyper-Ramsey spectroscopy of optical clock transitions*, Phys. Rev. A **82**, 011804 (2010).

[74] N. Huntemann *et al.*, *Generalized Ramsey Excitation Scheme with Suppressed Light Shift*, Phys. Rev. Lett. **109**, 213002 (2012).

[75] R. Li, K. Gibble, and K. Szymaniec, *Improved accuracy of the NPL-CsF2 primary frequency standard: evaluation of distributed cavity phase and microwave lensing frequency shifts*, Metrologia **48**, 283 (2011).

[76] K. Szymaniec, S. Lea, and K. Liu, *An evaluation of the frequency shift caused by collisions with background gas in the primary frequency standard NPL-CsF2*, IEEE Trans. Ultrason. Ferr. **61**, 203 (2014).

[77] C. W. Chou, D. B. Hume, J. C. J. Koelemeij, D. J. Wineland, and T. Rosenband, *Frequency Comparison of Two High-Accuracy Al^+ Optical Clocks*, Phys. Rev. Lett. **104**, 070802 (2010).

[78] P. O. Schmidt *et al.*, *Spectroscopy Using Quantum Logic*, Science **309**, 749 (2005).

[79] N. F. Ramsey, *Experiments with separated oscillatory fields and hydrogen masers*, Rev. Mod. Phys. **62**, 541 (1990).

[80] J. J. Bollinger, W. M. Itano, D. J. Wineland, and D. J. Heinzen, *Optimal frequency measurements with maximally correlated states*, Phys. Rev. A **54**, R4649 (1996).

[81] D. Leibfried *et al.*, *Toward Heisenberg-Limited Spectroscopy with Multiparticle Entangled States*, Science **304**, 1476 (2004).

[82] D. Leibfried *et al.*, *Creation of a six-atom Schrödinger catstate*, Nature **438**, 639 (2005).

[83] M. A. Nielsen and I. L. Chuang, *Quantum Computation and Quantum Information (Cambridge Series on Information and the Natural Sciences)*, 1 ed. (Cambridge University Press, 2004).

[84] R. W. Boyd, *Nonlinear optics* (Academic press, 2003).

[85] V. Letchumanan, *Coherent Control and Ground State Cooling of a Single* $^{88}Sr^{+}$ *Ion*, PhD thesis, Imperial College London, 2004.

[86] H.-R. Noh and W. Jhe, *Analytic solutions of the optical Bloch equations*, Opt. Commun. **283**, 2353 (2010).

[87] E. L. Hahn, *Spin Echoes*, Phys. Rev. **80**, 580 (1950).

[88] M. Drewsen and A. Brøner, *Harmonic linear Paul trap: Stability diagram and effective potentials*, Phys. Rev. A **62**, 045401 (2000).

[89] S. Gulde, *Experimental realization of quantum gates and the Deutsch-Josza algorithm with trapped* $^{40}Ca^{+}$ *ions*, PhD thesis, University of Innsbruck, 2003.

[90] M. Brownnutt, $^{88}Sr^{+}$ *ion trapping techniques and technologies for quantum information processing*, PhD thesis, Imperial College London, 2007.

[91] W. Nagourney, J. Sandberg, and H. Dehmelt, *Shelved optical electron amplifier: Observation of quantum jumps*, Phys. Rev. Lett. **56**, 2797 (1986).

[92] C. E. Moore, *Atomic Energy Levels* (National Bureau of Standards Washington, DC, 1958).

[93] A. Gallagher, *Oscillator Strengths of Ca II, Sr II, and Ba II*, Phys. Rev. **157**, 24 (1967).

[94] H. S. Margolis *et al.*, *Absolute frequency measurement of the 674-nm* $^{88}Sr^{+}$ *clock transition using a femtosecond optical frequency comb*, Phys. Rev. A **67**, 032501 (2003).

[95] D. F. James, *Quantum dynamics of cold trapped ions with application to quantum computation*, Appl. Phys. B **66**, 181 (1998).

[96] C. J. Foot, *Atomic physics* (OUP Oxford, 2004).

[97] G. Wilpers, P. See, P. Gill, and A. G. Sinclair, *A monolithic array of three-dimensional ion traps fabricated with conventional semiconductor technology*, Nature Nanotech. **7**, 572 (2012).

[98] M. Brownnutt *et al.*, *Controlled photoionization loading of* $^{88}Sr^{+}$ *for precision ion-trap experiments*, Appl. Phys. B **87**, 411 (2007).

[99] P. See, G. Wilpers, P. Gill, and A. G. Sinclair, *Fabrication of a Monolithic Array of Three Dimensional Si-based Ion Traps*, J. Microelectromech. Syst. **22**, 1180 (2013).

[100] M. Brownnutt, G. Wilpers, P. Gill, R. C. Thompson, and A. G. Sinclair, *Monolithic microfabricated ion trap chip design for scaleable quantum processors*, New J. Phys. **8**, 232 (2006).

[101] G. Wilpers, P. See, P. Gill, and A. Sinclair, *A compact UHV package for microfabricated ion-trap arrays with direct electronic air-side access*, Appl. Phys. B **111**, 21 (2013).

[102] J. Siverns, L. Simkins, S. Weidt, and W. Hensinger, *On the application of radio frequency voltages to ion traps via helical resonators*, Appl. Phys. B **107**, 921 (2012).

[103] R. G. DeVoe and C. Kurtsiefer, *Experimental study of anomalous heating and trap instabilities in a microscopic* ^{137}Ba *ion trap*, Phys. Rev. A **65**, 063407 (2002).

[104] I. Biaggio, B. Zysset, P. Kerkoc, L.-S. Wu, and P. Günter, *Refractive indices of orthorhombic $KNbO_3$ II. Phase-matching configurations for nonlinear-optical interactions*, J. Opt. Soc. Am. B **9**, 507 (1992).

[105] T. Hansch and B. Couillaud, *Laser frequency stabilization by polarization spectroscopy of a reflecting reference cavity*, Opt. Commun. **35**, 441 (1980).

[106] A. Madej, L. Marmet, and J. Bernard, *Rb atomic absorption line reference for single Sr^+ laser cooling systems*, Appl. Phys. B **67**, 229 (1998).

[107] D. J. Wineland and W. M. Itano, *Laser cooling of atoms*, Phys. Rev. A **20**, 1521 (1979).

[108] W. M. Itano and D. Wineland, *Laser cooling of ions stored in harmonic and Penning traps*, Phys. Rev. A **25**, 35 (1982).

[109] R. Blatt, G. Lafyatis, W. Phillips, S. Stenholm, and D. Wineland, *Cooling in traps*, Phys. Scripta **1988**, 216 (1988).

[110] A. Sinclair, M. Wilson, and P. Gill, *Improved three-dimensional control of a single strontium ion in an endcap trap*, Opt. Commun. **190**, 193 (2001).

[111] A. Steffen *et al.*, *Note: In situ measurement of vacuum window birefringence by atomic spectroscopy*, Rev. Sci. Instrum. **84**, (2013).

[112] F. Schmidt-Kaler *et al.*, *Realization of the Cirac-Zoller controlled-NOT quantum gate*, Nature **422**, 408 (2003).

[113] M. T. Baig *et al.*, *A scalable, fast, and multichannel arbitrary waveform generator*, Rev. Sci. Instrum. **84**, (2013).

[114] B. Blinov, D. Leibfried, C. Monroe, and D. Wineland, *Quantum Computing with Trapped Ion Hyperfine Qubits*, Quant. Inf. Proc. **3**, 45 (2004).

[115] V. Letchumanan, P. Gill, A. G. Sinclair, and E. Riis, *Optical-clock local-oscillator stabilization scheme*, J. Opt. Soc. Am. B **23**, 714 (2006).

[116] M. H. Levitt, *Composite pulses*, Prog. Nucl. Mag. Res. Sp. **18**, 61 (1986).

[117] J. Thom, G. Wilpers, E. Riis, and A. G. Sinclair, *Accurate and agile digital control of optical phase, amplitude and frequency for coherent atomic manipulation of atomic systems*, Opt. Express **21**, 18712 (2013).

[118] B. C. Young, F. C. Cruz, W. M. Itano, and J. C. Bergquist, *Visible Lasers with Subhertz Linewidths*, Phys. Rev. Lett. **82**, 3799 (1999).

[119] M. M. Boyd *et al.*, *Optical Atomic Coherence at the 1-Second Time Scale*, Science **314**, 1430 (2006).

[120] M. J. Snadden, R. B. M. Clarke, and E. Riis, *Injection-locking technique for heterodyne optical phase locking of a diode laser*, Opt. Lett. **22**, 892 (1997).

[121] D. Bacon, *Operator quantum error-correcting subsystems for self-correcting quantum memories*, Phys. Rev. A **73**, 012340 (2006).

[122] P. Aliferis and A. W. Cross, *Subsystem Fault Tolerance with the Bacon-Shor Code*, Phys. Rev. Lett. **98**, 220502 (2007).

[123] P. Gill, W. Murray, and M. H. Wright, *Practical Optimization* (Emerald, New York, 1982).

[124] F. J. Harris, *On the use of windows for harmonic analysis with the discrete Fourier transform*, Proc. of the IEEE **66**, 51 (1978).

[125] B. Abraham and J. Ledolter, *Statistical Methods for Forecasting* (Wiley, New York, 1983).

[126] S. S. Ivanov, N. V. Vitanov, and N. V. Korolkova, *Creation of arbitrary Dicke and NOON states of trapped-ion qubits by global addressing with composite pulses*, New J. Phys. **15**, 023039 (2013).

[127] S. S. Ivanov and N. V. Vitanov, *High-fidelity local addressing of trapped ions and atoms by composite sequences of laser pulses*, Opt. Lett. **36**, 1275 (2011).

[128] P. B. R. Nisbet-Jones, J. Dilley, A. Holleczek, O. Barter, and A. Kuhn, *Photonic qubits, qutrits and ququads accurately prepared and delivered on demand*, New J. Phys. **15**, 053007 (2013).

[129] A. Peters, K. Y. Chung, and S. Chu, *High-precision gravity measurements using atom interferometry*, Metrologia **38**, 25 (2001).

[130] M. J. Snadden, J. M. McGuirk, P. Bouyer, K. G. Haritos, and M. A. Kasevich, *Measurement of the Earth's Gravity Gradient with an Atom Interferometer-Based Gravity Gradiometer*, Phys. Rev. Lett. **81**, 971 (1998).

[131] T. L. Gustavson, P. Bouyer, and M. A. Kasevich, *Precision Rotation Measurements with an Atom Interferometer Gyroscope*, Phys. Rev. Lett. **78**, 2046 (1997).

[132] D. G. Blair, E. J. Howell, L. Ju, and C. Zhao, *Advanced Gravitational Wave Detection*, 1 ed. (Cambridge University Press, 2012).

[133] P. Kwee *et al.*, *Stabilized high-power laser system for the gravitational wave detector advanced LIGO*, Opt. Express **20**, 10617 (2012).

[134] J. Rollins, D. Ottaway, M. Zucker, R. Weiss, and R. Abbott, *Solid-state laser intensity stabilization at the* 10^{-8} *level*, Opt. Lett. **29**, 1876 (2004).

[135] B. Canuel *et al.*, *Sub-nanoradiant beam pointing monitoring and stabilization system for controlling input beam jitter in gravitational wave interferometers*, Appl. Opt. **53**, 2906 (2014).

[136] T. Kessler *et al.*, *A sub-40-mHz-linewidth laser based on a silicon single-crystal optical cavity*, Nature Photonics **6**, 687 (2012).

[137] M. J. Biercuk *et al.*, *Optimized dynamical decoupling in a model quantum memory*, Nature **458**, 996 (2009).

[138] B. Bloom *et al.*, *An optical lattice clock with accuracy and stability at the* 10^{-18} *level*, Nature **506**, 71 (2014).

[139] J. Liu, Y. Kida, T. Teramoto, and T. Kobayashi, *Generation of stable sub-10 fs pulses at 400 nm in a hollow fiber for UV pump-probe experiment*, Opt. Express **18**, 4664 (2010).

[140] T. Kanai *et al.*, *Pointing stabilization of a high-repetition-rate high-power femtosecond laser for intense few-cycle pulse generation*, Appl. Phys. Lett. **92**, (2008).

[141] A. Stalmashonak, N. Zhavoronkov, I. V. Hertel, S. Vetrov, and K. Schmid, *Spatial control of femtosecond laser system output with submicroradian accuracy*, Appl. Opt. **45**, 1271 (2006).

[142] R. A. Hardin, Y. Liu, C. Long, A. Aleksandrov, and W. Blokland, *Active beam position stabilization of pulsed lasers for long-distance ion profile diagnostics at the Spallation Neutron Source (SNS)*, Opt. Express **19**, 2874 (2011).

[143] R. Drever *et al.*, *Laser phase and frequency stabilization using an optical resonator*, Appl. Phys. B **31**, 97 (1983).

[144] G. Barwood, P. Gill, G. Huang, and H. Klein, *Observation of a Sub-10-Hz Linewidth* $^{88}Sr^{+}$ $^{2}S_{1/2}$ - $^{2}D_{5/2}$ *Clock Transition at 674 nm*, IEEE Trans. Instrum. Meas. **56**, 226 (2007).

[145] L.-S. Ma, P. Jungner, J. Ye, and J. L. Hall, *Delivering the same optical frequency at two places: accurate cancellation of phase noise introduced by an optical fiber or other time-varying path*, Opt. Lett. **19**, 1777 (1994).

[146] D. Allan, *Statistics of atomic frequency standards*, Proc. of the IEEE **54**, 221 (1966).

[147] E. Lucero *et al.*, *Reduced phase error through optimized control of a superconducting qubit*, Phys. Rev. A **82**, 042339 (2010).

[148] T. Choi *et al.*, *Optimal Quantum Control of Multimode Couplings between Trapped Ion Qubits for Scalable Entanglement*, Phys. Rev. Lett. **112**, 190502 (2014).

[149] M. H. Goerz, E. J. Halperin, J. M. Aytac, C. P. Koch, and K. B. Whaley, *Robustness of high-fidelity Rydberg gates with single-site addressability*, Phys. Rev. A **90**, 032329 (2014).

[150] I. I. Boradjiev and N. V. Vitanov, *Control of qubits by shaped pulses of finite duration*, Phys. Rev. A **88**, 013402 (2013).

[151] I. I. Boradjiev and N. V. Vitanov, *Power narrowing in coherent atomic excitation by smoothly shaped pulsed fields*, Opt. Commun. **288**, 91 (2013).

[152] A. Soare *et al.*, *Experimental noise filtering by quantum control*, Nature Phys. **10**, 825 (2014).

[153] S. Kotler, N. Akerman, Y. Glickman, A. Keselman, and R. Ozeri, *Single-ion quantum lock-in amplifier*, Nature **473**, 61 (2011).

[154] S. Kotler, N. Akerman, Y. Glickman, and R. Ozeri, *Nonlinear Single-Spin Spectrum Analyzer*, Phys. Rev. Lett. **110**, 110503 (2013).

[155] J. Labaziewicz *et al.*, *Suppression of Heating Rates in Cryogenic Surface-Electrode Ion Traps*, Phys. Rev. Lett. **100**, 013001 (2008).

[156] D. Hite *et al.*, *100-Fold Reduction of Electric-Field Noise in an Ion Trap Cleaned with In Situ Argon-Ion-Beam Bombardment*, Phys. Rev. Lett. **109**, 103001 (2012).

[157] N. Daniilidis *et al.*, *Fabrication and heating rate study of microscopic surface electrode ion traps*, New J. Phys. **13**, 013032 (2011).

[158] W. M. Itano *et al.*, *Quantum projection noise: Population fluctuations in two-level systems*, Phys. Rev. A **47**, 3554 (1993).

[159] Y. Pawitan, *In all likelihood: statistical modelling and inference using likelihood* (Oxford University Press, 2001).

[160] C. Ballance, T. Harty, N. Linke, and D. Lucas, *High-fidelity two-qubit quantum logic gates using trapped $^{43}Ca^{+}$ ions*, arXiv preprint arXiv:1406.5473 (2014).